Stony Brook University

**Study of Dynamic Processes in Unique Oxide-Ion Conduction Materials
via Solid State NMR Spectroscopy**

A Dissertation Presented

by

Lesley Holmes

To

The Graduate School

In Partial Fulfillment of the

Requirements

for the Degree of

Doctor of Philosophy

in

Chemistry

Stony Brook University

December 2008

Stony Brook University

The Graduate School

Lesley Holmes

We, the dissertation committee for the above candidate for the

Doctorate of Philosophy degree, hereby recommend

acceptance of this dissertation.

Clare P. Grey Dissertation Advisor

Professor, Department of Chemistry

Philip Johnson Chairperson of Defense

Professor, Department of Chemistry

John B. Parise, Third Member

Professor, Department of Chemistry

Philip J. Grandinetti, Outside Member

Professor, Department of Chemistry, The Ohio State University

This dissertation is accepted by the Graduate School

Dean of the Graduate School
Lawrence Martin

Abstract of the Dissertation

Study of Localized Dynamic Processes in Unique Oxide-Ion Conduction

Materials

via Solid State NMR Spectroscopy

By

Lesley Holmes

Doctorate of Philosophy

in

Chemistry

Stony Brook University

2008

Detailed examination of the conduction processes in solid oxides identified as potentially beneficial materials for use as electrolytes in solid oxide fuel cells (SOFC's), is of tremendous interest. The current study focuses on materials that are of potential interest in forming the electrolyte layer of a SOFC, or as gas sensors or separation membranes. Currently, the most common electrolyte material used in SOFC applications is yttria stabilized zirconia (YSZ). To achieve reasonable levels of conduction through this material, high operating temperatures $\geq 800°C$ are required. However, devices containing materials which demonstrate reasonable conduction at slightly lower temperatures ($\approx 600°C$) could potentially be constructed from a wider range of materials i.e. stainless steel. Given the unique and sensitive ability NMR has to examine the

subtle dynamic aspects of a system on a localized level, we have undertaken to use this technique to answer some difficult questions regarding several complex ionically conducting solid oxide materials. First, a uniquely constructed, column-containing system of the formula $Bi_{26}Mo_{10}O_{69}$ was studied because it is compositionally related to materials which have been found to be highly conducting, but has a very unusual structure. This material demonstrated unexpected levels of ionic motion at a tremendously wide range of temperatures. Next, the oxide conduction aspects of the parent as well as lanthanum and gallium doped forms of barium indium oxide ($Ba_2In_2O_5$) were examined in depth. While NMR spectra have previously been acquired of the end member of this material, a re-examination at higher field strengths revealed new structural information. Lanthanum and gallium doped analogs were examined by ^{17}O and ^{71}Ga NMR for the first time. Finally, proton conduction in hydrated analogs of barium indium oxide ($Ba_2In_2O_5 \cdot H_2O$) was examined by variable temperature NMR. Proton conducting hydrates of oxide materials are very useful as electrolytes in intermediate temperature solid oxide fuel cells (ITSOFC). Proton spectra have previously been acquired for this system at room temperature, however, no interpretation as to the structural or dynamic implications of these spectra have yet been undertaken until the current study.

Table of Contents

Chapter 1

Introduction

Chapter 2

Variable Temperature ^{17}O NMR Study of Oxygen Motion in the Anionic

Conductor $Bi_{26}Mo_{10}O_{69}$

Chapter 3

Analysis of Structural Characteristics and Dynamics of Lanthanum &

Gallium-Doped $Ba_2In_2O_5$ via Ultra-High Field ^{17}O Solid State NMR

Chapter 4

Proton Conduction and Hydration Dynamics in $Ba_2In_2O_5 \cdot H_2O$

List of Figures

Acknowledgments

Chapter 1

Introduction

1.1   Solid Oxide Electrolytes as Anionic Conduction Materials

Currently, tremendous interest has arisen in examining the conduction processes in solid oxides that have been identified as potentially beneficial materials for use as electrolytes in solid oxide fuel cells, and in monitors and sensors for the measurement of partial pressures of gases,[1,2]. A solid oxide fuel cell (SOFC) electrochemically converts the oxidation of a fuel into electricity directly. Unlike batteries, fuel cells require the continued application of reactant to generate power, but under proper reaction conditions, can be run under nearly continuous operation with little to no maintenance. Efficiencies of up to 60% have been achieved for this type of fuel cell alone, and up to 85%[3,4] for hybrid systems which use excess heat to drive a turbine engine. SOFC's are unique in their simplicity. They contain only an ionically conducting solid oxide (ceramic) electrolyte layer, anode and cathode layers, and binding media. Oxygen gas from the air is reduced into oxygen ions at the cathode. These ions then diffuses through the electrolyte material to the anode where the applied hydrogen fuel is oxidized to form electrons and water as a byproduct (Figure 1.1):

$$\textit{Anode Reaction}: \ 2H_2 + 2O^{2-} \rightarrow 2H_2O + 4e^-$$

$$[1.1]^4$$

$$\textit{Cathode Reaction: } O_2 + 4e^- \rightarrow 2O^{2-}$$

$$[1.2]^4$$

$$\textit{Overall Cell Reaction: } 2H_2 + O_2 \rightarrow 2H_2O$$
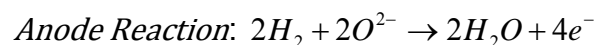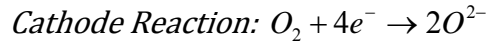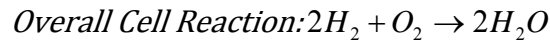
$$[1.3]^4$$

This type of fuel cell is stable over long time periods and is relatively inexpensive to build[5].

The current study focuses on ceramic materials which have been found to be of potential interest in forming the electrolyte layer of a SOFC. Currently, the most common electrolyte material used in solid oxide fuel cell applications is yttria stabilized zirconia (YSZ). To achieve reasonable levels of oxygen ion conduction through this material, high operating temperatures ≥ 800°C are required. High operating temperatures are useful for operating a fuel cell since a liquid fuel source, such as methanol, can be used directly, reforming hydrogen ions in situ:

$$\textit{Anode: } CH_3OH + H_2O \rightarrow CO_2 + 6H^+ + 6e^-$$

$$[1.4]^6$$

$$\textit{Cathode: } (3/2)O_2 + 6H^+ + 6e^- \rightarrow 3H_2O$$

$$[1.5]^6$$

$$\textit{Overall Reaction: } CH_3OH + (3/2)O_2 \rightarrow CO_2 + H_2O$$
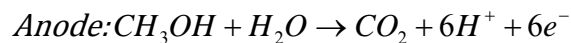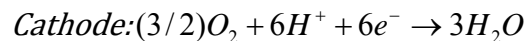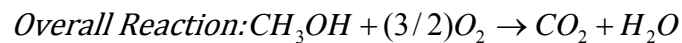
$$[1.6]^6$$

However, devices containing materials demonstrating reasonable conduction at slightly lower temperatures (≈ 600°C) could potentially allow for devices to be constructed from a wider range of materials i.e. stainless steel. Gadolinium doped cerium oxide and bismuth oxide have been examined as potential alternatives to YSZ. Both demonstrate high levels of ionic conduction below 700°C, but are highly susceptible to reduction at the anode[7] making them less than ideal candidates for devices requiring long lifetimes. Since an ideal electrolyte material for SOFC's has not been found yet, there is a need for a better understanding of what structural aspects of these ceramics permit efficient ionic conductivity.

It has been found that the structural characteristics of compounds with high ionic conductivity tend to be those that have[1]:

1. A large number of mobile ions of a single species.
2. Vacancies with similar potentials to the occupied sites.
3. A low activation energy barrier for ion hopping between sites.
4. A structure with open channels through which ions can move easily.
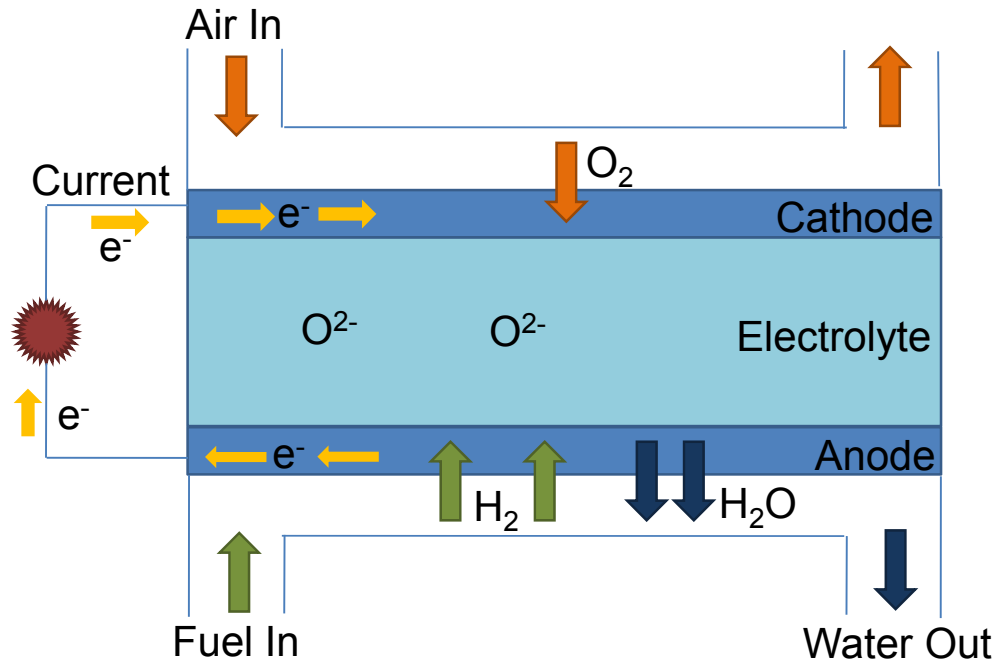
Figure 1.1 – Schematic of a Solid Oxide Fuel Cell (SOFC).

The conductivity of these materials can be calculated by:

$$\sigma = \eta Z_e \mu$$

[1.7][2]

Where n is the number of charge carriers per unit volume, Z_e is the charge in multiples of electron charge (e = 1.602189 x 10^{-19} C), and μ is the drift velocity in a constant electric field. These materials tend to become more conductive at high temperatures, and the temperature dependence of this mobility can be described by the Arrhenius equation:

$$\mu = \mu_0 e^{-E_a/kT}$$

[1.8][2]

Where E_a is the activation energy for cation hopping, k is the Boltzmann constant (k = 1.380662 x 10^{-23} JK^{-1}), and μ_0 is a pre-exponential proportionality constant. Ionic solids above absolute zero inherently contain intrinsic (stoichiometric) defects (Figure 1.2). Extrinsic defects can also be induced by the insertion of foreign atoms into the lattice. Ionic conduction occurs when ions "hop" into vacancies in the lattice or into interstitial positions between atoms.
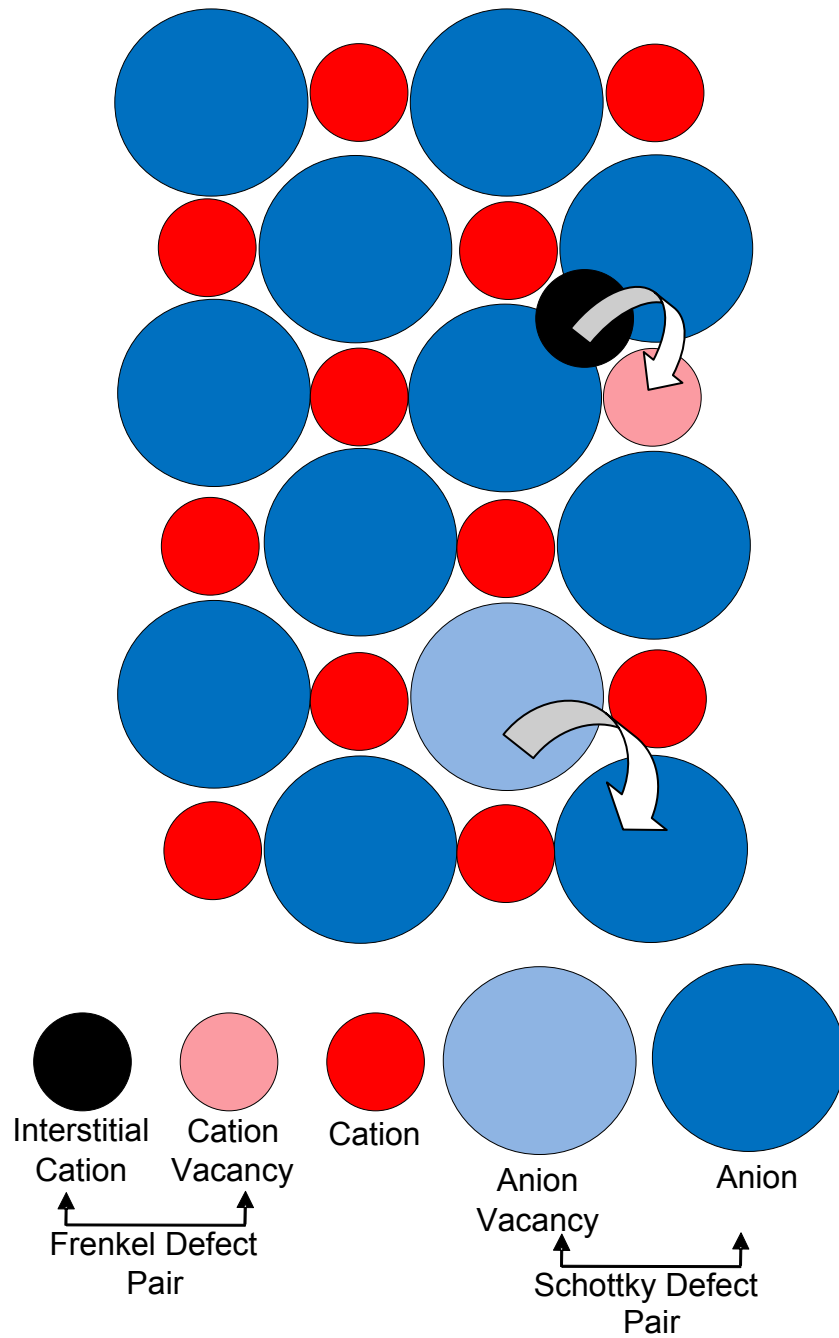
Figure 1.2 Schematic illustration of intrinsic point defects in a crystal of composition MX. Arrow shows anionic "hopping" motion of ionic conduction[2].

At low temperatures, the concentration of extrinsic defects dominates, and the conductivity can be calculated by:

$$\sigma = \left(\sigma_0 / T\right)e^{-E_z / T_z}$$

$$[1.9]^2$$

where σ_0 contains n and Z_e as well as hop frequency and distance information. Doping to increase extrinsic defects can change the conductivity in this temperature region. Intrinsic defects are of two varieties: Schottky defects which are identified by vacancies in the lattice, and Frenkel defects which are created when an atom moves into an interstitial position, leaving a hole (Figure 1.2). At high temperatures, the concentration of intrinsic defects dominates, and the conductivity is described by:

$$\sigma = \left(\sigma_0 / T\right)e^{-E_a / kT}e^{-\Delta H_{s/f} / 2kT}$$

$$[1.10]^2$$

where $H_{s/f}$ is the enthalpy of formation of a Schottky or Frenkel defect[2]. While conductivity tends to increase exponentially with temperature, in this high temperature regime, the activation energy barrier will depend upon both the activation energy for the ion jump and the enthalpy of formation of the defect. Figure 1.3 shows how the activation energy changes when a compound is in the temperature range of its extrinsic defect regime (low temperatures) versus its intrinsic defect regime (high temperatures). Conducting oxides which could potentially be used as electrolytes for SOFC applications often contain high

levels of intrinsic defects to facilitate oxygen hopping, and can be fine tuned to further increase conductivity by doping to increase the number of extrinsic defects.
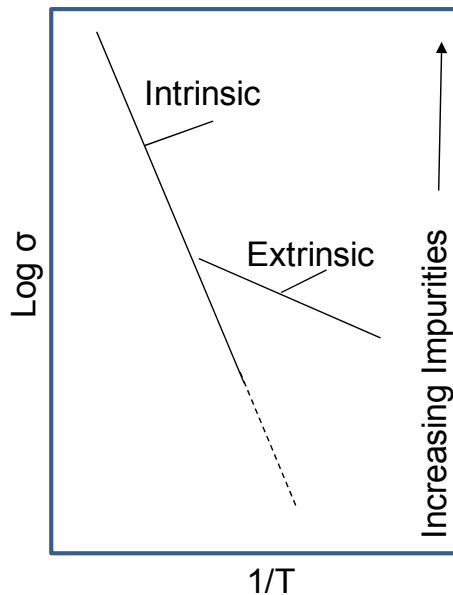
Figure 1.3 Arrhenius Plot - extrinsic vs. intrinsic conductivity regions of Na$^+$ ions in NaCl[1].

Due to the vacancy-laden nature of conducting oxides, many of these compounds readily absorb water into the lattice at ambient and slightly elevated (200-300°C) temperatures. The sorbed water dissociates into a hydroxide ion and a proton, with the hydroxide ion filling an oxygen vacancy and the proton associating with an oxygen in the lattice[8]. Protonic motion of hydrated oxides competes with oxygen conduction, but is also useful in charge conduction. For this reason, hydrated oxides have been found to be potentially good electrolytes in intermediate temperature solid oxide fuel cells (ITSOFC's). These devices

have the advantage of demonstrating a high level of protonic conduction even at modest temperatures, but will dehydrate as the temperature is raised to the point where, oxide conduction dominates. The disadvantage of the requisitely low operating temperatures of ITSOFC's is that liquid fuel cannot be reformed in situ such that hydrogen gas must be applied directly. At low temperatures, conductivity is also generally lower, reducing the power that can be generated from such a cell. The details of protonic conduction in a system in the current study are given in Chapter 4.

Whether the motion is anionic[9-14] or protonic[15-19], solid state NMR is a useful tool for looking at ionic hopping on a local level and determining the conduction mechanism of a system. With this information, one can determine the qualities that make for a good ionic conductor and at what temperature range. Thus, if the characteristics leading to high conductivity can be identified, better electrolyte materials can be designed.

1.2   Solid State Nuclear Magnetic Resonance (NMR) of Powder Samples

In order to appreciate how solid state NMR can be used to determine local structural information and dynamic phenomena in materials on a multitude of timescales, a brief introduction to the technique follows.

1.2.1   The NMR Experiment

For samples in solution, molecules tumble at a rate that is fast relative to the NMR timescale such that interactions dependent upon molecular orientation are averaged nearly to zero. Therefore the resolution of spectra for solution samples is usually quite good. Because powdered solid samples do not tumble freely they inherently have an orientation-dependence, and these interactions are not naturally averaged out, causing lines in solid spectra to be broadened (Figure 1.4). For this reason, gaining good resolution when performing an NMR experiment on a solid powder sample can often be difficult. However, because of this orientation dependence, solid-state NMR can provide much more information about local molecular dynamics of a system than its liquid counterpart. As the ceramic oxide materials examined in this study have localized dynamic properties which are of interest, we have chosen solid-state NMR to study them. While impedance measurements give information only about the average long-range conductive process, solid-state NMR one can derive the rate of highly localized motions on timescales from very slow (Hz-kHz) to very rapid (100's of MHz). This is illustrated in (Figure 1.5) where slow chemical exchange processes on the order of hertz to kilohertz cause lineshape changes, motions on the order of tens of kilohertz to megahertz affect the nutation rate or pulse length necessary to give maximum NMR signal amplitude, and very fast motions on the order of tens to hundreds of megahertz can be probed by examining the longitudinal relaxation rate for each site. Details for each of these measurement types are given below.

B_0
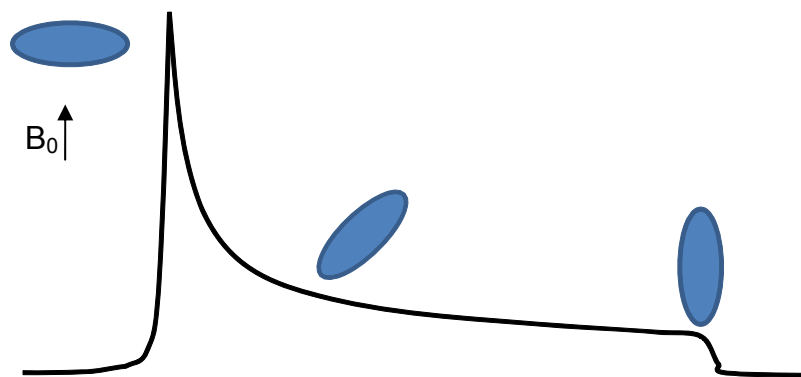
Figure 1.4 Powder Patterns: NMR spectral broadening due to different crystallite orientations[20].

τ_c(s) 10^2 10^0 10^{-2} 10^{-4} 10^{-6} 10^{-8} 10^{-10}

Oxygens Moving on the Order

Will Affect this Characteristic in the Spectra

Hz-kHz (0.01 -10 ms)   Line widths of Isotropic Resonances & Disappearance of Sidebands

kHz-MHz (0.1 -0.01 ms)   Nutation Rate

0.1-5MHz (0.01 -0.0001 ms)   Quadrupolar Interaction

10 – 100 MHz (<0.0001 ms) T_1 Relaxation Time
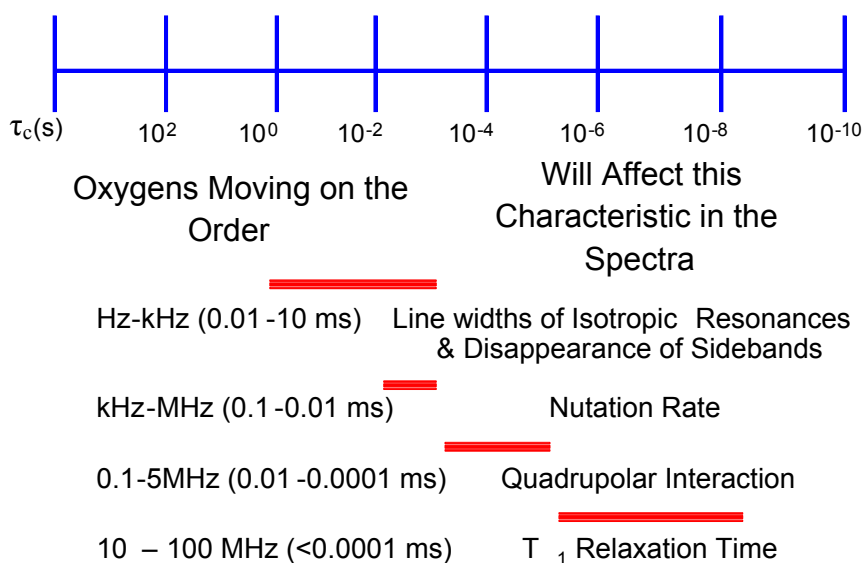
Figure 1.5 NMR Motional Timescales[21]

1.2.2 Chemical Exchange by Two-Dimensional Exchange Spectroscopy (EXSY)

Extremely slow ionic hopping or conformational changes in a solid can be

probed using a two-dimensional exchange (EXSY) experiment[21,22]. This

experiment is most effective when the frequency of the exchange process is significantly slower than the chemical shift difference between the exchanging sites, yet more rapid than the longitudinal relaxation rate (see section 1.2.11.1). The pulse program for this experiment is shown in Figure 1.6 below. It is a three pulse experiment, where the first 90° pulse converts the longitudinal (z-direction) magnetization of the spins into transverse (y-direction for pulse along x) magnetization. The spins are allowed to evolve during a time period t_1, wherein the oscillations of the spins causes them to become labeled with x and y magnetization. A second 90° pulse then converts the magnetization of the now labeled spins into the xz plane. Phase cycling then destroys the residual transverse component of the magnetization such that only longitudinal magnetization is left[21]. Chemical or conformation exchange is then allowed to occur for the spins now having labeled longitudinal magnetization during a mixing time, τ_m. A final 90° pulse is then applied to return the longitudinal magnetization to observable transverse magnetization. The system is then finally allowed to evolve during detection for a period t_2. While τ_m is fixed for the course of the experiment, the evolution periods t_1 and t_2 are varied and the two-dimensional experiment is plotted as a function of t_1 and t_2 in the first and second dimensions respectively. If the mixing time is chosen such that $\tau_m < k^{-1}$, the rate of exchange, no cross peaks will appear in the spectrum. If the mixing time chosen is sufficiently long to allow exchange to occur, cross peaks will appear in the two-dimensional spectrum for sites which are exchanging with one another, their intensity a function of the mixing time. If $\tau_m \approx 2k^{-1}$, diagonal and cross peaks will

have equal intensity. Finally, if $\tau_m > 2k^{-1}$, all peaks will lose intensity from longitudinal (T_1) relaxation.

The rate of exchange (k) can be calculated by performing several exchange experiments varying the mixing time. The ratio of the peak intensities of the cross to diagonal peaks is plotted as a function of the mixing time and fitted to:

$$\frac{a_{cross}}{a_{diag}}(\tau_m) = \frac{\sinh(k\tau_m)}{\cosh(k\tau_m)} = \tanh(k\tau_m)$$

[1.11][21]
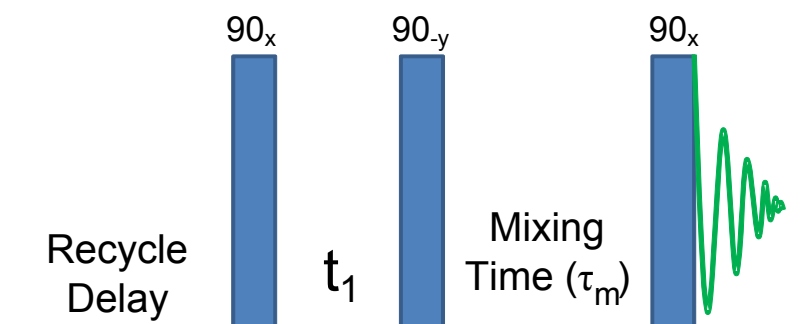
Figure 1.6 NMR pulse program for two-dimensional exchange (EXSY) experiment.

The EXSY pulse program was employed by Hampson et al[23]. for ^{17}O NMR of zirconium tungstate (ZrW_2O_8). The compositional similarities between this system and the oxides in the current work caused us to examine the results determined in this study. Two possible mechanisms for oxygen exchange in ZrW_2O_8 are an "S_N2 type" mechanism where bonds are broken and reformed

only between oxygens 1 & 2 as shown in Figure 1.7, or a "ratcheting motion",
wherein a conformational change involving a full rotation of two adjacent
tetrahedra would occur as shown in Figure 1.8. This second mechanism would
involve exchange between all four oxygen sites, but no breaking of bonds.
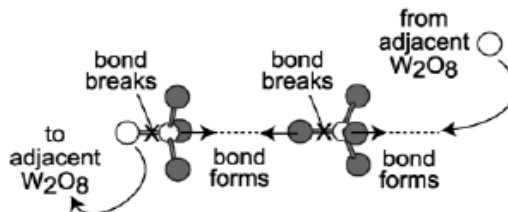
Figure 1.7 Proposed "S_N2 type" mechanism for oxygen exchange in ZrW_2O_8[24].
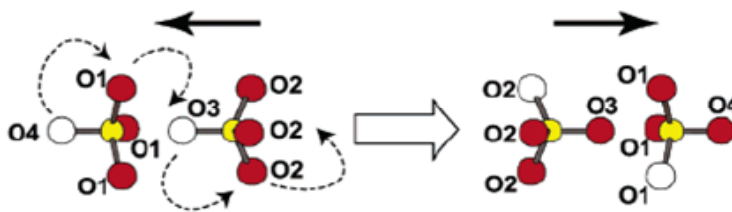
Figure 1.8 Proposed "ratcheting type" mechanism for oxygen exchange in
ZrW_2O_8[24].

Two dimensional chemical exchange data (see Figure 1.9) shows that hopping
occurs between all four sites, demonstrating that the motion in this system occurs
via the "ratcheting type" mechanism. While this result is not entirely surprising
given the relative energy difference between simple rotation of the tetrahedral
units and bond breaking, it is interesting to note that the exchange experiment
confirms this in an elegant and clear cut way.

14

Given some of the structural similarities between this and the systems currently studied, we had hoped to ascertain the mechanism for motional processes using two-dimensional exchange experiments. This analysis, however, requires the ability to resolve peaks for each of the exchanging sites. For the systems currently examined, we were unable to resolve individual oxygen sites for tetrahedral units, and, relaxation was too rapid relative to experimentally feasible mixing times for cross peaks to be observable.
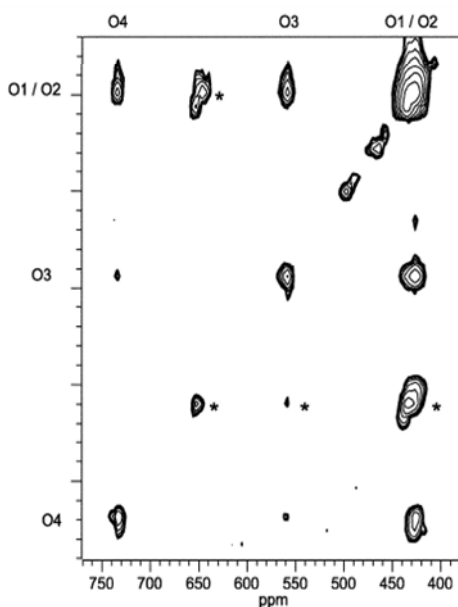
Figure 1.9 Two-dimensional exchange (EXSY) spectrum for ZrW_2O_8[24].

1.2.3 Line Broadening

Faster exchange of ions in a solid affects peak widths in an NMR spectrum. Consider an exchange process occurring between two sites in the

slow intermediate exchange regime where the rate of exchange is less than one half of the chemical shift difference (Ω_Δ) between the two exchange sites. In this regime, as the rate of exchange increases, peaks become broader and eventually the two peaks from exchanging sites will coalesce. This is referred to as motional broadening. In the regime where exchange processes are faster than one half of the chemical shift difference between peaks of exchanging sites, peaks will narrow as the rate of exchange increases. This is referred to as motional narrowing and it occurs when the exchange between sites is rapid enough that spins in different chemical sites do not have enough time to accumulate a significant phase difference in the free induction decay (FID) between two exchanges. The nuclei will have jumped to many different sites before they can precess to any large extent. The peak narrows because the precession frequency is not averaged between several exchange sites (Figure 1.10)[21].
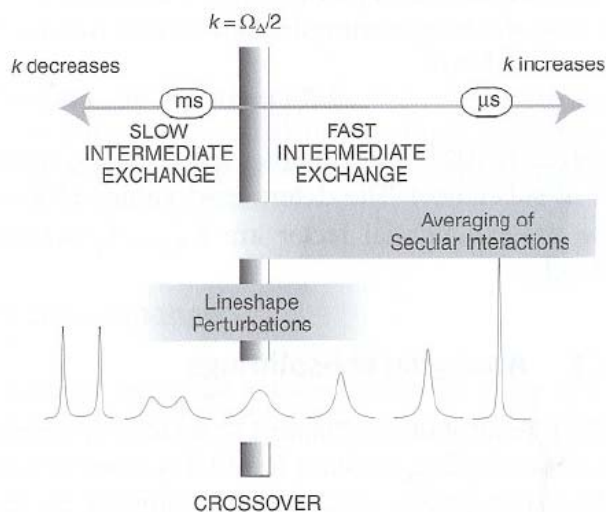
Figure 1.10 Slow vs. Fast Intermediate Exchange - Motional Broadening or Narrowing[21][♦]

1.2.4 Magic Angle Spinning (MAS)

Solid state NMR allows observation of those interactions pertaining to molecular orientation, but significant spectral overlap of peaks can make deconvolution a difficult and somewhat ambiguous process. Magic angle spinning (MAS) can greatly enhance spectral resolution at all fields. This technique takes advantage of the fact that the orientational dependence of the interactions that dominate line-broadening which is described by $3\cos^2\beta - 1$, the angular function being made up of second rank ($l = 2$) spherical harmonics. If a sample is spun at an angle β relative to the applied field B_0 (Figure 1.11), the orientational dependence of these nuclear spin interactions averaged over one rotor period gives rise to an isotropic resonance flanked by sidebands separated

[♦]   (21) Levitt, M. H. *Spin Dynamics: Basics of Nuclear Magnetic Resonance*; 1st ed.; John Wiley & Sons: New York, 2002.

at intervals of the spinning speed[25,26]. When β is 54.73° (referred to as the *Magic Angle*), $3\cos^2\beta - 1 = 0$, meaning that as the spinning frequency at this angle is much larger than the frequency of the anisotropy (giving rise to the line width) of the interaction, then the anisotropy associated with a given interaction will be averaged to zero. In summary, spinning at the magic angle (MAS) reduces a large amount of spectral broadening and resolution near that of solution samples can be achieved for very fast spinning of some samples.
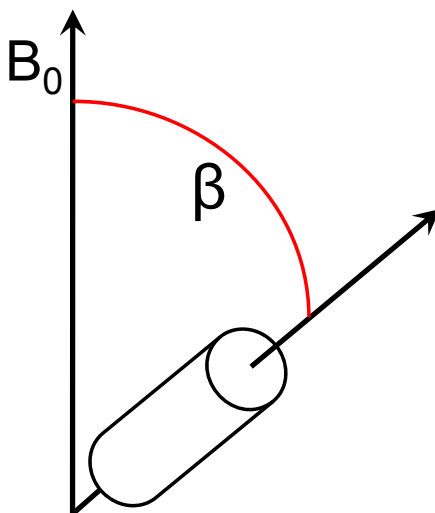
Figure 1.11 The angle (β) that defines the orientation of the rotor axis, with respect to the static magnetic field (B_0)[27].

1.2.5 Dipolar Interactions

One of the anisotropic interactions eliminated by magic angle spinning for nuclei with spin (I) equal to ½ are dipolar interactions. These are through space interactions dependent upon the distance between interacting nuclei (r) and the

angle (θ) formed between them and the bulk field (B_0) (Figure 1.12). These interactions can be quantified using the dipolar coupling constant which is described by:

$$\frac{3\cos^2\theta - 1)/2}{r^3}$$

[1.12]
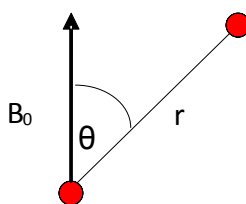
Figure 1.12 Dipolar Interaction.

1.2.6 Spin Properties of ^{17}O

As the motion of oxygen is of interest in most oxide solids studied, using NMR to directly examine oxygen may seem the logical choice to begin an analysis. This is rather non-trivial, however, as oxygen-17, the only NMR spin active oxygen nucleus, has a natural abundance of only 0.038%[28] making it highly insensitive to NMR. Obtaining NMR spectra in a reasonable timeframe therefore requires isotopic enrichment which can be costly and has varying rates of success dependent upon technique and the receptivity of the material being enriched. ^{17}O is also a quadrupolar nucleus with a spin (I) of $^5/_2$. Quadrupolar nuclei experience additional interactions to their spin ½ counterparts which can

provide additional orientation dependant information, but often also complicate spectral interpretation. This is described in further detail below.

1.2.7 Quadrupolar Nuclei

Nuclei such as oxygen with spin greater than ½ have an electric quadrupole moment (Figure 1.13). The nuclear charge distribution is non-spherical and, will couple with electric field gradients caused by nearby ions and/or electrons in addition to other anisotropic interactions (e.g. chemical shift anisotropy, dipolar, etc.). If the electronic environment surrounding the nuclei is highly symmetric, i.e. cubic, octahedral, tetrahedral, etc., the nucleus will experience little quadrupole coupling effect. If, however, the distribution of electric field gradients is not symmetric, the quadrupolar interaction can be quite large as in the case where there is a preferred orientation for an ellipsoidal nucleus (Figure 1.14).
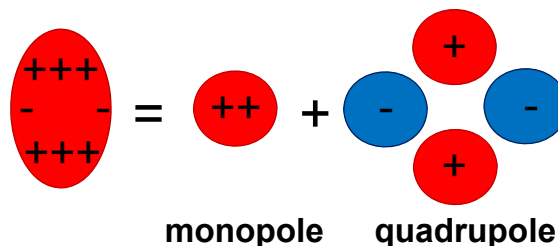
Figure 1.13 Quadrupolar Nucleus
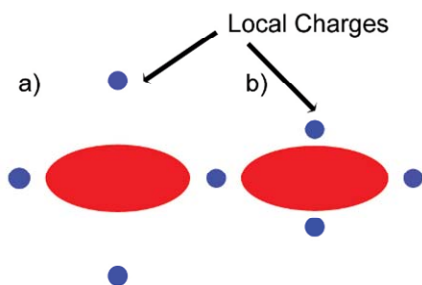
Figure 1.14 Quadrupolar Interaction – origin of the electrostatic quadrupole interaction in spins I > 1/2, reflecting the coupling between an ellipsoidal (quadrupolar) positive nuclear charge and a) a local symmetric electrostatic potential and b) a local, asymmetric electrostatic potential. There is a preferred orientation for the asymmetric case.

Quadrupole coupling causes the nucleus to precess not around the static field (B_0), but a combination of B_0 and the quadrupolar field. This coupling interaction can be very large, on the order of MHz. In the frame of the electric field gradient, the Hamiltonian associated with quadrupole coupling is:

$$H_Q = Q_{cc}\{3I_z^2 - I(I+1) + \eta_Q(I_x^2 - I_y^2)\}/I(2I-1)$$

[1.13][29]

Where Q_{cc} is the Quadrupole Coupling Constant = $e^2qQ/\hbar$ where e is the electron charge, eq is the z component of the electric field gradient felt at the nucleus, Q is the nuclear electric quadrupole moment[30], $\hbar$ is the reduced Plank constant (h/2π), and η_Q = the quadrupolar asymmetry parameter = $(V_{yy}-V_{xx})/V_{zz}$. When ω_0 (Larmor/resonance) frequency) » ω_Q (frequency of quadrupolar interaction), the eigenstates of the Zeeman Hamiltonian:

$$H_0 = \omega_0 \hat{I}_z$$

will form the zero-order basis functions. In the high field limit, the quadrupole interaction acts as a perturbation of the Zeeman states (see Figure 1.15). In the principal axis frame, the Hamiltonian representing the first order component of the quadrupole interaction is:

$$H_Q^{(1)} = 1/2Q'(\theta,\phi)\{I_z^2 - I(I+1)/3\}$$

where Q' is the quadrupole splitting as a function of the angles θ and Φ that define the orientation of the principal axis system of the quadrupole tensor defined by V_{xx}, V_{yy} and V_{zz} (see Figure 1.16):

$$Q'(\theta,\phi) = (\omega_Q/2)[(3\cos^2\theta - 1) - \eta_Q \sin^2\theta \cos 2\phi]$$

ω_Q, the quadrupole frequency is:

$$\omega_Q = 3e^2 qQ/[2I(2I-1)h]$$

And η_Q, the quadrupolar asymmetry parameter is:

$$\eta_Q = (V_{yy} - V_{xx})/V_{zz}$$

[1.18][27]

In the principal axis frame, the Hamiltonian representing the second order component of the quadrupole interaction is:

$$H_Q^{(2)} = -\left[\frac{e^2 qQ}{4I(2I-1)}\right]^2 (1/\hbar\omega_0)\left[\tfrac{1}{2}\eta^2 e^2 Q^2 I_z (2I(I+1) - 2I_z^2 - 1)\right]$$

[1.19][31]

This second-order correction to the frequency of the central transition is then given by:

$$\omega_Q^{(2)} = -(3\omega_Q^2/16\omega_0)(1 - \cos^2\theta)(9\cos^2\theta - 1)$$

[1.20][27]

This interaction is usually 10^2 to 10^3 times smaller than the first order interaction. It can, however, cause a large degree of spectral broadening and a change in the frequency of the central transition for samples possessing a large Q_{cc}. Equation [1.20][27] shows that as $\omega_Q^{(2)}$ scales as $1/\omega_0$, the effects of the second order quadrupolar effect will decrease with increasing field strength.

In the principle axis frame, the complete quadrupole hamiltonian in angular frequency units is then:

$$\hat{H}_Q = \frac{e^2qQ}{4I(2I-1)\hbar}\left[3\hat{I}_z^2 - \hat{I}^2 + \frac{1}{2}\eta_Q(\hat{I}_x^2 - \hat{I}_y^2)\right]$$

[1.21][25]

Because the frequency of the central transition (-½ ↔ ½) does not depend upon Q', it is unaffected by first order quadrupolar interactions. The second order perturbation, however, affects all spin transitions, including the central transition (Figure 1.15).
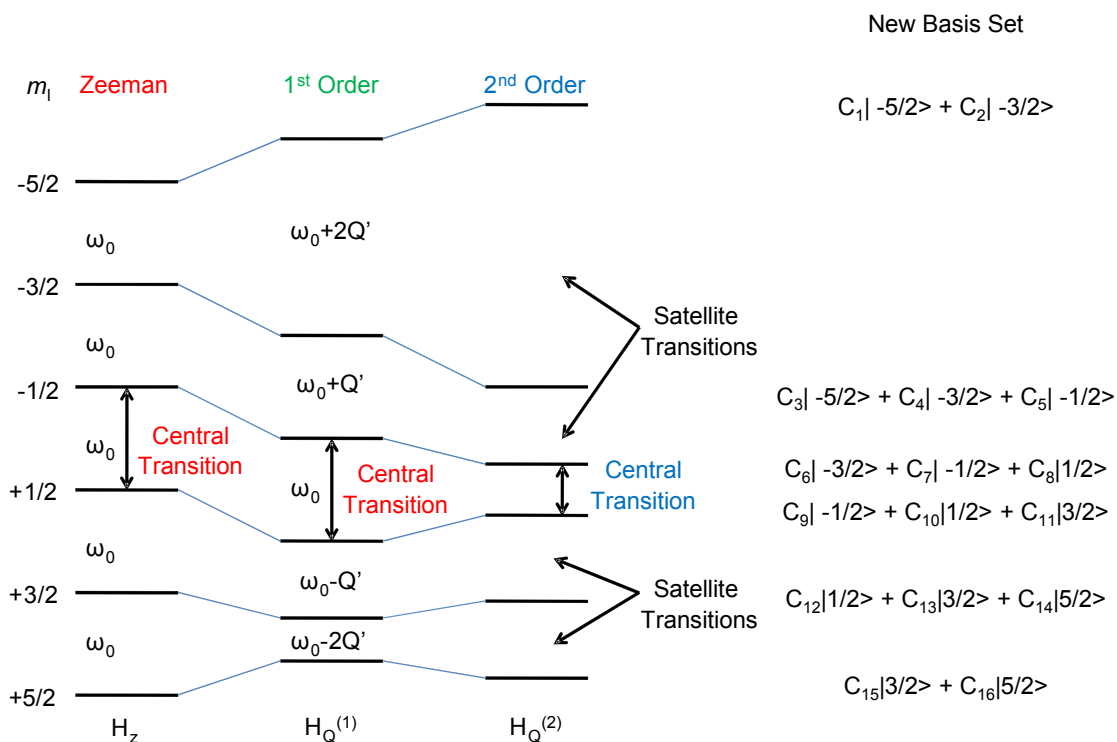
Figure 1.15 Quadrupolar interaction: effect on spin states for a spin 5/2 nucleus. C_n are coefficients representing the proportion of each spin state forming each new basis set.

1.2.8 NMR of Quadrupolar Nuclei

The angles (θ, Φ, β) that define the orientation of the quadrupole tensor (V_{xx}, V_{yy}, V_{zz}) and the rotor axis (ω_r), with respect to the static magnetic field (B_0) are shown in Figure 1.16. Under magic angle spinning (MAS), the correction to the central transition frequency in the rotor frame is given by:

$$\omega_{-1/2 \leftrightarrow 1/2} = Q_{cc}^2 / \omega_0 [I(I+1) - 3/4][A_0 + 8A_2(\theta, \phi)P_2(\cos\beta) + 18A_4(\theta, \phi)]P_4(\cos\beta)]$$

[1.22][29]

where A_0 is a constant proportional to the isotropic shift, $A_2(\theta,\varphi)$ and $A_4(\theta,\varphi)$ are orientation-dependant functions and the P_2 and P_4 terms are second- and fourth-rank *Legendre* polynomials as a function of the spinning angle (β) describing first and second order quadrupolar interactions respectively where:

$$P_2(\cos\beta) = 1/2(3\cos^2\beta - 1)$$

<div align="right">[1.23][32]</div>

$$P_4(\cos\beta) = 1/8(35\cos^4\beta - 30\cos^2\beta + 3)$$

<div align="right">[1.24][32]</div>
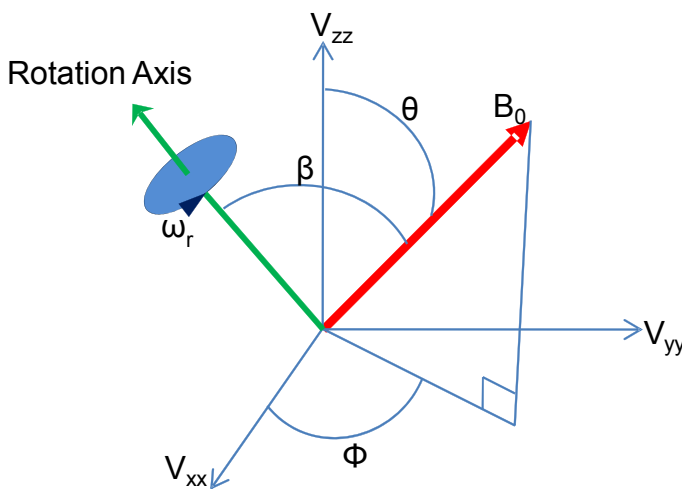
Figure 1.16 The angles (θ,Φ, β) that define the orientation of the quadrupole tensor (V_{xx}, V_{yy}, V_{zz}) and the rotor axis (ω_r), with respect to the static magnetic field (B_0)[27].

Note that $A_2(\theta,\Phi)$ and $A_4(\theta,\Phi)$ are responsible for the residual broadening that is observed even with sample spinning. Because the first order perturbation to the Zeeman interaction is described by a second rank polynomial [1.23][32], its effects

can be averaged out by magic angle spinning at a P_2 magic angle of 54.73°. This causes the broad resonances from the satellite transitions to be split evenly into sidebands on either side of the isotropic resonance, separated by the spinning speed. (Note that the isotropic resonance is the sum of the central transition resonance (-½ ↔ ½) and the center bands of the satellite transitions). The spread of these sidebands can be used to determine the quadrupole coupling constant (Q_{cc}) while their shape describes the quadrupolar asymmetry parameter $(\eta_Q = \dfrac{V_{xx} - V_{yy}}{V_{zz}})$ [25]. The second order perturbation is described by a fourth rank polynomial [1.24][32]. By inspection, there is no single solution to both [1.23][32] and [1.24][32], and therefore no single angle at which a sample can be spun to eliminate both first and second order quadrupolar effects[20,27,29,32-40]. Therefore significant line broadening, due to second order effects, is often observed for samples with sufficiently large quadrupole couplings, even with fast magic angle spinning. If sites are well resolved, quadrupole coupling effects can provide information about both the structure and dynamics of a system as they are highly sensitive to both. Structurally, sites in highly symmetric environments will show little quadrupolar broadening, but slight distortions in the lattice can cause significant line-broadening. On a dynamic level, very slow ionic hopping on the order of the ratio between the spinning speed and the quadrupole splitting will cause the disappearance of spinning sidebands. Faster motions, on the order of the quadrupole coupling, will average the effects of quadrupole splitting and cause a narrowing of isotropic peaks.

1.2.9 Multiple Quantum Magic Angle Spinning NMR (MQMAS)

As explained above, there is no single angle about which one can spin a powder sample to completely eliminate both first and second order effects from quadrupole coupling. For samples with large second order effects, this can be problematic if one wishes to acquire high resolution spectra. In order to overcome this, first mechanical means of spinning at both a P_2 and P_4 magic angle were developed. The first of these was double rotation (DOR), invented by Samoson et al.[41,42] wherein a sample is simultaneously spun at both the P_2 and P_4 (see [1.23][32] and [1.24][32]) magic angles in a rotor specially designed for this purpose as shown in Figure 1.17. By contrast, Dynamic Angle Spinning (DAS)[43-49], conceptualized by Llor et al.[50,51], makes the spinner axis time dependant. This requires that the angle of the rotor be switched between positions (β_1 & β_2) during the course of a two-dimensional echo experiment. The first period of evolution along one dimension is taken at β_1 and the second at β_2. The angles chosen must simultaneously fulfill conditions:

$$P_2(\cos\beta_2) = -P_2(\cos\beta_1)$$

[1.25][50]

And

$$P_4(\cos\beta_2) = -P_4(\cos\beta_1)$$

[1.26][50]

Where (β_1, β_2) is the DAS angle pair. This yields a two-dimensional correlation spectrum with a high-resolution isotropic dimension providing information about the chemical and second-order quadrupolar shifts, and an anisotropic dimension retaining the information about the size of the quadrupole coupling. But, in order for this to be effective, the longitudinal relaxation time must be sufficiently long such that magnetization information is retained in the sample while the rotor angle is switched, and this is often a difficult criterion to meet in a quadrupolar sample, as quadrupolar relaxation, particularly in samples having large quadrupole coupling, is very efficient.

While these two solutions are quite elegant, in order to achieve high resolution spectra of samples with large, second order quadrupole broadenings, while avoiding the necessity for specialized equipment and often unrealizable relaxation criteria involved in the DOR and DAS methods, Frydman and Harwood[29] developed a method where the same anisotropic averaging could be achieved by pulsing alone, in a two-dimensional correlation sequence they called Multiple-Quantum Magic Angle Spinning (MQMAS). Because the mixing of Zeeman and quadrupolar interactions makes multiple quantum coherences into allowed transitions, the MQMAS experiment is able to use an echo pulse sequence to correlate the frequencies of these multiple-quantum coherences with single-quantum coherences (Figure 1.15).
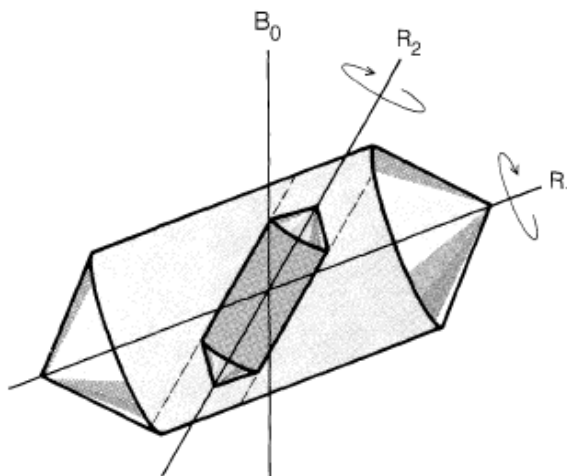
Figure 1.17 Diagram of the double rotor assembly used for DOuble Rotation (DOR) NMR techniques.[41]
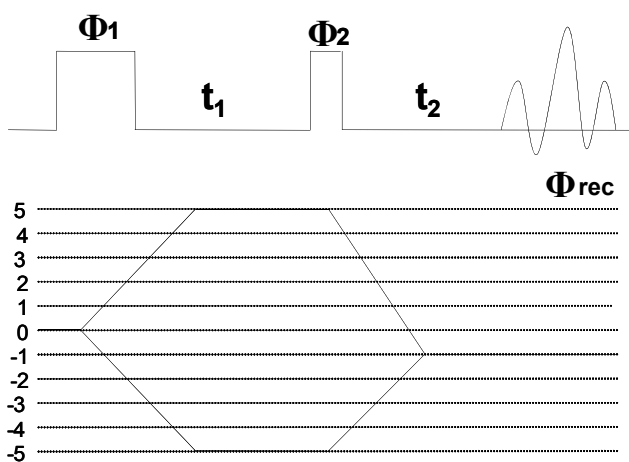
$\Phi 1 = $ 0°, 36°, 72°, 108°, 144°, 180°, 216°, 252°, 288°, 324°
$\Phi 2 = $ 0°
$\Phi rec = $ 0°, 180°

Figure 1.18 MQMAS pulse sequence with appropriate phase cycling for correlation of the pathway from $0 \rightarrow 5 \rightarrow -1$.

Using MQMAS, magic-angle spinning uses spatial averaging to remove first-order effects from chemical shift anisotropy, dipolar coupling and the second rank terms of second order quadrupolar interactions. At the same time, RF pulses

manipulate spin terms to average out the fourth rank terms of the second order quadrupole coupling interaction (Equation [1.24][32]). The experiment is performed in two dimensions where the spin coherences are allowed to evolve for two different times, t_1 and t_2 (Figure 1.18).

In the MQMAS pulse sequence (Figure 1.18), the first pulse ($\Phi 1$) excites all multiple quantum coherences. The system is then allowed to evolve in t_1, after which a second pulse ($\Phi 2$) converts all multiple quantum coherence to single quantum coherence. A t_1 dependent, linear phase correction is applied to the 2D data set in order to view the pure isotropic Fourier transformed spectrum. The resulting projections of the transformed two dimensional spectra are an anisotropic (=MAS only) spectrum in the f1 dimension and a high resolution isotropic spectrum in the f2 dimension. Amoureux and Fernandez describe analyzing MQMAS spectra by defining an isotropic chemical shift (CS) axis, an anisotropic axis (A) and a quadrupolar induced shift (QIS) axis[52,53] as shown in Figure 1.19. In this way, one can determine whether peak broadening is due primarily to chemical shift anisotropy, or to second order quadrupolar effects. When the quadrupole interaction is small, resonances are found on the chemical shift axis. Larger quadrupolar interactions will cause displacement in the QIS direction. Examination of one dimensional slices of the two dimensional spectrum will yield isotropic spectra for individual sites. In this way, spectra complicated by overlap from quadrupolar broadening can often be better interpreted using only a standard MAS probe.
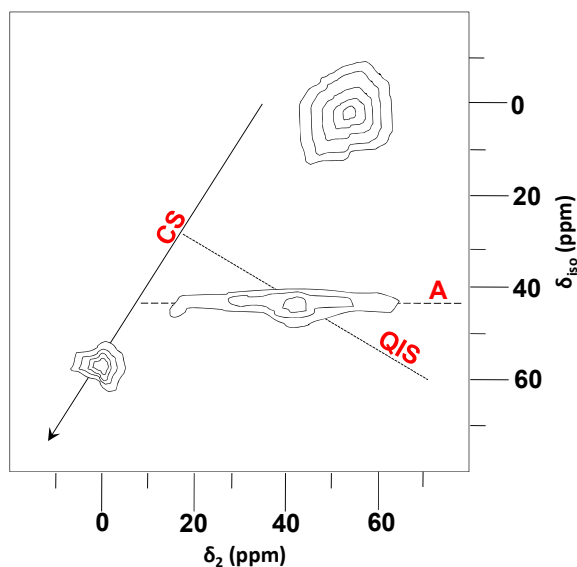
Figure 1.19 Diagram of a Multiple Quantum Magic Angle Spinning (MQMAS) NMR spectrum[52,53].

1.2.10 Nutation

When the quadrupole coupling of a given site is sufficiently small such that modeling of the lineshape becomes ambiguous, nutation studies can be another useful way to determine the approximate size of the quadrupole coupling constant at various temperatures. From this, information about the temperature dependence of motional processes on the order of the nutation frequency (tens of kHz) can also be derived.

For NMR, nutation refers to nuclear precession of the magnetization in response to perturbation by an RF pulse. A series of different pulse widths are applied to a sample to determine the duration of the RF pulse necessary to flip the magnetization completely into a plane perpendicular to the applied RF, i.e. the pulse length that results in the maximum signal amplitude. For quadrupolar

nuclei, because the amplitude of the quadrupolar interaction is sometimes larger than that of the RF pulse, two scenarios for the excitation are possible[37]:

1.   If the quadrupole interaction is small such that $\omega_Q << \omega_{RF,}$ all nuclear spin transitions are excited. The nutation frequency will be slow, resembling that of a solution sample containing the same nucleus (Figure 1.20 – Blue).

2.   If the quadrupole interaction is large such that $\omega_Q >> \omega_{RF,}$ only the central spin transition is excited. The nutation frequency will be much more rapid in this case, at $\omega_{nut} = I + 1/2$ times that of a spin half nucleus, while the amplitude will be proportionately less by a factor of $1/(I+1/2)$. (Figure 1.20 – Red).
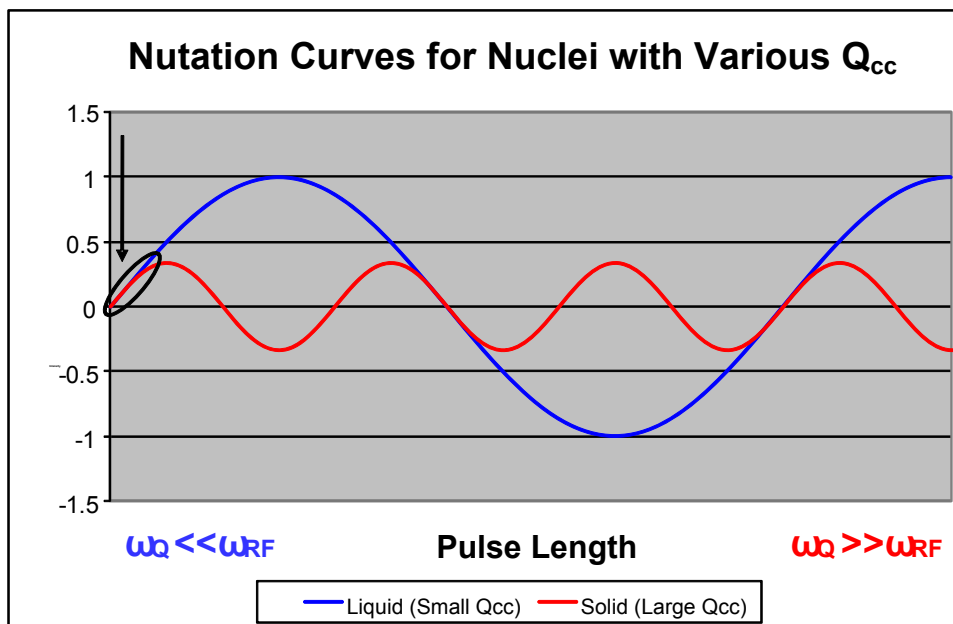
Figure 1.20 Nutation Curves for Nuclei with Various Q_{cc}'s – the circled region represents reponses that are nearly linear for both types of nuclei.

For short pulse durations, the response is essentially linear (intensity α time) for nuclei with either a large or a small quadrupole coupling constant (Figure 1.20 – Circled Region)[37]. For oxygen conducting compounds, a site that demonstrates slow (liquid-like) nutation at higher temperatures may in actuality have a larger quadrupole coupling than is indicated by the nutation frequency as much of the coupling may be averaged out by motion on the order of, or greater than the nutation frequency. This motion can be probed by performing experiments at low temperatures. The temperature at which the site demonstrates fast (solid-like) nutation at low temperatures is the temperature at which the motion is said to "freeze out" on the timescale of the nutation experiment.

1.2.11 Nuclear Spin Relaxation

In NMR, relaxation refers to the process by which spins right themselves after perturbation by RF pulses. Of greater interest in the current study, however, is that, for solids with ionic motion, the rate of relaxation of nuclei in different local environments can offer information about the very rapid (MHz) dynamics of the compound.

1.2.11.1   Spin-Lattice (T_1) Relaxation

Longitudinal (T_1) relaxation refers to the buildup of a net magnetization in the direction of the applied field (usually designated the z-direction). Because with T_1 relaxation the system enters a lower energy state, energy is said to be

released into the "lattice" or the rest of the system and the T_1 process is therefore often referred to as *spin-lattice* relaxation. From a quantum mechanical point of view, if an external magnetic field is applied to a group of nuclear spins, the degeneracy of the spin states will be removed and a small net spin density (described by the Boltzmann distribution) will exist in the lower energy state. Upon addition of an RF pulse, spins will be promoted into the higher energy state and then "relax" back into the lower energy state, dispersing energy into the lattice. For samples in solution where I = ½, this process generally proceeds via a single exponential:

$$M_z(t) = M_0(1 - e^{-t/T_1})$$

[1.27]

where M_z refers to the z-component of the magnetization and M_0 refers to the equilibrium value for the magnetization.

1.2.11.2   Spin-Spin (T$_2$) Relaxation

After the application of an RF pulse satisfying the resonance condition occurs, the (T_2) or *spin-spin* relaxation process refers to the loss of coincidence of spins within the xy plane. Spins in the xy plane precess at differing frequencies such that the transverse magnetization is said to "fan out". Eventually spin vectors point in all directions losing their phase coherence and the net

magnetization is lost. There is no energy change in the T_2 process, it occurs with only an entropy increase for the system. In a perfectly homogeneous field, and assuming no distribution of chemical shifts, the T_2 relaxation time can be determined from the full width at half height of singlet peaks as:

$$1/T_2 = \Delta\omega_{1/2}$$

[1.28][54]

Where $\Delta\omega_{1/2}$ is the peak width at ½ its maximum height (FWHM). This can also be thought of as T_2 line broadening.

1.2.11.3   Correlation Time (τ_c) / T_1 Minimum

The timescale for Brownian motion of solute in a solvent is described by the rotational correlation time, τ_c. This factor is defined as the amount of time is takes on average for a solute molecule to rotate by one radian. For a spherical molecule rotating in a liquid:

$$\tau_c = 4\pi a^3 \eta / 3kT$$

[1.29][54]

Where "a" is the hydrated radius of the solute and η is the viscosity of the solvent. The region of extreme narrowing occurs when the correlation time is shorter than one Larmor period of the nuclei. In this region, T_1 and T_2 relaxation times are equal. If the correlation time is increased (i.e. the temperature is decreased or the viscosity of the solution or size of the molecules increased), the

relaxation time of the system is reduced. T_1 reaches a minimum when τ_c is equal to the resonance frequency (ω_0) for a given nucleus. Further increases in correlation time do not allow for as much energy exchange to occur and therefore T_1 again increases. T_2, however, continues to decrease with increased τ_c as the correlation time now approaches the timeframe of other interactions (Figure 1.21).
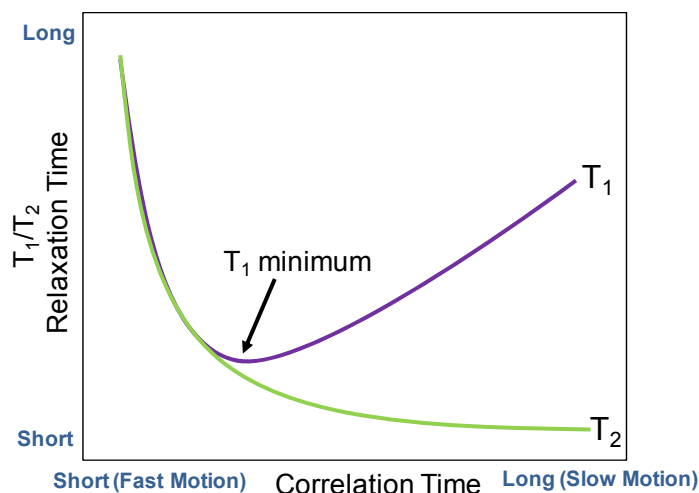
Figure 1.21 Dependence of Relaxation Times on Rotational Correlation Time.

For the anionic solids studied, $T_1 >> T_2$ and the correlation time (τ_c) is a function of the hopping frequency (exchange)[55] (Figure 1.21 far right). This value can then be compared to hop frequencies acquired from impedance data to ascertain whether they can be attributed to long range conductive jumps, or if only localized motions are contributing to the relaxation. As the temperature is increased, the rate of anionic motion increases and the correlation time

decreases. For these compounds, T_1 decreases and approaches a minimum with increasing temperature. This minimum should be seen at $1/\omega_0$.

1.2.11.4 Relaxation Mechanisms

1.2.11.4.1. Dipolar

The rotational motion of unpaired electrons or other nuclei in close proximity to a given nucleus causes small fluctuations in the local magnetic field. Dipolar coupling energetically "joins" spins to one another and allows them to "see" the effect i.e. motion of one another (section 1.2.7). If the fluctuation of the field is on the order of its Larmor frequency, relaxation of the nucleus can occur as described above. (Vibrational motion is usually at a frequency well above that of nuclear resonances.) That is, the fluctuating field provides a mechanism for energy exchange between nuclei and their surroundings; the energy released when nuclei in the upper energy state (opposing the field) enter the lower energy state, is transformed into a subsequent (slight) heating or cooling of the lattice. The rate of the relaxation is proportional to the probability that the local fluctuations are on the order of the resonance frequency. Dipolar coupling between nuclei scales with the distance between them (r) by a factor of $1/r^3$ and the angle formed between the internuclear vector and the static field (θ) (Figure 1.12). Each nucleus couples to its neighbors by the relationship:

$$\{1/2(3\cos^2\theta - 1)/r^3\}$$

[1.30]

38

The relaxation is proportional to the square of the dipolar interaction or $1/r^6$ (Figure 1.12)[21,54,56-59].

1.2.11.4.2. Quadrupolar

Due to their non-spherical charge distribution, quadrupolar nuclei (section 1.2.7) interact with electric field gradients generated by anisotropic distributions of charge surrounding them. Rotating charge distributions at the resonant frequency can facilitate an energy exchange between the nuclei and its surroundings via a T_1 mechanism, or cause a loss of nuclear phase coherence via a T_2 mechanism. The relaxation rate for quadrupolar nuclei in a diamagnetic solid can be greater than that arising from dipolar coupling by up to eight orders of magnitude as it is proportional to the strength of the coupling. The rate for relaxation of the various spin states of a quadrupolar nucleus differ from one another, ex. for a spin 3/2 nucleus, the spin transition from 3/2 to 1/2 or -3/2 to -1/2 differs from that from 1/2 to -1/2. These differing rates mean that the overall relaxation cannot be described by a single exponential. If the correlation time of a quadrupolar nuclear site is sufficiently long, the relaxation time will be the sum of I + ½ decaying exponential terms for I with half-integer values. For example, in the case of oxygen where I = 5/2, the relaxation will be made up of 5/2 + 1/2 = 3 exponential terms[60,61]. This is described by:

$$N_0 / n_0 = 1 - 0.06 e^{-\frac{4}{5}Wt} - 0.85 e^{-\frac{3}{2}Wt} - 0.09 e^{-\frac{33}{10}Wt}$$

[1.31][62]

Where n_0 is the difference in population between adjacent spin levels when equilibrium between spin system and lattice is achieved in the absence of RF power and W is the probability of the transition between any two given energy levels. Thus, three relaxation times (representative of three spin transitions) at 5/4W, 2/3W and 10/33W are derived. If the correlation time is short, i.e. when the electric field gradients are fluctuating much more rapidly than the Larmor frequency, the expressions will collapse to a single exponential decay[61]. Imperfections in a crystal lattice can also create differing electric field gradients, causing an additional source for distribution in relaxation times.

This is emphasized by McDowell et al., who state that the ability to determine if the non-exponential relaxation curves are intrinsic to the spin system or due to sample inhomogeneity of non-equivalent spins is very useful when trying to interpret the dynamic processes within a system[63,64]. By knowing what the expected magnetization recovery curve will be, one can distinguish between magnetic (i.e. driven by the motion of surrounding ions) and quadrupolar (driven by the modulation of the quadrupole coupling by the motion of the given spin itself) relaxation mechanisms. Magnetically driven relaxation occurs primarily when there is a high density of paramagnetic relaxation centers or if the nuclear quadrupole moment is sufficiently small such that the quadrupole relaxation mechanism cannot compete with other relaxation mechanisms. This means that the relaxation rate for compounds experiencing a magnetic relaxation mechanism will increase with decreasing temperature as paramagnetic effects will be amplified with decreasing temperature, while the rate for compounds

40

experiencing quadrupolar relaxation will decrease with decreasing temperature as molecular motions slow down.

In their studies of zirconium tungstate ZrW_2O_8, Hodgkinson and Hampson concluded for oxygen, as a quadrupolar nucleus with spin 5/2, "given the complexities introduced by multi-exponential T_1 relaxation, it would be difficult to use ^{17}O NMR to distinguish between mechanisms that have such similar overall effects[24,65,66]". As ^{17}O is in the intermediate quadrupolar regime (Section 1.2.10), the ZrW_2O_8 experiences excitation of both satellite and central transitions. Like previous groups, they found significant systematic errors in the plotting of their data that could not be accounted for by simple random error. They fit their data to a purely quadrupolar relaxation mechanism (a relaxation mechanism driven by local modulation of quadrupole coupling by the motion of a given spin with 4W/5 : 3W/2 : 33W/10 between the three rates[61]), a purely magnetic relaxation mechanism (a relaxation method driven by the motion of *other* ^{17}O nuclei, with 2W : 12W : 30W between the rates) and a single exponential. The data best fit the magnetic mechanism of relaxation indicating that the motion of oxygens in close proximity to the nucleus of interest is the primary mode of relaxation.

Due to the obvious complexity in describing the multi-exponential nature of decay processes stemming from combined relaxation processes in ionically conducting systems with quadrupolar nuclei having overlapping NMR peaks, the distribution of relaxation times can be estimated by modeling to a stretched exponential function[67]:

$$M(\infty) = M(t)(1 - e^{[-t/T_1)^\beta]})$$

Where β is the stretching exponent with 0 < β ≤ 1. The stretched exponent or Kohlrausch-Williams-Watts (KWW) function was first used by Kohlrausch in 1854[68-70] and later re-introduced into popular use by Graham Williams and David C. Watts[71,72] in the 1970's. Narayanan et al. used this approach in 1994 to describe the non-exponential decay processes of ^{29}Si in silicon carbide samples with paramagnetic impurities. They did so with the caveat, that, "for a model to be legitimate, we must not only have the best values for the parameters, but also some assurance that the model itself is appropriate".[73] They analyzed the stretched exponential approach to relaxation with the comment that, "while lacking the physical significance of some of the more sophisticated models, in certain situations, [it] represents a convenient model for non-exponential relaxation in solids." Of their data, the group observed that it is not possible upon mere inspection to determine whether the application of a stretched exponential fit is appropriate. By taking the sum of the squares of the values for the pure error in their data and the lack of fit, the group plotted results for both the single and stretched exponential models to show whether any residual lack of fit is due to a bias and not pure error. They concluded that the stretched exponential fit was appropriate as only this model gave results at a 95% confidence level[73]. While the complexities of silicon carbide as a paramagnetic system merit the use of a stretched exponential relaxation model, ^{29}Si is a spin ½ nucleus, unlike the

quadrupolar ^{17}O of interest in the current study. In models more closely approximating the added complexities introduced when quadrupolar nuclei are involved, studies of the relaxation behavior of ^{7}Li in heavy fermion LiV_2O_4[67,74] and orthorhombic perovskite $Li_{0.18}La_{0.61}IO_3$[75] still reached the conclusion that the stretched exponential model is appropriate for complex behavior in solids. For this reason, we have chosen to use this function to model the complex relaxation behaviors in the current systems. It is clear from the studies above that a large number of factors weigh into the relaxation mechanisms for solids with mobile oxygens including quadrupolar affects, defect interaction, and multiple modes of motion. Thus, while a wealth of information is available through NMR relaxation about ionic motion, great care must be taken when attempting to interpret its meaning.

1.2.11.5   Measuring Relaxation – The Pulse Delay Method

If the longitudinal relaxation of a nuclear site is sufficiently long, it can be measured through a series of experiments where a 90º RF pulse is applied and then a delay is allowed to occur before pulsing again. With each experiment, the delay time is increased, allowing the system to relax further back toward equilibrium before pulsing again. This method measures intensity as a function of recycle (pulse) delay. If the nuclear site is relaxing on the order of the time period chosen, the Fourier Transformed signal will increase with increasing delay time. That is, the system has been perturbed away from thermal equilibrium; after a

short time, the signal will be minimal, but if a longer delay is allowed to occur, the system will return to equilibrium and the signal will increase. Eventually the signal will reach a maximum and level off. This occurs at about 6 times the T_1 relaxation time.

1.2.11.6 Measuring Relaxation – The Inversion-Recovery Method

If the relaxation of a site is sufficiently rapid, i.e. the signal has leveled in delays so short that they are on the order of the inherent delays in taking a spectrum caused by hardware limitations, a pulse delay array cannot be used to measure longitudinal relaxation time. In this case, a series of *Inversion Recovery* experiments can be performed to determine T_1 (Figure 1.22). While similar to the pulse delay array, in this experiment, a 180º pulse is applied to the sample so that the signal is now in the –z direction. A delay (τ) is allowed first to occur and then a 90º pulse is applied and the signal is measured. However, the measured signal is now at 270º and the Fourier Transformed signal will be inverted. Spectra are acquired as a function of the delay time (τ). With each subsequent experiment, the delay is increased and the amplitude of the measured signal will decrease as the signal is relaxing further from the –z direction in the   period. Eventually the signal will disappear completely (null point) and then reappear upright and increase until it reaches a maximum.
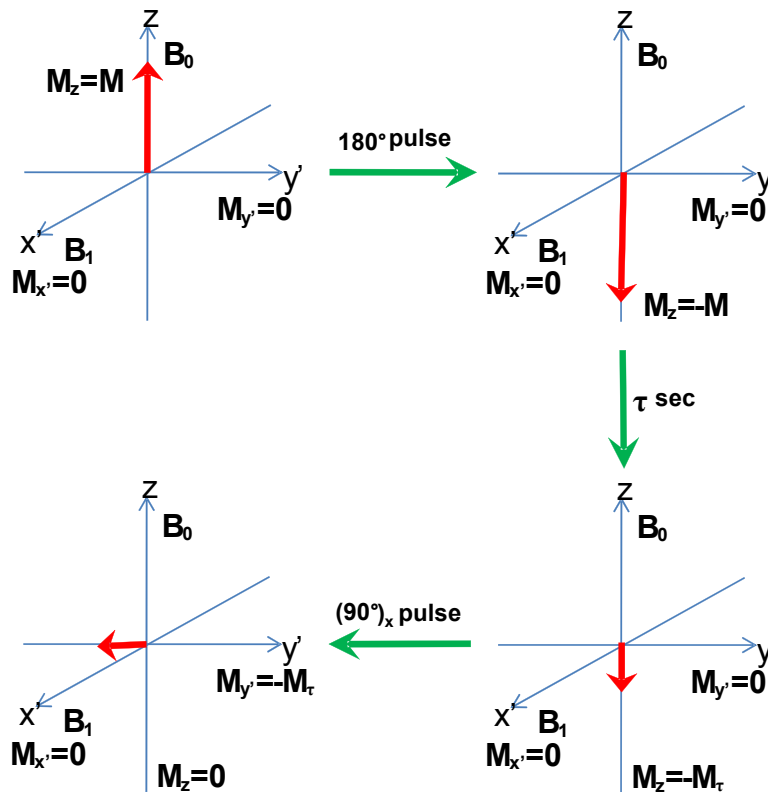
Figure 1.22 Inversion Recovery method for T_1 Measurement[54].

1.3   Systems Studied / Aims of Research

Given the unique and sensitive ability NMR has to examine the subtle structural and dynamic aspects of a system, we have undertaken to use this technique to answer some difficult questions regarding several complex ionically conducting solid oxide materials. First, a uniquely constructed, column-containing system, of the formula $Bi_{26}Mo_{10}O_{69}$ was studied for its unusual structure while being closely compositionally related to undoped bismuth oxides[76-83], bismuth tungstates and doped bismuth vanadates, the so called BiMeVOx's, all of which

have been found to be highly conducting. As though to parallel its structural uniqueness, this material demonstrated unexpected levels of ionic motion at a tremendously wide range of temperatures. The one dimensional techniques probing the gamut of motional processes as described above were necessary to fully understand the extent of motional timescales expressed by oxygens in this material. While two-dimensional spectroscopic techniques were undertaken to try to further probe slow motional processes in bismuth molybdate, they were unsuccessful as the T_1 relaxation was too rapid to allow for probing of chemical exchange in this way.

Next, the oxide conduction aspects of the parent as well as lanthanum and gallium doped forms of barium indium oxide ($Ba_2In_2O_5$) were examined in depth. While NMR spectra have previously been acquired of the end member of this material[13], a re-examination of one dimensional spectra at higher field strengths as well as MQMAS data revealed new structural information about this compound. Lanthanum and gallium doped analogs were examined by ^{17}O and ^{71}Ga NMR for the first time. Finally, proton conduction in hydrated analogs of doped and undoped barium indium oxide ($Ba_2In_2O_5 \cdot H_2O$) was examined by variable temperature NMR. As described above, proton conducting hydrates of oxide materials have been found to be very useful as electrolytes in intermediate temperature solid oxide fuel cells (ITSOFC). While proton spectra have been previously acquired for this system at room temperature[84], no interpretation as to the structural or dynamic implications of these spectra have yet been undertaken

until the current study. Detailed structural and dynamic analyses of each of these

systems are described in the following chapters.

Chapter 2

Variable Temperature ^{17}O NMR Study of Oxygen Motion in the Anionic Conductor $Bi_{26}Mo_{10}O_{69}$

Variable temperature ^{17}O NMR spectroscopy, spanning a temperature range from -238 to 1000 ºC, has been used to investigate mechanisms for ionic conduction in $Bi_{26}Mo_{10}O_{69}$, a material which contains both MoO_4^{2-} tetrahedra and $[Bi_{12}O_{14}]^{8-}_\infty$ columns. Two ^{17}O NMR resonances are observed which are assigned to oxygen atoms in the MoO_4^{2-} tetrahedra and in the $[Bi_{12}O_{14}]^{8-}_\infty$ columns. Based on the nutation curves for the two groups of resonances, extremely rapid, but local, re-orientational motion of the MoO_4^{2-} units occurs at -70 °C and above (with a frequency of > 50 kHz), while the Bi-O oxygen ions are rigid in this temperature regime. This is confirmed by both an analysis of the line broadening of the ^{17}O MoO_4^{2-} satellite transitions (under MAS) and the spin-lattice relaxation (T_1) times of these sites; the T_1 times indicating that the MoO_4^{2-} reorientation rates rapidly increase, reaching > 100 MHz at 400 °C. Line narrowing of the MoO_4^{2-} central-transition resonance indicates that exchange between the tetrahedral units, a motion required for long-range anionic conduction, is much slower, only involving jump rates of approx. 1 kHz at 200 °C. Both the changes in line width of the MoO_4^{2-} resonance, and the jump in the T_1 times of the oxygen atoms in the $[Bi_{12}O_{14}]^{8-}_\infty$ columns at around the triclinic-monoclinic phase transition temperature (310°C) are consistent with a mechanism for motion involving all the oxygen atoms. The predicted conductivity based on the [Bi-O] T_1 times is now of

the order of that extracted from *a.c.* impedance measurements reported by Vannier et al.[85] Based on this detailed NMR analysis, we propose that motion at ambient temperatures primarily involves the MoO_4^{2-} tetrahedral rotation: exchange between these sites is very slow. At higher temperatures, (above 310°C), the conduction process appears to involve the oxygen atoms coordinated to Bi^{3+}, in the $[Bi_{12}O_{14}]^{8-}_{\infty}$ columns, and most likely in the partially vacant O[19] site. The involvement of these sites allows for long-range conduction processes that do not involve concerted, multiple Mo-O bond breakages.

This chapter is adapted from a paper that is published in Chemistry of Materials[14].

1.1   Introduction

Anionic conductors are used in a growing number of applications including oxygen sensors in catalytic converters, membranes for oxygen/nitrogen separation and as electrolytes in solid oxide fuel cells, all of these applications requiring high O^{2-} transport. For the materials currently in use, conduction is very limited except at high temperatures (> 800°C). Even the widely employed yttrium stabilized zirconia (YSZ) exhibits rapid oxygen-ion motion only at temperatures above 700°C. Due to the practical difficulties and costs associated with the use of materials that can operate at these temperatures, it is important to identify electrolytes with higher levels of anionic conduction at lower temperatures and to understand the structural factors that promote this high conductivity. Currently, bismuth rich molybdates and vanadates (Bi/Mo(V) $\geq$ 2) have been shown to exhibit high oxide ion conductivity. Of these materials, the doped bismuth vanadium oxides (the so called BiMeVOx's Me = Cu, Co) have the highest oxide ion conductivity of any material yet reported[86]. The structures of the BiMeVOx's (and the related molybate Bi_2MoO_6) consist of defect Aurivillius phases composed of perovskite-like sheets comprising corner-sharing $VO_{6-\delta}^{(7-2\delta)-}$ (or MoO_6^{6-}) polyhedra alternating with $Bi_2O_2^{2+}$ layers. The motion predominantly occurs in the perovskite-derived sheets. Molybdates with an even higher Bi^{3+} content (solid solutions around the composition Bi/Mo~2.6) adopt a very different structure, which contains MoO_4^{2-} anions, and yet also show good anionic conductivity[85,87-90]. The purpose of the research described in this paper is to

investigate the nature of the local motion in the bismuth-rich material $Bi_{26}Mo_{10}O_{69}$, by using ^{17}O MAS NMR spectroscopy and to combine these results with longer probes of motion such as *a.c.* susceptibility. The parent composition, $Bi_{26}Mo_{10}O_{69}$, is a pure oxide ion conductor (i.e., there is a negligible electronic contribution) with a conductivity of 1 mS/cm at 500°C and a low activation energy of only 0.47eV. On cooling, it undergoes a phase transition at 310°C from a monoclinic to a triclinic structure, which is characterized by a decrease of the conductivity and a noticeable increase of the activation energy to 1.05 eV[85]. A solubility range of $2.57 \leq Bi/Mo \leq 2.77$ was determined for these materials by Vannier *et al.*[85] and confirmed by Buttery *et al.*[91] In contrast, Galy and coworkers, in their more recent work, reported a larger solid solution domain of $2.53 < Bi/Mo \leq 3.50$[92], which was larger than the values that they had originally proposed[90]. The skeleton of the structure is composed of MoO_4^{2-} tetrahedra interspersed with $[Bi_{12}O_{14}]_\infty$ columns and an isolated bismuth ion (Figure 2.1). The structure of $Bi_{26}Mo_{10}O_{69}$ at room temperature was refined in the P2/c space group by Vannier[85] and Buttrey.[91] The small triclinic distortion could not be taken into account in these refinements. Both groups observed full occupancy of the isolated bismuth site and suggested that an interstitial oxygen site must be present to ensure overall charge balance (with the Bi^{3+} and Mo^{6+} ions). This model was in good agreement with the density measurements (7.54 kg/m^3 compared to a calculated value of 7.53 kg/m^3)[85]. Large anisotropic displacement parameters for the oxygen atoms in the MoO_4^{2-} tetrahedra were observed when compared to those in $[Bi_{12}O_{14}]_\infty$ columns, suggesting that oxygen motion in

51

$Bi_{26}Mo_{10}O_{69}$ occurs within the Mo units. In their model, Buttery et al. located the extra oxygen site close to the isolated bismuth atom but obtained short O-O distances of 2.1Å. They also showed that the structure could be viewed as the intergrowth of fluorite-like bands and a "monoclinic variation of the cation arrangement". These monoclinic regions are very similar to the fluorite lattice and by comparing the structural model of "$Bi_{26}Mo_{10}O_{68}$" with the fluorite structure, Vannier et al. found a 4g empty site at ~0.45, ~0.40, ~0.15, which they labeled O(19)[87]. This O(19) interstitial site is coordinated to two Bi^{3+} atoms (Bi(4) and Bi(5)) and is located between two Mo(3)O_4 tetrahedra as shown in Figure 2.1a. Because of the short distances (2.5-2.9 Å) between oxygen atoms belonging to Mo(1)O_4 and Mo(3)O_4 tetrahedra and this interstitial site, an oxygen diffusion pathway along the [0 1 0] direction was proposed by these authors involving these tetrahedra and the O[19] site, as shown in yellow in Figure 2.1a. Because of the relatively long O-O distances between O atoms of the Mo(1)O_4^{2-} and Mo(2)O_4^{2-} tetrahedra, long range conductivity involving the Mo(1)O_4^{2-} tetrahedra, (i.e. in the a-c plane) was excluded. The materials were therefore proposed to be mono-dimensional oxide ion conductors, with conduction occurring along the directions of the columns (the b-direction). In contrast, Galy et al. proposed the following general formula to explain the solid solution extension, $Bi_{(2+x)/3}\square_{(1-x)/3}[Bi_{12}O_{14}][MoO_4]_{5-x}[BiO_3]_x$ with $0 \leq x \leq 1$, and viewed the structure as being built from MoO_4^{2-} and $BiEO_3$ tetrahedra (E being the bismuth cation lone pair) in $[Bi_{12}O_{14}]_\infty$ columns and an isolated bismuth ion[92]. The composition Bi/Mo=2.6 then corresponds to two $Bi_{0.695}\square_{0.305}[Bi_{12}O_{14}][MoO_4]_{4.913}[BiO_3]_{0.087}$ units per cell.

Note that this leads to a theoretical density of 7.40 kg/m^3 instead of 7.54 kg/m^3 measured by Vannier et al. The oxygen diffusion was suggested to occur via a cooperative mechanism along the [2 0 1] direction, in which all the MoO$_4^{2-}$ tetrahedra are involved, but no oxygen vacancies or interstitial sites (Figure 2.1b).
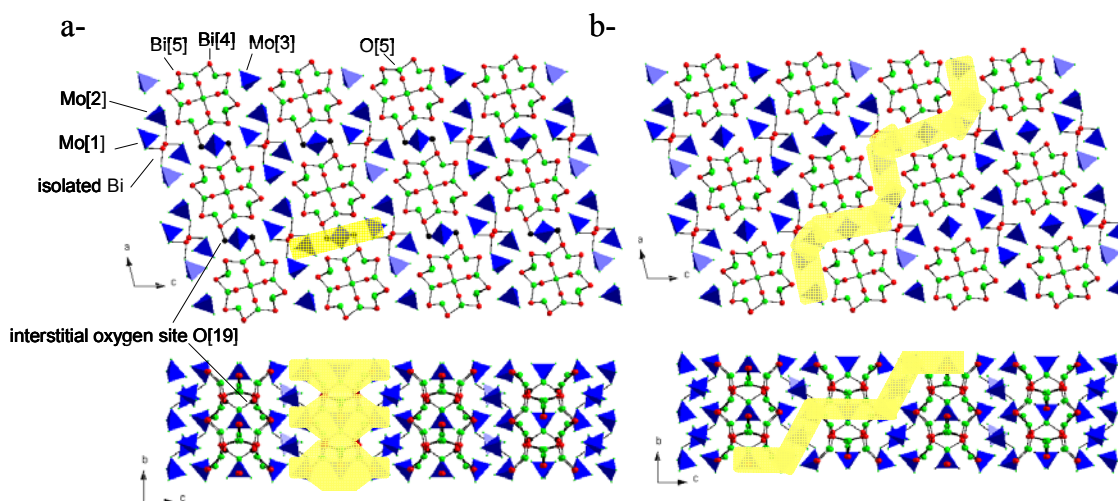
Figure 2.1 Structure of Bi$_{26}$Mo$_{10}$O$_{69}$ showing, in yellow, the preferential oxygen pathways proposed by a) Vannier et al[87]. and b) Galy et al.[89] in the a, c and b, c planes. Red spheres represent bismuth, green spheres represent oxygen and blue tetrahedra represent MoO$_4^{2-}$ units. The O(19) interstitial sites proposed by Vannier are indicated. Coordinates were taken from ref [87], bond lengths up to 2.36Å were used for the Bi-O connectivity.

The prior work on these systems highlights the complexity of both the structures of these materials and the conduction mechanisms. The mechanisms for conduction in this material remain controversial[85,87-90] and it is clear that further measurements are required to test the different models for conduction. While impedance studies have yielded the values for the long-range ionic motion, they cannot be used to determine the pathway(s) or the local dynamics responsible

53

for the conduction, nor do they provide information concerning which type of oxygen site is responsible for the motion. Also, while insight into the possible mobile species can be extracted from diffraction studies, this technique does not provide a direct measure of the exchange rates between different oxygen sub-lattices. To provide such information, ^{17}O NMR methods have been successfully applied to a wide range of ionic conductors[11,93]. For example, in our previous work[93] on the Aurivillius phase Bi_2WO_6, three resonances could be identified in the 1-dimensional magic angle spinning (MAS) NMR spectrum, which were assigned to oxygens coordinated solely to bismuth (O-Bi$_4$), tungsten (W-O-W), or bridging between both bismuth and tungsten (Bi-O-W) ions. Once the different species were identified, it was then possible to discern the different conduction pathways associated with these ions: Oxygen mobility in the tungstate layers was identified by variable temperature 1D MAS NMR, while slower exchange rates between the tungstate and bismuth layers was identified by two-dimensional (2D) magnetization exchange methods. Thus, the objective of the work presented here is to use ^{17}O NMR methods to determine the conduction mechanism and to establish how the unique structure of bismuth molybdate controls the movement of oxygen atoms in this compound. We apply a wide range of NMR spectroscopic techniques to investigate motion in $Bi_{26}Mo_{10}O_{69}$, as the hopping rates were found to span more than five orders of magnitude over the temperature range investigated. 2D magnetization exchange methods were not feasible due to very short spin-lattice relaxation times observed for this material. The results are combined with prior *a.c.* impedance measurements[85] which probe longer range

motion. We show that while the molybdate units are rotating extremely rapidly (with rates of ~ 2 MHz), even at room temperature, conductivity also involves exchange with the oxygen atoms coordinated to Bi^{3+} ions.

2.1 Experimental

Preparation, diffraction studies and *a.c.* impedance measurements of $Bi_{26}Mo_{10}O_{69}$ powder were described previously by Vannier et al.[85] ^{17}O enrichment was performed by heating a quartz tube containing a small quantity of the sample to 500° C in an $^{17}O_2$ environment (Isotec min. 50 atom %) for 24 hours. Room and high temperature MAS NMR experiments were carried out at SUNY Stony Brook at 67.78 MHz (11.7 T) on a Varian InfinityPlus-500 spectrometer equipped with a Chemagnetics 4mm HXY probe with pulse widths of 1.5 μs a pulse delay of 1 second, at a spinning speed of 15 kHz, and using approximately 30,000 scans. Ultra low and high temperature experiments were carried out at the National Institute of Chemical Physics and Biophysics in Tallinn, Estonia where low temperature MAS experiments were carried out at 48.8 MHz (8.45 T) on a Bruker AMX360 spectrometer with a Cryo-MAS™ 1.8 mm probe[94] built by the Samoson group[94,95], with pulse widths of 1.2 μs, a pulse delay of 2 seconds, at a spinning speed of 25 kHz using helium for bearing, drive and temperature control, and using approximately 200 scans. High temperature static experiments were carried out at 48.8 MHz on a Bruker AMX360 spectrometer with a home-built 5mm HX probe using pulse widths of 3.5 μs, a pulse delay of 0.1 seconds, and approximately 5600 scans. Ultra high temperature experiments were carried

out at the University of Warwick in Coventry, United Kingdom at 81.3 MHz (14.1

T) on a Bruker Avance II[+] 600 spectrometer equipped with a home built 7.5 mm

single channel probe[96] using a pulse width of 15 μs, a pulse delay of 0.1 seconds

and approximately 7400 scans. Experiments were performed with a rotor

synchronized Hahn-echo pulse sequence ($\pi/6 - \tau - \pi/3 - \tau$) to avoid probe ringing.

A one pulse experiment was used for the ultra high temperature experiments,

due to the poor signal-to-noise (S/N) at these temperatures. Nutation and T_1

experiments were performed by varying the pulse length and pulse delay,

respectively.

2.2   Results

2.2.1   Room and Low Temperature MAS NMR

The ^{17}O MAS NMR spectrum of $Bi_{26}Mo_{10}O_{69}$ is shown in Figure 2.2. While

there are nineteen different O crystallographic sites in this compound, only two

distinct resonances are observed at 200 and 570ppm. The resonance at 200

ppm is assigned to oxygen atoms coordinated to bismuth ions based on previous

^{17}O NMR studies by Yang et al.[97] of Bi_2O_3 (δ = 195ppm), and on our work on the

BiMeVOx[11] systems and Bi_2WO_6[93]/Bi_2MoO_6 where a shift of 242ppm was

observed for the oxygen ions in the $Bi_2O_2^{2+}$ layers. The resonance is broad due

to two effects, (a) the presence of 6 different O sites within the $[Bi_{12}O_{14}]_\infty$

columns, and (b) line broadening due to residual dipolar coupling to the nearby

quadrupolar, I = 9/2 ^{209}Bi nuclei[98] which are associated with extremely large

quadrupole moments. The isotropic resonance at 570ppm is assigned to

oxygens in the MoO_4^{2-} units based on work by Emery et al.[99] on $La_2Mo_2O_9$ (δ = 346-602ppm for MoO_4 groups), and in WO_4^{2-} units in ZrW_2O_8 (δ = 434, 561 & 734ppm)[100]. The 570ppm resonance is comprised of a sharper peak and a broader component in the baseline, the broader component presumably reflecting the distribution of local environments that arise from the 3 crystallographically-distinct MoO_4^{2-} groups (and hence 12 O sites) that contribute to this resonance. No significant change in the line width (in units of ppm) of the 570 ppm resonance was observed when the spectrum was acquired at a lower field strength (11.7 vs. 8.45 T), confirming that the line width is dominated by a distribution of chemical shifts, rather than 2nd order quadrupolar interactions. Broad sidebands are seen for the 200ppm resonance which spread over more than 6000 ppm; these are attributed to satellite transitions from this resonance. In contrast, the much sharper sidebands seen for the 570ppm resonance, which spread over 1800ppm, (Figure 2.2) are assigned to sidebands from both the central and satellite transitions of the MoO_4^{2-} ions. According to the structural model proposed by Vannier et al, the interstitial oxygen atom in the O[19] site is coordinated to one Bi^{3+} ion, and weakly coordinated to three MoO_4^{2-} units, and thus, is expected to resonate at a frequency intermediate between the two major groups of resonances. However, this site is only 25% occupied, and will therefore only account for only approx. 1.5% of the intensity. It is presumably too weak to be observed in these spectra, and/or is hidden under the spinning sidebands.
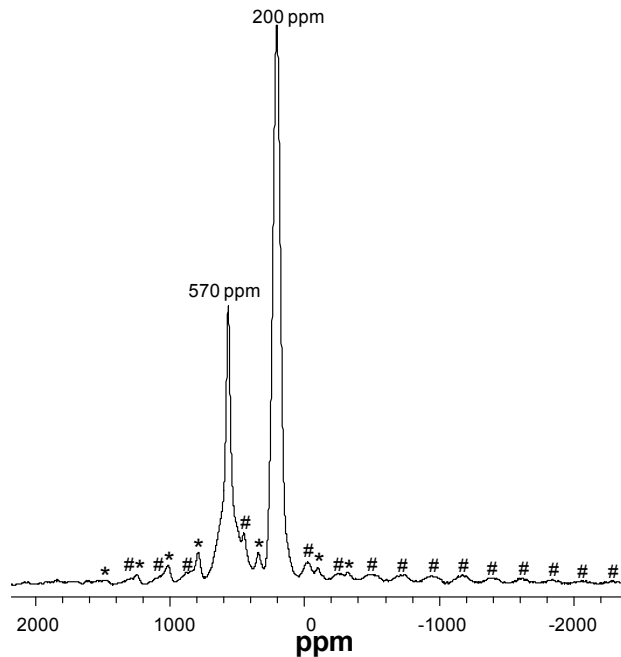
Figure 2.2 Room temperature ^{17}O MAS NMR echo spectrum of $Bi_{26}Mo_{10}O_{69}$ acquired with short ($\pi/6$; $\pi/3$) pulse widths and a pulse delay of one second at a spinning speed of 15 kHz at 67.7 MHz. Chemical shifts of the isotropic resonances are indicated in this and subsequent spectra. Sidebands from the 570 and 200ppm resonances are marked with "*", and "#", respectively. The broad resonances, seen clearly between – 200 and – 2000ppm are the satellite transitions from the 200ppm resonance. (N.b., satellite transitions are also seen at high frequencies; these are, however, much weaker due to the characteristics of the probe, which has an asymmetric tuning "dip"). On decreasing the temperature, no significant change in the line width of the $[Bi_{12}O_{14}]_\infty$ resonance is observed (Figure 2.3). In contrast, the sharp component of the MoO_4^{2-} resonance broadens, and a single broad (asymmetric) resonance is observed at -120 °C, indicative of a distribution of local

environments.
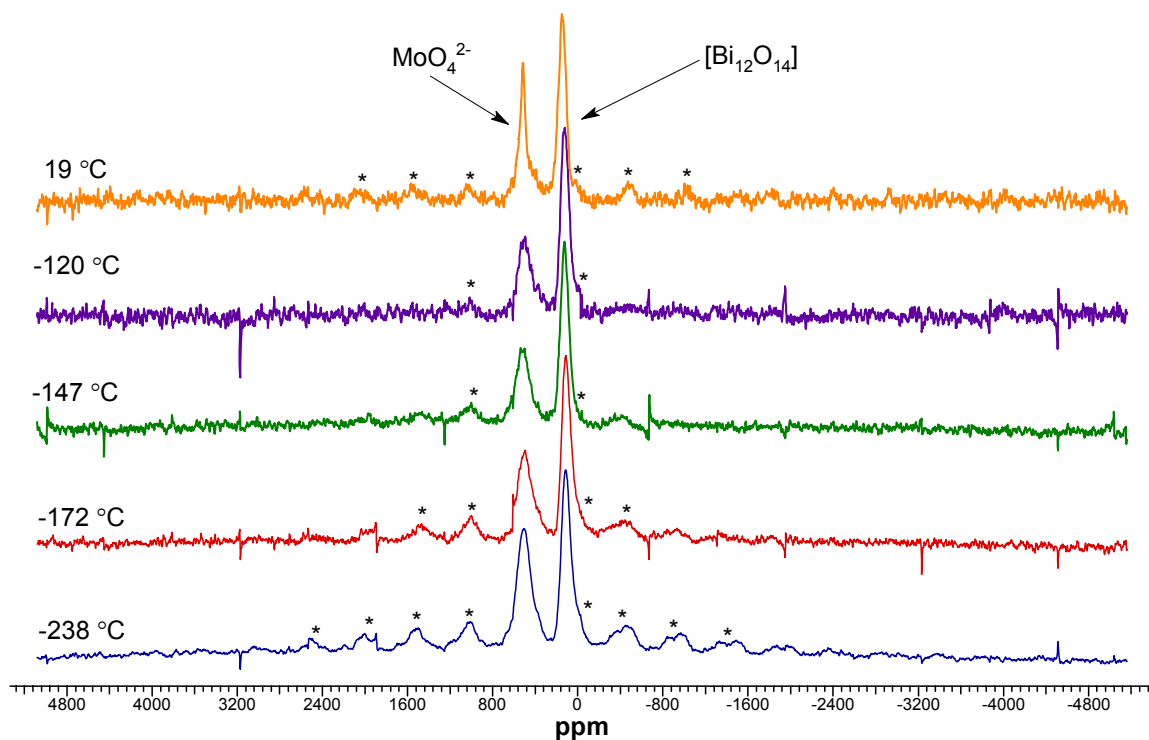
Figure 2.3 Variable low temperature ^{17}O MAS NMR spin echo spectra of $Bi_{26}Mo_{10}O_{69}$ at a field strength of 48.8 MHz and a MAS frequency of 25 kHz. Sidebands due to the MoO_4^{2-} groups are marked with asterisks. Small spikes in the spectra are most likely due to the instability of the low temperature spinning and the use of He as a spinning gas.

The line width of the isotropic resonances in a 1D NMR spectrum will be strongly affected if motion is present of the order of the frequency difference between the various resonances. When the hopping frequency of the O^{2-} anions between different sites approaches one half of this frequency difference, peak broadening is observed. With increasing exchange rates, the peaks broaden further and then coalesce producing a narrow resonance with a shift intermediate between those of the original resonances.[21] Thus, at room temperature, motional processes on the order of the low temperature line width of this resonance (2.12 kHz), involving

at least a subset of the MoO_4^{2-} oxygen atoms, must be present resulting in line-narrowing. More obvious, however, is the disappearance and reappearance of spinning sideband manifolds arising from the satellite transitions with decreasing temperature. In a MAS NMR experiment, slow re-orientational motion during the rotor period alters the evolution of the spin packets so that they no longer necessarily contribute to echo formation at the end of the rotor period in the free induction decay (FID) and in turn to the formation of spinning sidebands in the spectrum[101]. The timescale of this process is governed by the size of the anisotropic part of the interaction that broadens the resonance (for ^{17}O resonances, this is largely dominated by the quadrupole interaction and to a much lesser extent the dipolar and chemical shift anisotropies (CSA)) and the MAS frequency. Very slow motion of the ions on the order of the spinning frequency will cause a decrease in the intensity and eventually the disappearance of the spinning sidebands. Assuming random isotropic motion, the line broadening due to this mechanism, given by $1/T_2^*$, can be calculated from the following equation:[101]

$$T_2^* = 16(\omega_r / \delta\omega_0)^2 \tau_c$$

[2.1]

where $\delta\omega_0$ is the total (static) line width of the resonance or transition (in angular frequency). The line widths can be readily calculated from expressions for the 1st order quadrupolar interaction and for the inner and outer satellite transitions of an

I = 5/2 nucleus and are given by Q_{cc}*9/80 and Q_{cc}*9/40, respectively, where Q_{cc} is the quadrupole coupling constant = $e^2qQ/\hbar$. Unfortunately, the stability of the spinning speed at this temperature was not sufficient to allow spectra with well resolved satellite transitions to be acquired since the spinning speed instabilities tend to wash out the outer satellite peaks. Furthermore, there is considerable overlap between the satellite transitions of the Bi-O and Mo-O resonances at the spinning speed used at low temperatures (25 kHz). In addition, the width of the satellite transitions may be larger than the bandwidth of the probe. Thus it was not possible to extract an accurate value for Q_{cc}, directly from the low temperature ^{17}O MAS NMR spectra. Based on the line width of the *observable* sideband manifold of approx. 8000ppm (0.39 MHz) an estimate for the Q_{cc} of 1.6 MHz is obtained (assuming η = 0), which will represent a lower limit. This value is consistent with typical ranges for the ^{17}O Q_{cc} of 0.5-2.0 MHz, for ions in these types of environments,[13,93,100] but is larger than the Q_{cc} of 0.5 MHz observed for the WO_4^{2-} groups of ZrW_2O_8[24]. This Q_{cc} value was then used to estimate a value for the motional timescale required to prevent refocusing of the rotor echoes and thus for the progressive loss of the satellite transitions above -202°C. Assuming that the sidebands start to disappear into the baseline when the line-broadening is similar to the spinning frequency, jump frequencies of approximately 1.9 kHz are required for the disappearance of the outer satellites (at approx. -172°C) and 7.7 kHz for the disappearance of the inner satellites (at approx. -147°C). A much smaller set of sidebands is seen at room temperature, indicating that motion on a timescale that is larger than the Q_{cc} of the rigid Mo-O oxygen ions, has resulted

in partial averaging of the electric field gradient (EFG) and thus the observation of a reduced Q_{cc}. Only at -238°C does even the slowest ionic motion cease to affect the refocusing of the rotor echoes.

2.2.2 Nutation Spectroscopy
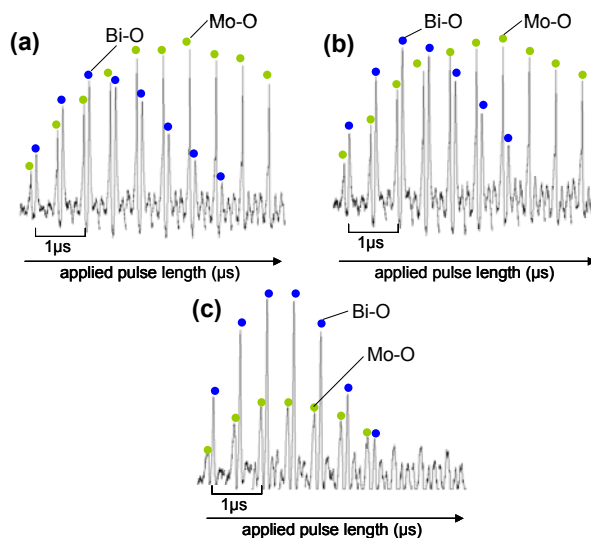
Figure 2.4 ^{17}O NMR nutation curves for $Bi_{26}Mo_{10}O_{69}$ for oxygens bonded to bismuth atoms (blue circles) and molybdenum atoms (green circles) at a) -40°C, b) -70°C, and c) -150°C. Spectra are plotted as a function of the pulse length. The pulse length was incremented in steps of 0.5 μs from 0.5 to 5.0 μs.

For quadrupolar nuclei such as ^{17}O, the frequency at which the spins nutate about an applied radio frequency (rf) field (with field strength ω_1) is strongly dependent on the size of the quadrupole frequency (ω_Q) (where ω_Q is given by $(3/20)Q_{cc}$ for a I = 5/2 nucleus).[102] For quadrupolar spins in local environments where $\omega_Q < \omega_1$, (i.e., liquid samples or in solids having environments with inherently small quadrupolar couplings, or ones where rapid re-orientational motion averages out the quadrupolar interaction), all the 2I transitions can be efficiently excited. The nutation frequency is then identical to that observed in the

spin-1/2 system and is given by ω_1. For (rigid) local environments associated with large quadrupole coupling constants (Q_{cc}), where $\omega_Q \gg \omega_1$, only the central transition ($+\frac{1}{2} \rightarrow -\frac{1}{2}$) of a non-integer spin nucleus is efficiently excited. This partial excitation of the spin system leads to a nutation curve which has ($I + \frac{1}{2}$) (i.e., three for ^{17}O) times the frequency but only $1/(I + \frac{1}{2})$ times (i.e. one third for ^{17}O) the amplitude as compared to the above case where all transitions are excited. In this large quadrupole frequency regime, the rf pulse necessary to excite the spin system such that the magnetization is tipped by 90°, is 3-times shorter than the $\pi/2$ pulse measured for a liquid (e.g., $H_2{}^{17}O$). The nutation frequency for oxygens associated with bismuth sites in $Bi_{26}Mo_{10}O_{69}$ is approximately three times that of the liquid reference for all temperatures indicating that $\omega_Q \gg \omega_1$ for this site (Figure 2.4). From this it can be inferred that no ionic motion occurs on the order of the nutation frequency (50 kHz) to result in averaging of the quadrupolar interactions for these sites. In contrast, the nutation frequency of the $MoO_4{}^{2-}$ oxygens is similar to that of the liquid reference, at room temperature (not shown), -40 and -70°C, indicating that at these temperatures the effective or averaged value of ω_Q (in the timescale of the nutation experiment) is less than ω_1. At -150°C, however, the nutation rate of this site increases so as to approach that of the rigid Bi-O site, and the Mo-O spin-system approaches the regime where $\omega_Q \gg \omega_1$. Thus, the nutation curves indicate that at -70°C and above, oxygen re-orientational motion must be occurring on a timescale that is much faster than the timescale of the nutation frequency (i.e., $\gg$ 50 kHz), so as to result in averaging of the quadrupolar interaction.

2.2.3 High Temperature NMR
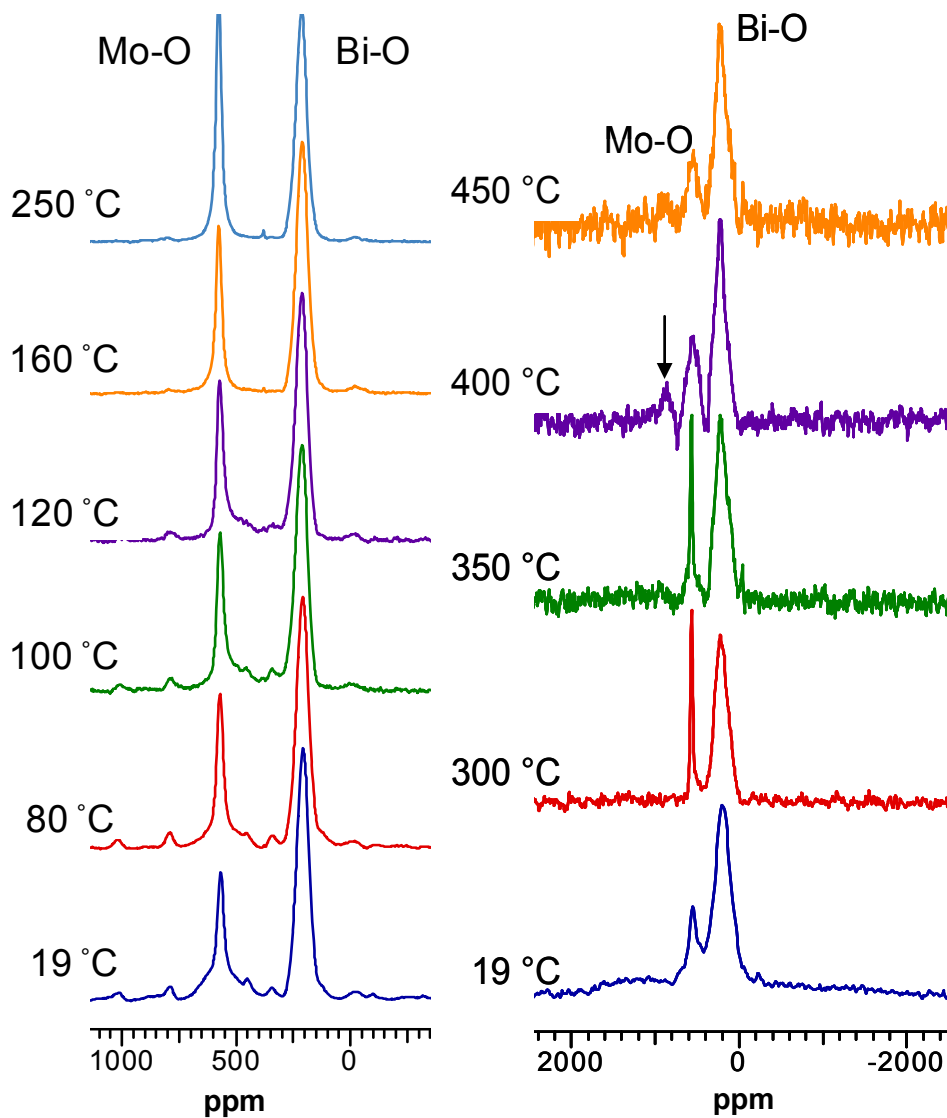
Figure 2.5 High temperature ^{17}O NMR spectra of $Bi_{26}Mo_{10}O_{69}$ acquired at a Larmor frequency of 48.8 MHz. Left: MAS NMR spectra from room temperature to 200°C. Right: static spectra to 450ºC. The arrow in the 400°C spectrum indicates the peak that is tentatively assigned to the $|3/2> - |1/2>|$ satellite transition.

The high temperature MAS and static ^{17}O NMR spectra presented in Figure 2.5 show that the Bi-O peak remains relatively unchanged while the broad component of the MoO_4^{2-} resonance in the MAS spectra narrows significantly above room temperature resulting in a single, sharp resonance at 160°C, which indicates that all the oxygen atoms of the MoO_4^{2-} units are undergoing very rapid motion at high temperatures. Two types of motion should be distinguished, re-orientational motion within the tetrahedra and O exchange between the tetrahedra. The former motion will not contribute (directly) to long-range ionic conductivity. The nutation data and spinning sideband data suggest that at least one of these motional processes is occurring extremely rapidly (with a hop frequency > 50 kHz, even at -70°C). At room temperature, however, a broad line width is still observed (in both the static and MAS spectra) with a line width of 2.12 kHz (MAS), indicating that rapid motion involving all 12 crystallographically distinct Mo-O oxygen atoms cannot be occurring at this temperature, and that there must be a distribution of correlation times for Mo-O motion. This is not inconsistent with the nutation curves presented in the previous section, since these are likely to be dominated by the more rapidly rotating ions, as these are associated with sharper resonances. It is difficult to follow the nutation behavior of the broader resonances, given the poorer S/N of the lower temperature spectra. The results strongly suggest that the rapid motion is likely only occurring within the tetrahedra, since this would result in an effective mechanism for reduction of the quadrupolar interaction (this hypothesis will be confirmed by a comparison with long-range measurements of conductivity, discussed in a later

section). Given that there are three crystallographically distinct MoO_4^{2-} units in the unit cell, rapid rotational motion within units, but not between units, would, in principle, result in the observation of three distinct resonances, the chemical shift of each resonance reflecting the average value for the 4 oxygens in each individual tetrahedral unit. The observation of only a single resonance at 160°C, which sharpens considerably up to 350ºC suggests that exchange is also occurring between the units, on a timescale that is larger than the separation between the four resonances, at this temperature. Since we are not able to observe and assign the resonances from the individual tetrahedra it is difficult to extract an accurate value for the correlation time of this slower motion. However, given the line width of the MoO_4^{2-} resonance at low temperatures (2.1 kHz), motion is likely occurring with a rate greater than this frequency, at 160ºC and above. Above 350°C, significant broadening and loss of intensity of the MoO_4^{2-} resonance can be seen. We tentatively ascribe this phenomenon to the onset of another motional process, possibly involving exchange not only with other oxygens in molybdenum environments, but also with those in bismuth environments. However, this broadening could also possibly be due to other dynamic processes such as the collapse of the satellite transition resonances into the central transition resonance due to the onset of *isotropic* motional processes occurring at a frequency greater than the Q_{cc}. This latter suggestion, however, does not appear to be consistent with the appearance of a small peak at a higher frequency than the Mo-O peak, at 350°C, which is ascribed to contributions from the inner satellite transitions, involving the m = | |3/2> | and |

|1/2> | states with its lower frequency counter-part resonance buried underneath the Bi-O peak. These satellite transitions may give rise to the broad resonance visible in the room temperature spectrum, which then disappears at higher temperatures due to motion. Assuming an asymmetry parameter of 0, an estimate for the Q_{cc} of 250 kHz may be obtained from the position of this peak maximum. The reduced but non-zero Q_{cc} seen at this temperature for the rapidly rotating Mo-O groups is ascribed to the electric field gradients still present at the tetrahedral sites in this highly anisotropic solid with its one-dimensional Bi-O columns.
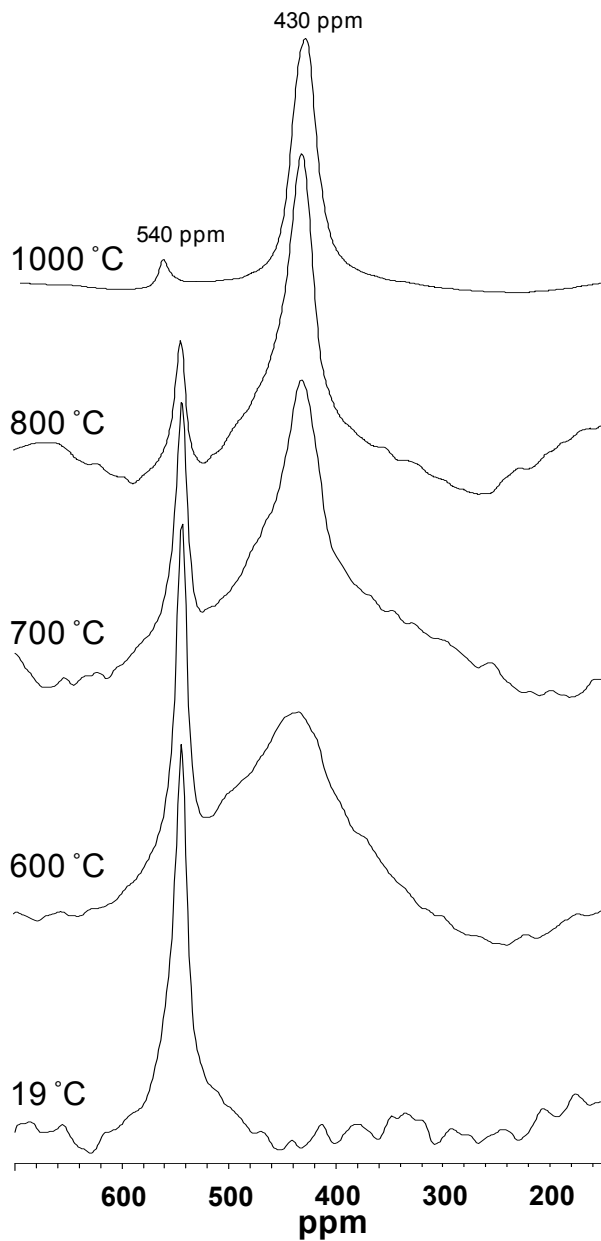
Figure 2.6 Comparison of room and ultra high temperature single pulse ^{17}O NMR spectra of static $Bi_{26}Mo_{10}O_{69}$ acquired at a field strength of 81.3 MHz. In the room temperature spectrum, only the Mo-O42- peak is visible. This is believed to be because the signal for the broad Bi-O peak dies quickly and may be lost in the dead time of the probe.

The chemical exchange between the Mo-O and Bi-O sub-lattices is confirmed by

the ultra-high temperature static ^{17}O NMR spectra seen in Figure 2.6. The Bi-O

peak, at 200ppm at room temperature, has completely disappeared, and instead

a resonance at a frequency intermediate between that of the Bi-O and Mo-O resonances (430ppm) is observed at 600°C. Coalescence occurs when the frequency of hops between the two sites ($1/\tau_c$) is greater or equal to $2^{-\frac{1}{2}}\pi\nu_{AB}$, where ν_{AB} is the frequency separation between the two resonances (Mo-O and Bi-O), i.e., $1/\tau_c \geq 55$ kHz for bismuth molybdate at 600°C. Continued line-narrowing of the 430 ppm resonance occurs as the temperature increases up to 1000°C, indicating a further increase in the rate of Bi-O, Mo-O exchange. A weaker resonance due to the MoO_4^{2-} groups is observed, which diminishes in intensity as the temperature is raised. Thus, there is a distribution of correlation times for Bi-O, Mo-O exchange: not all of the MoO_4^{2-} groups are involved in the rapid exchange process, even at these elevated temperatures. This is an important observation, because it indicates that rapid exchange (where rapid is defined as >> 55 kHz) between *all* the MoO_4^{2-} groups cannot be occurring even at 1000°C. If rapid exchange between all the MoO_4^{2-} groups was indeed occurring, along with a distribution of correlation times for exchange Bi-O, Mo-O exchange, then all the MoO_4^{2-} oxygen-ion are rendered equivalent in the timescale of the Bi-O, Mo-O exchange. In this case, the MoO_4^{2-} resonance would be expected to shift gradually from its ambient temperature position (540ppm) to higher frequencies as more and more Bi-O oxygen atoms exchange with the Mo-O oxygen atoms with rates approaching 55 kHz. This phenomenon was observed previously in spectra of LaF_3 and Sr^{2+}-doped LaF_3[12]. Surprisingly, no residual resonance remains at 200ppm, indicating that all the Bi-O oxygen atoms, even in the center of the columns, undergo exchange.

2.2.4 Spin-Lattice Relaxation Times
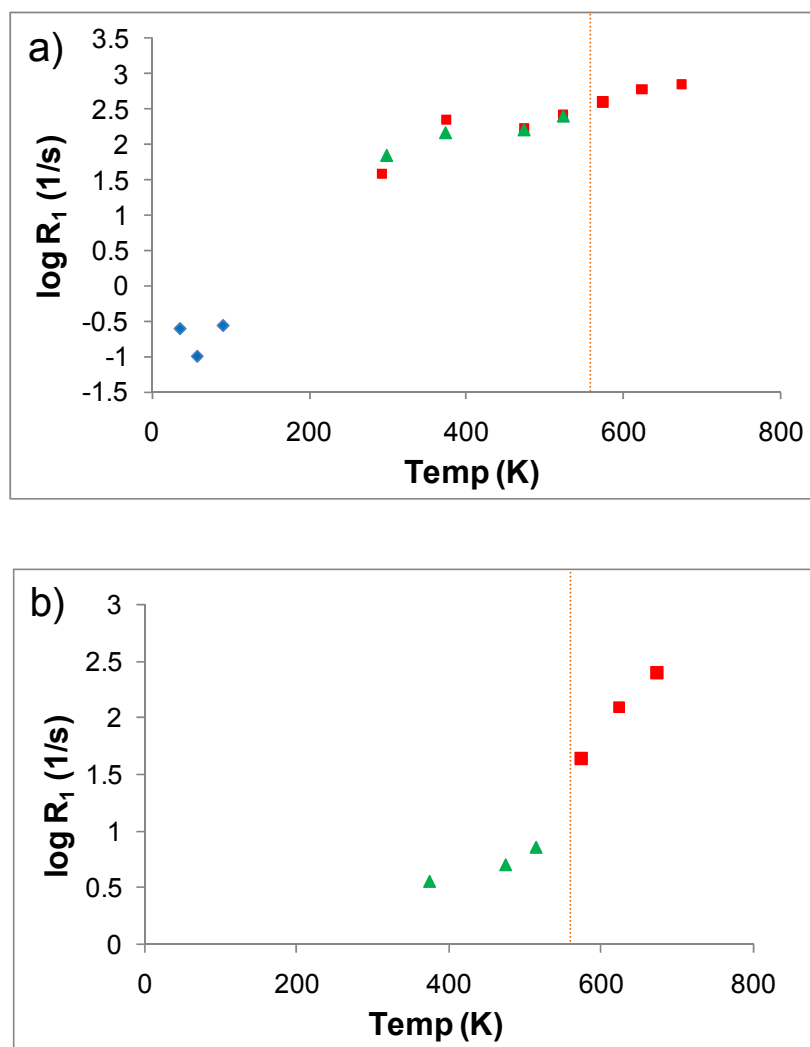
Figure 2.7 Relaxation rates, R_1 ($1/T_1$) versus temperature for oxygens in (a) molybdenum environments and (b) bismuth environments in $Bi_{26}Mo_{10}O_{69}$. Blue diamonds represent data acquired on the 1.8mm MAS cryostat probe, green triangles represent data acquired on a 4mm MAS probe, red squares represent data acquired on a 5mm static high temperature probe. Orange dashed line indicates the phase transition temperature.

Very fast moving ions on the order of the Larmor frequency (ω_0; typically 10-100 MHz for ^{17}O) will influence the longitudinal (T_1) relaxation time. In principle, ^{17}O

70

relaxation can be driven by two different mechanisms:[62] quadrupolar and/or magnetic. Quadrupolar relaxation, as a general rule does not follow a single exponential decay process, due to the possibility of different transition rates between the different spin-states $|m_I\rangle$ [62] (see Yesinowski *et al.* and Suter *et al.* for recent discussions of this phenomena[103,104]). The relaxation time of a non-integer spin quadrupolar nucleus will be the sum of I + ½ decaying exponential terms[60,61,102], i.e., for I = 5/2 nuclei such as ^{17}O, the relaxation process will involve three exponential terms. However, the relative contribution of the different terms depends on both how the spin-system is initially excited and the relative importance of the transition rates W_n involving single (ω_0) and double quantum transitions ($2\omega_0$), W_1 and W_2, respectively. For excitation of the central transition only (i.e., $\omega_Q \gg \omega_1$) and assuming that $W_1/W_2 = 1$ an expression of the form[105]

$$I(t) = I - 0.029e^{(-0.8W_1 t)} - 0.794e^{(-1.5W_1 t)} - 0.178e^{(-3.3W_1 t)}$$

[2.2]

is derived. If the correlation time is short, *i.e.*, when the electric field gradients are fluctuating much more rapidly than the Larmor frequency, however, as occurs in a liquid, the decay expressions will collapse to a single exponential[61]. In diamagnetic systems, the quadrupolar mechanism generally dominates[106], due to the much larger sizes of the fluctuating fields caused by the quadrupolar interaction than by for example, the dipolar coupling to nearby mobile ions, or the chemical shift anisotropy. Magnetically driven relaxation occurs primarily when

there is a high density of paramagnetic relaxation centers or if the nuclear quadrupole moment is sufficiently small such that the quadrupole relaxation mechanism cannot compete. In their studies of zirconium tungstate, a compound that contains mobile WO_4^{2-} ions, Hodgkinson and Hampson somewhat surprisingly concluded that their ^{17}O T_1 data was better fit to a model based on a magnetic relaxation mechanism, where the relaxation was driven by motion of other ^{17}O nuclei[23,100]. However, given the complexities introduced by multi-exponential T_1 relaxation they acknowledged that it would be difficult to use ^{17}O NMR to distinguish between these mechanisms as they have such similar overall effects. The analysis of their system was further complicated by the relatively slow exchange that occurs between the different oxygen ions in the WO_4^{2-} ions, so that the overall relaxation was a sum of multiple different rates. Given the complexity involved in interpreting relaxation data, several groups have used a stretched exponential function to describe a distribution of relaxation times[73] :

$$M(\infty) = M(t(1 - e^{[-(t/T_1)^{\beta}]}))$$

[2.3]

where β is the stretch exponent with $0 < \beta \leq 1$. While lacking the physical significance of some of the more sophisticated fittings, this method does represent a convenient and practical model for characterizing non-exponential relaxation in solids. It is also a reasonable approximation because, even in representations that consider more than one rate, the relaxation process is

generally dominated by a single rate (i.e., $1.5W_1$ in equation [2.2]). Thus, we have chosen to use this approach in this work. T_1 relaxation rates ($1/T_1$) were calculated by using equation [2.3] and are plotted as a function of temperature for the oxygens in the two environments of $Bi_{26}Mo_{10}O_{69}$ in Figure 2.7. Stretched exponents, β, of close to 0.5 were required to fit the T_1 data, reflecting both the large numbers of crystallographic sites (presumably each with slightly different correlation times for motion and different Q_{ccs}), and the complex nature of the ^{17}O relaxation processes. Both oxygen environments are associated with relaxation rates that increase with temperature, gradually at low temperatures and then much more rapidly above 310°C, the triclinic-to-monoclinic phase transition temperature. However, there is a far more profound discontinuity in the relaxation rates for oxygens in bismuth environments than for those in molybdenum environments at this phase transition temperature. The rapid relaxation times for the Bi-O ions at high temperatures are surprising as both the static and MAS spectra are not consistent with motion for these ions on the Larmor frequency timescale. Two mechanisms can be envisaged that will result in rapid T_1 relaxation. First, the Bi-O oxygen atoms, although not mobile themselves, will nonetheless experience fluctuations in the electric field gradients, due to rapid motion of nearby charged ions. This mechanism was previously proposed to explain the short T_1 times seen for $[Bi_2O_2]^{2+}$ O ions in doped Bi_2WO_6 in temperature regimes where they are not themselves mobile[93] and for the rigid oxygen-sub-lattices of Zr-doped $Ba_2In_2O_5$[107]. A second mechanism involves the exchange between the Bi-O and Mo-O ions, the T_1 relaxation rate representing a

73

measure of the exchange rate between the two sub-lattices. This mechanism was shown to be responsible for the short relaxation times of F^- ions in the "rigid" BaF_2 sub-lattice of $BaSnF_4$[9]. Undoubtedly, the first mechanism will contribute in part to the gradual decrease in the T_1 time with temperature, and the decrease should track the decrease in the Mo-O relaxation times directly. The discontinuity in the Bi-O relaxation rates (but not in the Mo-O rates) at the phase transition cannot, however, be ascribed to this mechanism, and it strongly suggests that exchange between the Bi-O and Mo-O sub-lattices must also be occurring. This observation is consistent with the line shape changes of the Mo-O resonances seen in Figure 2.5 in this temperature regime and the coalescence seen for the Mo-O and Bi-O resonances at higher temperatures.

2.3   Discussion

2.3.1   Interpretation of the T_1 data; implications for local and long range motion:
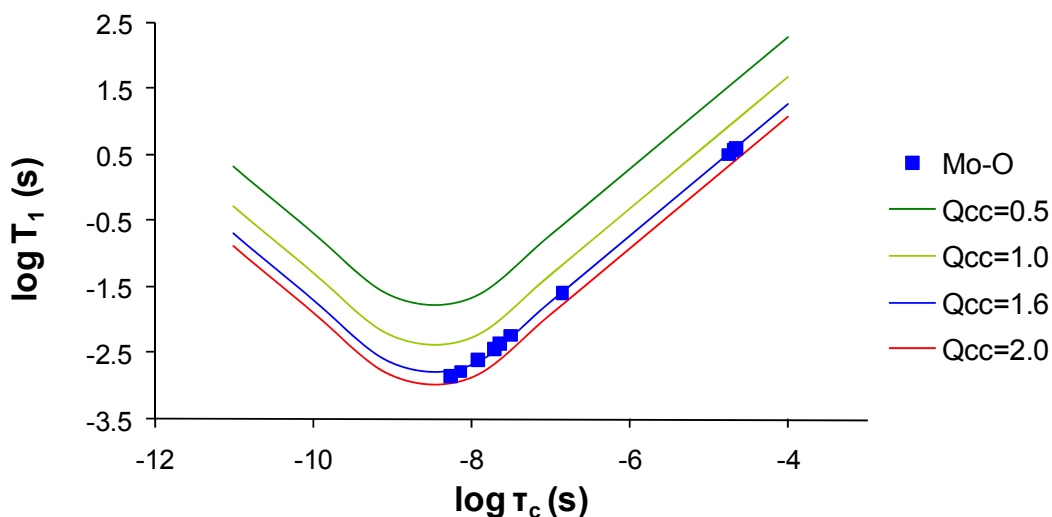
Figure 2.8 ^{17}O NMR T_1 relaxation time for oxygen nuclei in molybdenum environments in $Bi_{26}Mo_{10}O_{69}$ at 8.5 T vs. calculated correlation times with a quadrupole coupling constant of 1.6 MHz. General T_1 vs. τ_c curves for a 5/2 system at a field of 8.5 T, from top to bottom calculated with Q_{cc} = 0.5, 1.0, 1.6 and 2.0 MHz respectively. The blue squares represent the experimental data in the temperature range from 35 to 673 K.

The relaxation data can be used to extract a correlation time, τ_c, (τ_c = 1/ hop frequency) for the motion that drives the increase in relaxation, via equations of the form:

$$\frac{1}{T_1} = \frac{3}{625} Q_{cc}^2 \left(1 + \frac{\eta^2}{3}\right) \left[\frac{a\tau_c}{1 + \omega_L^2 \tau_c^2} + \frac{4b\tau_c}{1 + 4\omega_L^2 \tau_c^2}\right]$$

This equation is specific to a spin 5/2 system and assumes that the major driving force for relaxation comes from the quadrupole interaction, quantified via Q_{cc} and the asymmetry parameter, η. The numerical coefficients a and b reflect the geometric details of the motion, and the multi-exponential character of the decay (e.g., the W_1/W_2 ratio, the state of the initial spin system etc.). a = b = 1 in the case of rapid fluctuations of the EFG tensor; this is assumed in this work, which although an approximation, allows approximate orders of magnitude for τ_c to be extracted. The T_1 relaxation times for the molybdenum oxygen environment are plotted versus correlation time, calculated from equation [2.4] in Figure 2.8. A quadrupole coupling constant of 1.6 MHz was assumed, which represents the estimate for the Q_{cc} made based on the low temperature MAS data, and then fitted to the calculated general curve for a 5/2 system at this field. As demonstrated via calculating general T_1/τ_c curves for other Q_{cc}'s, as shown in this figure, Q_{cc} values of smaller than 1.6 MHz do not result in a sufficiently large reduction in the τ_c. Thus, this Q_{cc} value also represents the minimum possible value for the Q_{cc} required to produce the experimentally observed decreases in the T_1 time for the Mo-O sites, assuming that the quadrupolar relaxation mechanism represents the dominant relaxation mechanism. Since no clear T_1 minimum is observed in the data, we cannot exclude the possibility that the Q_{cc} is actually slightly larger. As illustrated in Figure 2.8, an increase in the Q_{cc} from 1.6 to 2.0 MHz, results in a change in calculated correlation time, τ_c by approximately

55%. The Q_{cc} cannot be significantly larger than 2.0 MHz, because we did not observe any evidence for broadening of the isotropic (central transition) resonance, due to the second order quadrupolar interaction, even at the lower magnetic field strengths. The hop frequencies extracted from these T_1 measurements are surprisingly large, varying from 12 kHz at -238°C, ~5 MHz at room temperature and 78 MHz at 400°C. These values are consistent with the hop frequencies estimated based on the analyses of the nutation curves and the line widths of the spinning sidebands at lower temperatures. Furthermore, the higher temperature values are consistent with the averaging of the first order quadrupolar interaction and the reduction of the Q_{cc} from approx. 1.6 MHz to 250 kHz, indicating that motion on the MHz timescale is occurring at these temperatures. Errors in our assumption concerning the two constants, a and b, in Equation [2.4] do not affect these general conclusions. If we assume that b = 0, no noticeable change in the calculated hop frequency is observed. The Bi-O hop frequencies were similarly calculated by assuming a Q_{cc} for this site of 1.6 MHz, this value for the Q_{cc}, (as for the Mo-O sites) representing the minimum size of the Q_{cc} fluctuation required to produce the experimentally observed T_1 values.

2.3.2   Comparison between long- and short-range motion:
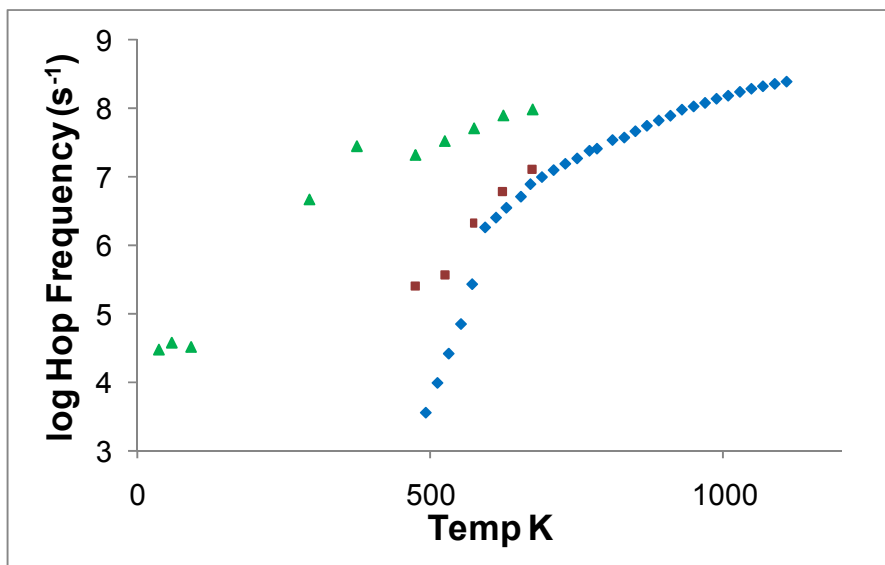
Figure 2.9 Comparison of oxygen hop frequencies versus temperature calculated from conductivity data[85] with those calculated from NMR T_1 data for Bi-Os site and Mo-O sites. Blue diamonds = hop frequencies calculated from conductivity measurements; green triangles = hop frequencies calculated from relaxation data on Mo-O site; red squares = hop frequencies calculated from relaxation data on Bi-O site.

We now compare the hop frequencies for oxygens at various temperatures determined by NMR, with those calculated from conductivity measurements in order to determine if the motion causing the effects in the NMR experiments is due to long-range or local movement of the ions. The hop frequencies for motion that contributes to long-range conductivity can be calculated from conductivity measurements using the Nernst-Einstein equation:

$$\sigma \frac{k_B T}{N q^2} H_R = D^T$$

[2.5]

And the Einstein-Smoluchowski relationship:

78

$$\tau_c^{-1} \frac{r^2}{6} f = D^T$$

<div align="right">[2.6]</div>

where σ is the conductivity, H_R is the Haven ratio, q is the charge, T is the temperature, N is the number of charge carriers, k_B is the Boltzmann constant, D^T is the tracer diffusivity, f is the correlation factor and τ_c^{-1} is the hop frequency. The hop frequencies obtained from these equations and previous conductivity measurements for this system[88] are compared with those obtained from the T_1 relaxation data in Figure 2.9. We assumed a Haven ratio and correlation factor of 1, a jump distance of 3 Å, representing the average distance between MoO_4^{2-} units, that O^{2-} is the only charge carrier contributing to conductivity. While these assumptions may not be justified at all temperatures, the jump rates calculated from the conductivity measurements are less than those calculated from the NMR relaxation data of the Mo-O site by several orders of magnitude, a conclusion that is not affected by these assumptions. This result indicates that the very rapid oxygen motion of the Mo-O tetrahedra causing the NMR relaxation is most likely localized and does not contribute to long-range conductive hopping at low-intermediate temperatures. The jump rates of the O ions on the Bi-O sites, as measured by the NMR relaxation data do, however, approach those calculated from conductivity data at higher temperatures, strongly implying that the two methods do in fact examine the same motional processes. This is provides further support for our proposal that the high temperature, long-range

conductive process in this material involves exchange between oxygens ions bonded to the molybdenum and those bonded to bismuth ions.

2.4   Conclusions: Implications for Motion in $Bi_{26}Mo_{10}O_{69}$

The rates of oxygen motion for two major types of oxygen environments in $Bi_{26}Mo_{10}O_{69}$ have been determined by a wide variety of ^{17}O NMR methods, over an extremely large range of temperatures. Nutation studies, analysis of the changes in line widths of the satellite transitions and T_1 relaxation data, all *consistently* indicate that very rapid motion, with associated jump frequencies on the order of 10^4-10^5 Hz commences even at very low temperatures. For example, analysis of the sideband manifolds indicates that hop frequencies greater than 2 kHz at -172°C, and 7 kHz at -147°C are occurring. This motion becomes extremely rapid above room temperature, the relaxation data indicating that motion of the order of 30 MHz occurs at 100°C; the observation of a reduction in the Q_{cc} on the timescale of the quadrupolar interaction at 300°C also suggests that motion on the MHz timescale is occurring. Despite this evidence for extremely rapid motion, coalescence of the broad and narrower components of the MoO_4^{2-} *isotropic* resonance only occurs above 160°C, indicating that not all of the oxygen ions in the MoO_4^{2-} groups undergo rapid chemical exchange with each other (i.e., rapid inter-tetrahedral exchange is not occurring between all the ions). Furthermore, long-range (*a.c.* conductivity) measurements in this temperature regime are consistent with hop rates between MoO_4^{2-} ions that are

almost four orders of magnitude less than the hop rates extracted for these ions from the relaxation data (e.g., a hop rate between O sites of only 3.5 kHz is calculated at 200°C from the *a.c.* conductivity data (Figure 2.9)). We therefore, ascribe the more rapid motion to the rotation of the individual MoO_4^{2-} tetrahedra. This is consistent with the large thermal parameters seen for the Mo-O oxygen atoms in the structural refinements[85] and indicates that the thermal parameters do not necessarily provide a good measure of the sub-lattice and mechanism responsible for long-range anionic conductivity. This extremely rapid MoO_4^{2-} rotation is most likely assisted by the presence of lone pairs on the Bi^{3+} ions, which point directly towards the MoO_4^{2-} tetrahedra. This motion does not directly give rise to long range conductivity. Long-range anionic conductivity in this temperature range is ascribed to slow exchange between the MoO_4^{2-} tetrahedra (on the order of > 2 kHz at this temperature). The mechanism by which this occurs is discussed below. At 350°C, above the phase transition, exchange occurs between the Mo-O and Bi-O sub-lattices, as indicated by the increase in the Mo-O line width, the noticeable increase in the Bi-O T_1 relaxation rate, and the approach towards coalescence of the Bi-O and MoO_4^{2-} resonances at 600°C. No Bi-O resonances remain, indicating that oxygen exchange between the ions in the center and outer shell of the $[Bi_{12}O_{14}]_\infty$ columns occurs. These columns adopt the fluorite structure, which is also the structure of the high temperature form of Bi_2O_3, δ-Bi_2O_3, which similarly exhibits high oxide ion conduction[109]. Once an oxygen vacancy is introduced into the Bi-O lattice, the proposal that oxygen diffusion occurs appears to be quite reasonable[79,110-115]. In this temperature

regime, the hop frequencies of the Bi-O oxygen atoms and those calculated from the *a.c.* impedance measurements approach each other. Taken together, these observations strongly suggest that the long range conductive processes now start to involve the Bi-O sites, even in the $[Bi_{12}O_{14}]_\infty$ columns. However, there is no evidence for rapid exchange within the $[Bi_{12}O_{14}]_\infty$ columns before the onset of the Bi-O and Mo-O exchange indicating that long range conductivity cannot be ascribed to motion only involving the $[Bi_{12}O_{14}]_\infty$ columns. Finally, both a jump in the long-range conductivity (by almost an order of magnitude) and a decrease in the activation energy are seen at the phase transition temperature[87], also suggesting that different conductivity mechanisms are operating above and below the phase transition temperature, with an increasing number of charge carriers at elevated temperatures. Long-range motion involving only the MoO_4^{2-} ions is expected to be extremely slow, because it requires the concerted creation of both lower *and* higher coordinate $MoO_n^{(6-2n)-}$ ions as presumably short-lived defects or intermediate states. The low coordinate environment, in particular, is likely to be associated with a very high energy of formation resulting in a high activation energy for this process. Vannier et al. have suggested that the long range conductive mechanism for bismuth molybdate involves the vacancies at the isolated, but partially occupied, Bi-O O[19] sites[88]. The O[19] site is in close proximity to Mo(3) and Mo(1) oxygen atoms, and is also strongly bonded to Bi(4) and Bi(5) (Figure 2.1a) with calculated Bi(4)-O[19] and Bi(5)-O[19] bond lengths of 1.97(7) Å and 2.56(3)Å, respectively. These vacant O[19] sites can provide a source of additional oxygen ions/vacancies, so that the conduction mechanism

no longer requires the albeit transient formation of low coordinate $MoO_n^{(6-2n)-}$ ions. This allows a motional process with a lower activation energy to proceed involving the transfer of an O[19] to a nearby vacant O[19] site via an intervening MoO_4^{2-} ion (Figure 2.10). This process is mediated via the extremely rapid rotation of the MoO_4^{2-} ions. Since the closest O[19] sites are along the b- (the column) direction and are 6 Å apart, and only separated by one intervening $Mo(3)O_4^{2-}$ or $Mo(1)O_4^{2-}$ tetrahedral unit, as shown schematically in Figure 2.10, conduction along the b-direction, as proposed by Vannier et al., appears reasonable. Motion in the a-c plane will occur much less frequently, because it involves a jump-process with concerted bond breakages of Mo-O bonds in multiple tetrahedra. For example, O[19] sites are separated by over 9 and 11 Å and two and four MoO_4^{2-} tetrahedra in the c- and a-directions, respectively. Given the low occupancy of the proposed O[19] site, however, it is difficult to determine by NMR the role that this site, or another low occupancy interstitial site in the structure, plays in the process at ambient temperatures. However, the current NMR data clearly indicate that the motion below the phase transition primarily involves motion between the MoO_4^{2-} ions. Above the phase transition, the NMR data indicates that there is an additional mechanism of motion which now involves more of the Bi-O oxygen atoms. These oxygen atoms now appear to serve as possible sites for vacancies (Figure 2.10) and motion is now permitted in three-dimensions.
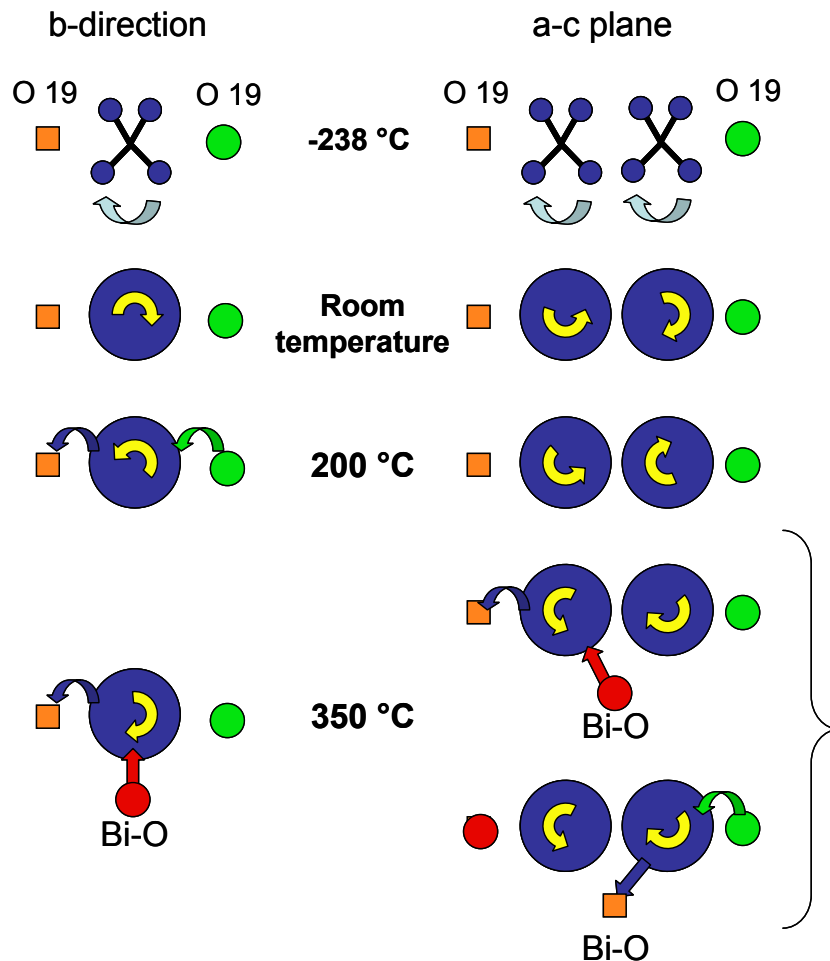
Figure 2.10 Schematic illustrating the dominant motions in $Bi_{26}Mo_{10}O_{69}$ at different temperatures. At low temperatures, rotational motion of the MoO_4^{2-} ions commences, as illustrated by the light green arrow. By room temperature, this motion is so rapid on the scale of any long-range motion, that the tetrahedra may be viewed as rapidly rotating balls on this timescale. By 200°C, concerted motion involving filled and empty O[19] sites and the MoO_4 tetrahedra has commenced. Above the phase transition, additional motion involving oxygen atoms from the Bi-O columns begins; this motion can occur in both the b and a-c directions and does not require concerted Mo-O bond breakage in more than one MoO_4^{2-} tetrahedral unit.

No oxygen vacancy was identified on these column sites in the structural refinements[88,91] performed at room temperature. However, as the temperature is increased, the energy associated with vacancy formation on the Bi-O column will decrease relative to kT (the thermal energy) and formation of oxygen vacancies

appears to be possible. The O-O distances obtained at room temperature[4] between O[5] and O[17], O[5] belonging to the column and O[17] to the nearby Mo(3)O$_4{}^{2-}$ tetrahedron (see Figure 2.1), is 2.82Å, while the O[17] to O[19] distance is only 2.52 Å. Therefore, a hop of the O[19] vacancy to an O[17] site, as described above, can readily occur. Further migration of this vacancy to the nearby O[5] site is then possible, which will result in a three dimensional diffusion process involving both the Bi-O and Mo-O sub-lattices. The observation of residual MoO$_4{}^{2-}$ groups at very high temperatures indicates that not all the MoO$_4{}^{2-}$ groups are involved in rapid exchange. This suggests that while at these temperatures, rapid motion occurs in the a-c plane, as proposed by Galy et al.[89], exchange involving *all* the tetrahedra is not occurring. The motion observed in this system is quite different to that seen by Hampson *et al.* for ZrW$_2$O$_8$.[100] They were able to resolve the individual oxygen sites within the tungstate tetrahedra and observed exchange between all the O-sites at close to ambient temperatures. Although this motion involves two adjacent WO$_4{}^{2-}$ tetrahedra, (the W$_2$O$_8{}^{4-}$ units), again the exchange in this temperature regime involves motion only within the individual tetrahedra, and not between the anions. They proposed a local, re-orientational or "ratcheting"-type motion of the W$_2$O$_8{}^{4-}$ units, based on the exchange rates between the different types of oxygen atoms, which could account for the negative thermal expansion seen for this material. The re-orientational motion seen here in Bi$_{26}$Mo$_{10}$O$_{69}$ is two orders of magnitude faster, which is ascribed to the presence of the large, highly polarizable Bi^{3+} ions with their stereo-active lone pairs. In conclusion, this work has demonstrated that it is

possible to unravel the mechanisms that contribute to both short and long-range conductivity in an extremely structurally and dynamically complex material $Bi_{26}Mo_{10}O_{69}$, by using both short- (NMR) and long-range (*ac impedance*) probes of motion. The NMR analysis required that a large number of different ^{17}O NMR experiments were performed over a wide range of temperatures. We demonstrate that rotational motion of the MoO_4^{2-} units is extremely rapid even at very low temperatures, consistent with the large thermal parameters seen for the O sites of these units[88]. The results indicate that care must be taken when using large thermal parameters as an indication of long-range motion. A new mechanism is proposed to explain the high temperature conductivity of this material that involves oxygen atoms in both the MoO_4^{2-} and Bi-O sub-lattices. The mechanism involves O^{2-} hops between oxygen sites coordinated to Bi^{3+} ions, involving intermediate MoO_4^{2-} tetrahedra. The tetrahedra undergo very rapid re-orientations, mediating the transport process *indirectly:* i.e. the rate limiting process for conduction will be associated with Mo-O bond breakage, rather than MoO_4^{2-} re-orientation, since the latter process is extremely rapid on the timescale of the Mo-O bond breaking process. Although conduction is likely occurring in all three directions, the proposal by Vannier *et al.* that conduction in the b-direction is more rapid than in the a-c plane appears reasonable for 2 reasons, (i) conduction in this direction can occur in the absence of Mo-O, Bi-O column exchange, (via the O[19] sites), without involving concerted Mo-O bond breakage on multiple MoO_4^{2-} tetrahedra and (ii) resonances due to isolated MoO_4^{2-} ions (i.e., O^{2-} in tetrahedra not undergoing rapid exchange with Bi-O ions or between

86

tetrahedra), are seen at very high temperatures suggesting that rapid motion involving all the tetrahedra equally is not occurring.

Chapter 3

Analysis of Structural Characteristics and Dynamics of Lanthanum & Gallium-Doped $Ba_2In_2O_5$ via Ultra-High Field ^{17}O Solid State NMR

Previous high temperature ^{17}O solid-state NMR measurements by Adler et al. show that, in undoped barium indium oxide, an increasing number of oxygen ions are involved in the conductivity between 925 and 1075 °C, i.e., in the tetragonal phase. All oxygen ions are shown to become mobile above 1075 °C as the material enters the cubic phase (Adler et al. J. Am. Chem. Soc., 116 (1994), 675). Current ^{17}O NMR measurements of the undoped $Ba_2In_2O_5$ material at a frequency of 122 MHz showed two resonances at 185 and 137ppm with an intensity ratio of 3:2. The resonance at 185ppm is attributed to O atoms coordinated to 4- and 6- coordinate equatorial In^{3+} groups, while the resonance at 137ppm is attributed to axial oxygens coordinated to two 6-coordinated In^{3+} ions. Material with >20% doping of Lanthanum contained a single resonance at 178ppm consistent with an averaging of all oxygen environments and with XRD analyses showing that these materials display cubic symmetry even at room temperature.

3.1   Introduction

In addition to the bismuth molybdate mentioned in the previous chapter, another class of materials that has been found as a potential lower-temperature competitor for use in oxygen ion conducting applications to yttria-stabilized zirconia (YSZ) and other materials adopting the fluorite structure at high temperatures, are those derived from the perovskite structure. The stoichiometry of this structural family is of the form ABO_3, where "A" are cations, typically rare-earth or alkaline-earth cations and "B" are typically transition metal or semi-metal cations[107] of mixed valency or radius. The B cation coordinates to six oxygens forming corner-sharing octahedra, and the "A" cation occupies the spaces between eight of these octahedral units and coordinating to twelve oxygens.(Figure 3.1) Depending upon the relative sizes of the cations, expansion of the unit cell and significant tilting of the octahedra may occur. Tuning of these distortions may potentially lead to increased conductivity. Perovskites are named for the calcium titanate mineral from which they are derived. In the ideal structure, they have a simple cubic structure having no oxygen vacancies, with space group $Pm\bar{3}m$[116] (Figure 3.1). These materials can be doped with lower valent cations resulting in the introduction of extrinsic vacancies, and often leading to enhanced ionic conductivity.

Within this class of materials, this study focuses on barium indium oxide ($Ba_2In_2O_5$) and its lanthanum (($Ba_{1-x}La_x)_2In_2O_{5+x/2}$) and gallium ($Ba_2(In_{1-x}Ga_x)_2O_5$) doped analogs, as they are materials which have been found to have

conductivites significantly exceeding that of yttria-stabilized zirconia[117] at high temperatures[13,116-124]. The high temperature structure of $Ba_2In_2O_5$ is that of a highly oxygen-deficient perovskite; to charge balance, one sixth of all the oxygen atoms in the perovskite structure are removed, resulting in a structure laden with intrinsic vacancies. In the room temperature phase of barium indium oxide, these vacancies are highly ordered such that the material becomes orthorhombic with space group *Ibm2* [125]. In this phase, the material has three crystallographically distinct oxygen sites ordered in alternating layers of tetrahedrally (T,T') and octahedrally (O) coordinated In^{3+} ions, with alternate tetrahedral layers offset from one another in a ···OTOT´··· pattern (Figure 3.2). Specifically, these are labeled with the O(1) site at the equatorial position of the indium octahedra, the O(2) site at the axial site of the indium octahedra, and the O(3) site at the tetrahedral position (Figure 3.2). This is referred to as the Brownmillerite phase, named for the Ca_2FeAlO_5 mineral originally determined to have this structure[125]. Oxygen vacancies in materials having the Brownmillerite structure order alternately in the (010) planes of the tetrahedral layers. From the orthorhombic room temperature phase, $Ba_2In_2O_5$ undergoes a structural phase change to tetragonal above 925 °C and then to the aformentioned disordered cubic phase above 1075 °C[126]. Information on the conductivity of $Ba_2In_2O_5$ was first determined by Goodenough et al. in 1990 as shown in Figure 3.3[117]. While the large number of oxygen vacancies in the tetrahedral layers would appear to be condusive to good oxygen conduction, trapping of the vacancies in the room temperature orthorhombic phase allows for only limited oxygen motion. As the

material enters the cubic phase at high temperature and the vacancy distribution becomes disordered, conduction is increased by several orders of magnitude. Islam et al. have speculated that this occurs as the temperature is increased and oxygens in O(1) and O(2) environments migrate into the vacancies in the tetrahedral layers until the average coordination environments of the tetrahedrally and octahedrally coordinated indiums become indistinguishable and the material becomes cubic.

Calorimetry measurements by Prasanna and Navrotsky indicate that the experimentally observed disordering of the oxygen vacancies at the cubic transition is only 4.8% of the calculated potential configurational entropy. They interpreted this to mean that conduction is still limited even in this temperature regime by extensive short range ordering[120]. This phenomenon was confirmed by Adler et al. who observed ordering on the range from 50-100 Å in these materials by high resolution transmission electron microscopy (HRTEM)[107]. The current study hopes to more fully examine the implications of this localized ordering using solid state nuclear magnetic resonance (NMR) techniques.

Previous high temperature ^{17}O solid-state NMR measurements by Adler et al. show that an increasing number of oxygen ions are involved in the conductivity between 925 and 1075 °C, i.e., in the tetragonal phase, and that all oxygens become mobile above 1075 °C as the material enters the cubic phase[13]. They observed three ^{17}O resonances in the room temperature spectrum of barium indium oxide, two very broad peaks attributed to the O(1) and O(2) environments, and a narrow peak at 220ppm associated with the O(3)

environment. The peak broadening and lineshapes of the O(1) and O(2) environments are attributed to second order quadrupolar broadening owing to an asymmetric distribution of charge at these oxygen sites (section 1.2.8). They observed a third resonance that was quite narrow and nutated on the order of liquid $H_2{}^{17}O$ (section 1.2.10). This resonance was ascribed to being a crystallographic inversion center having no asymmetric distribution of charge and therefore experiencing no second order quadrupolar effects. The current work re-examines the undoped material using solid state NMR spectroscopy at higher field strengths and 2-dimensional multiple-quantum magic angle spinning (MQMAS) techniques. Also, materials doped with lanthanum at the barium site and gallium at the indium site are examined by solid state NMR for this first time, using both ^{17}O and ^{71}Ga NMR spectroscopy.

3.1.1 Doping Studies

Doping of barium indium oxide by cations into both the "A" (barium) and "B" (indium) sites has been found to stabilize the cubic phase at room temperature. Doping of cations with different valency from those contained in the parent material can reduce vacancy ordering for a number of reasons. First, M^{3+} for Ba^{2+} doping will reduce the concentrations of vacancies. Second, the introduction of dopants with significantly different ionic radii from the end member will cause both local and long range lattice distortions. Substitution of In^{3+} by cations with the same oxidation state such as Ga^{3+} does not change the vacancy

concentration. However, since these materials are synthesized at high temperatures, cation doping is likely to occur randomly in the lattice and may impede the ability of the vacancies to order over long length scales, particularly if the vacancies are strongly correlated, or anti-correlated with the dopant ion. Many studies have suggested that a combination of the reduced vacancy ordering and the distortion of the lattice can facilitate oxygen transport[107,117,127-137]. This study examines both doping strategies: looking at the introduction of lanthanum for barium as a model for the valency difference approach, and gallium for indium to help to understand the size difference strategy.

3.1.1.1 Lanthanum

Forms of $(Ba_{1-x}La_x)_2In_2O_{5+x/2}$ have been found to be cubic at room temperature, though there is some disagreement about the dopant level at which this actually occurs. Some reports have been made that the material is cubic at La dopant levels as low as x = 0.25[133,134], where other studies have indicated that the tetragonal form persists to x=0.5[130,132]. The increased valency of lanthanum (3+) versus that of barium (2+) leads to an overall decrease in the number of vacancies in the system[131] (i.e. an increase in the number of oxygen atoms doped on the vacant sites in the O(3) layers, often referred to as the O3' sites). It is currently thought that the combination of the reduced vacancy concentration and the disorder introduced by La^{3+} prevents cooperative long-range ordering. Experimentally, a linear increase in ionic conductivity in the lower temperature

regime is observed as a function of lanthanum doping up to x=0.6[131]. However, conductivity levels for the high temperature cubic phase of the undoped material are not achieved at lower temperatures. This is believed to be due in part to the overall decrease in the number of vacancies, but the implications on a local level or any short range order are not yet fully understood.

3.1.1.2 Gallium

Though they are isovalent, doping of gallium ions for indium ions has also been shown to stabilize the cubic phase of barium indium oxide at room temperature for x≥0.2[135]. Gallium ions have been found to be randomly distributed in both octahedral and tetrahedral indium layers. However, as they have a preference to be 4-coordinate due to their smaller size, they cause an introduction of oxygen vacancies into the octahedral indium layers and force the material into a disordered cubic form. Previous analysis by extended x-ray absorption fine structure (EXAFS) measurements have indicated that the coordination number of In^{3+} increases with increasing Ga^{3+} content, and thus is was inferred that the coordination number of Ga^{3+} is 4 in these systems[135]. The NMR chemical shift of ^{71}Ga has been previously shown to be very sensitive to coordination environment[138,139], so that this method can be used to determine the local coordination environment of the galliums at a variety of temperatures. In 1999, Massiot and co-workers showed that systems containing 4-coordinate galliums gave rise to ^{71}Ga chemical shifts in the range from 100 - 250ppm, where

those compounds having 6-coordinate galliums were found in the range from -6 - 25 ppm[138]. Finally, LaGaGe$_2$O$_7$, which contains a far rarer 5-coordinate gallium environment was found to have an intermediate [71]Ga shift of 75 ppm[138]. Ash and Grandinetti found similar results upon examination of different gallium-containing systems in 2006[139]. In this way, we are therefore able to use [71]Ga variable temperature solid state NMR spectroscopy to confirm the hypothesis that the barium indium oxide system contains only 4-coordinate galliums. Gallium doped materials have been shown to be less conducting than the undoped material at all temperatures[127,135] which is currently attributed to vacancy trapping near the Ga ion, as well as a decrease in the size of the window formed from 2A & 1B cations through which the O^{2-} has to jump and finally to an overall decrease in total unit cell free volume[135,140]. The overall effect of vacancy confinement is thought to cause conduction limitations as though the long-range structure were of lower symmetry[107].

While the doping of oxide electrolyte materials is clearly a useful way to lower operating conditions to reasonable levels, understanding some of the more subtle localized effects of the process is complicated. In their study on Zr-doped barium indium oxide, Adler et al. found evidence of short range ordering in the form of micro-domain layers over a length scale of 50-500 Å using HRTEM and solid state NMR[141]. They concluded that while the overall cubic symmetry determined by x-ray diffraction should lead to a highly conductive system, actual conductivity is much lower than anticipated due to local vacancy ordering[107]. The formation of microdomains and dopant clustering are also thought to be possible

mechanisms for thermal degradation of the electrolyte[116] over time, this "aging" of the electrolyte rendering it less effective with continued use[117]. HRTEM studies of La and Ga doped barium indium oxide materials performed by Mitome et al.[130] similarly show localized domains. As one of the goals of the current work, we hope to use solid state NMR to confirm whether the case of local ordering holds true for materials doped with lanthanum or gallium. As was mentioned in the previous chapter, solid state NMR is a useful technique for observing localized phenomena in conducting materials as once different ionic species are identified, it is then possible to discern the different conduction pathways associated with each, and hopefully in this case to ascertain whether this motion can be associated with a useful long-range conductive process, or is limited to localized hopping.
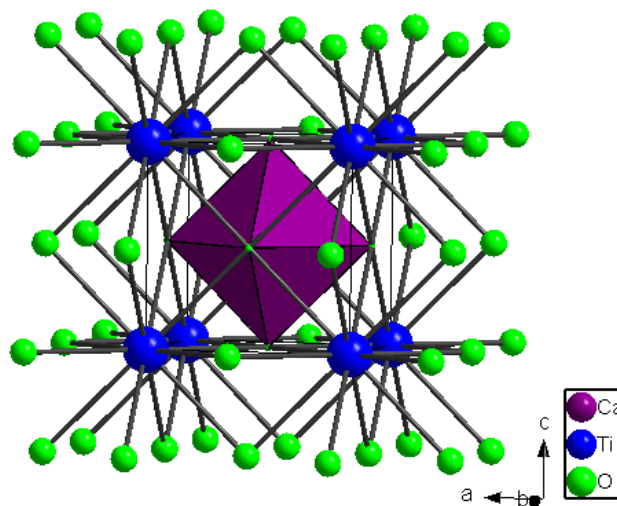
Figure 3.1 Structure of cubic perovskite CaTiO$_3$. Thin lines define the unit cell.
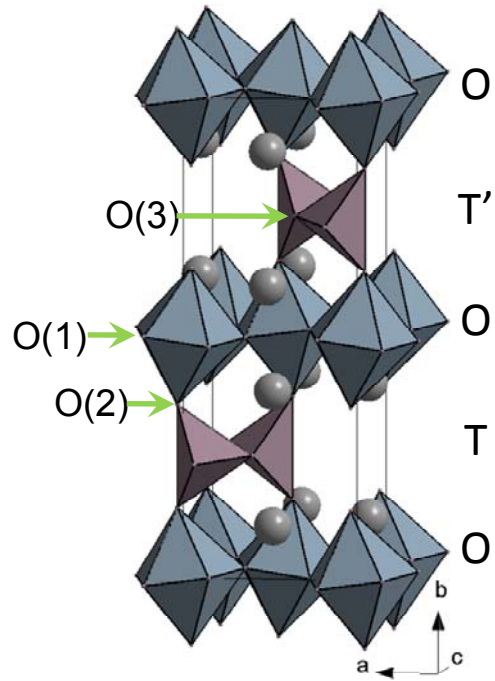
Figure 3.2 Crystal Structure of orthorhombic (room temperature) Brownmillerite $Ba_2In_2O_5$. Gray spheres represent bariums, blue polyhedral represent 6-coordinate indiums and purple polyhedra represent 4-coordinate indiums.
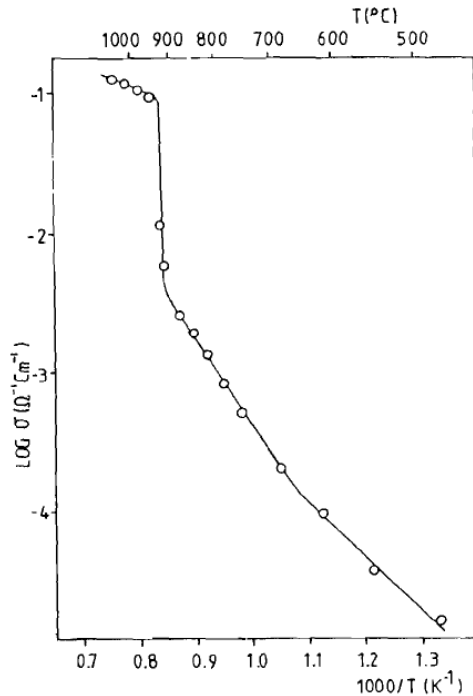
Figure 3.3 Arrhenius plot of lattice conductivity for $Ba_2In_2O_5$ under a $P_{O_2} = 10^{-6}$ atm[*].

3.2   Experimental

Preparation of $(Ba_{1-x}La_x)_2In_2O_{5+x/2}$ compounds for x=0.2 and x=0.4 were performed by K.S. Hong, a student of Dr. Eric Hellstrom at the University of Wisconsin, Madison, by grinding stoichiometric quantities of $BaCO_3$, La_2O_3, and In_2O_3 powders by hand and sintering at 1300°C for 24 hours. Preparation of $Ba_2(In_{1-y}Ga_y)_2O_5$ (y=0, 0.05, 0.1, 0.25, 0.3, 0.45) powders was performed by a solid state route. Stoichometric quantities of $BaCO_3$, In_2O_3, and Ga_2O_3 were ground in a planetary ball mill (Retsch PM100) at 600 rpm for 4 hours. Samples were then pelletized and sintered at 1300 °C for 24 hours and re-ground by hand.

---

[*] Goodenough, J.B., et al. Oxide-ion conduction in $Ba_2In_2O_5$ and $Ba_3In_2MO_8$ (M=Ce,Hf, or Zr) *Solid State Ionics* **44** (1990) 21-31

98

Powder x-ray diffraction spectra of gallium doped compounds were obtained on a Scintag X-ray diffractometer with Cu K_α radiation. ^{17}O enrichment was performed by first drying samples under vacuum at 1000° C for 12 hours, then heating a sealed quartz tube containing a small quantity (~0.5g) of the sample to 1000° C in an $^{17}O_2$ environment (Isotec min. 50 atom %) for 24 hours.

Room and intermediate temperature ^{17}O MAS NMR experiments were carried out at 67.78 MHz (11.7 T) on a Varian InfinityPlus-500 spectrometer equipped with a Chemagnetics 4mm HX probe with pulse widths of 1.5 µs pulse delays of 1-10 seconds depending upon the sample, at a spinning speed of 15 kHz, and using approximately 30,000 scans. Experiments were performed at 8.4 T on a Varian InfinityPlus-360 spectrometer equipped with a Chemagnetics 4mm HX probe with pulse widths of 1.5 s, pulse delays of 1-10 seconds depending upon sample, at a spinning speed of 15 kHz and using approximately 10,000 scans. Finally, experiments were performed at the highest magnetic field strength (19 T) on a Bruker AMX900 spectrometer with a 3.2mm HX probe using pulse widths of 2.0 µs, a pulse delay of 10 seconds, a spinning speed of 20 kHz and approximately 6500 scans. Triple quantum multiple quantum magic angle spinning (MQMAS) experiments were carried out on a Bruker AMX600 spectrometer with a 4mm HFX probe. High temperature experiments were carried out at the National Institute of Chemical Physics and Biophysics in Tallinn, Estonia at 48.8 MHz on a Bruker AMX360 spectrometer equipped with a home-built static 5mm HX probe using pulse widths of 2.5 µs, a pulse delay of 1 second, and approximately 5600 scans. Quadrupole coupling constants were

determined by simulation using Winsolids software. T_1 experiments were performed by varying the pulse delay.

^{71}Ga experiments were carried out at a field strength of 11.7 T on the Varian InfinityPlus-500 spectrometer equipped with a Chemagnetics 4mm HX probe with pulse widths of 1.5 µs, a pulse delay of 0.2 seconds, at a spinning speed of 15 kHz, and using approximately 100,000 scans. Most experiments were performed with a rotor synchronized Hahn-echo pulse sequence $(\pi/6-\tau-\pi/3-\tau)$ to avoid probe ringing.

3.3   Results

3.3.1   Powder X-ray Diffraction

X-ray powder diffraction patterns of lanthanum doped barium indium oxide samples $(Ba_{1-x}La_x)_2In_2O_{5+x/2}$ prepared by K.S. Hong were indexed by him to a tetragonal unit cell for x=0.2 and to a cubic unit cell for x=0.4.

X-ray powder diffraction results of undoped barium indium oxide $(Ba_2In_2O_5)$ prepared at SUNY Stony Brook are consistent with previous reports for this material and show that the structure is orthorhombic (Figure 3.4). Previous studies by Yao et al. indicated that their gallium doped barium indium oxide samples with compositions x=0.2 to x=0.5 can be indexed to a cubic lattice and be quite crystalline with few impurities[135]. These samples were sintered multiple times at 1200°C for 10 hour increments until no changes were observed in the diffraction patterns. The broad peaks observed in the x-ray powder diffraction patterns of the gallium doped samples in the current study (see Figure

3.4) indicate that these samples are less crystalline than those synthesized previously. The major reflections from the XRD pattern of the sample with x=0.25 can be indexed to a cubic unit cell, however, even in this sample there are few unindexed reflections which are ascribed to trace tetragonal or orthorhombic components. The x=0.1 sample is dominated by the tetragonal phase, while the x=0.05 is poorly crystalline and, appears to contain both the orthorhombic and tetragonal phases. These are ascribed to trace tetragonal or orthorhombic Ga-doped $Ba_2In_2O_5$ phases. All other sample compositions appear to have retained even larger regions of orthorhombic and/or tetragonal symmetry. The samples in the current study were only sintered once at 1300°C for 24 hours due to concerns about volatilization of gallium. It can be seen in the diffraction patterns for these samples that a large number of impurities remain, particularly for the x=0.45 sample. An attempt was made to ascertain if these peaks correspond with known barium indium oxide and gallium oxide impurities by comparison with the JCPDS database, but no positive matches were found. It is therefore possible that the extra peaks in this spectrum may be due to additional indium/gallium ordering in the structure, though it is unclear as to what this would look like. Fisher et al. similarly sintered their gallium doped barium indium oxide samples at 1350°C in air for 15 hours, noting that their material also was poorly sintered[129]. They attribute this to the small size of gallium not allowing it to be accommodated into the lattice at higher doping levels. These current authors also note that barium indium oxide and its doped analogs have been previously found to readily absorb water into the crystal lattice even under ambient

conditions and that this may be an additional source for the complexity in the diffraction pattern of these materials.
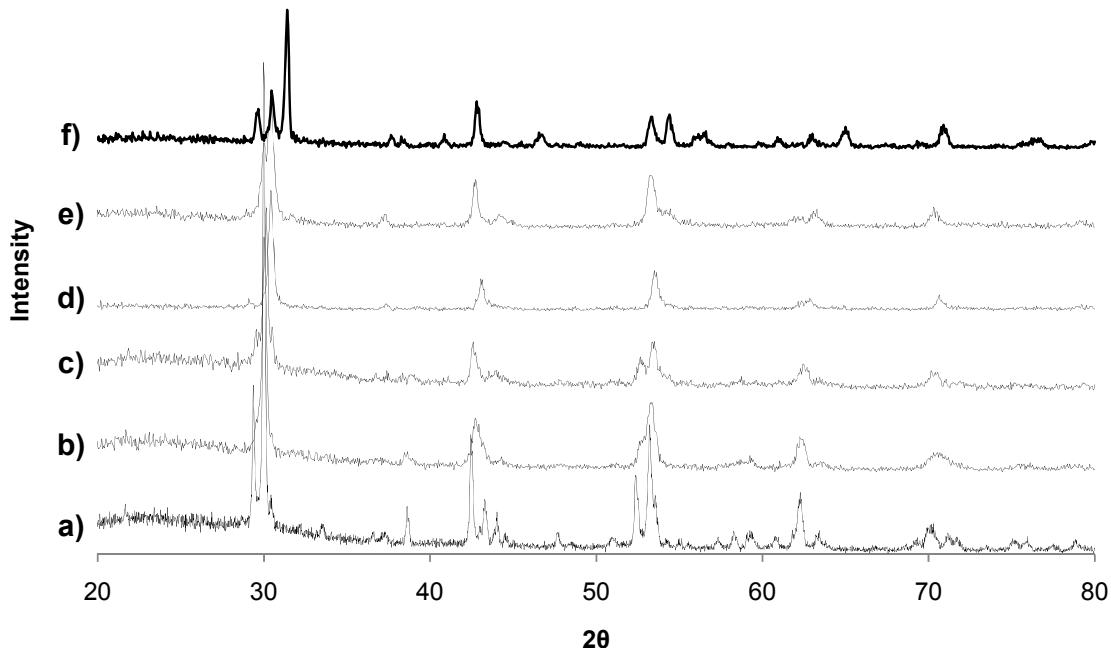
Figure 3.4 Powder X-ray diffraction of gallium-doped barium indium oxide $Ba_2(In_{1-x}Ga_x)_2O_5$ samples with (a) x=0, (b) x=0.05, (c) c=0.1, (d) x=0.25, (e) x=0.3, (f) x=0.45.

3.3.2 ^{17}O NMR of Undoped $Ba_2In_2O_5$

The one-dimensional ^{17}O NMR spectrum of the undoped $Ba_2In_2O_5$ material at 122 MHz (900 MHz rel ^1H) clearly shows two resolved resonances at 184 and 137ppm in an intensity ratio of 3:2 (Figure 3.5). Simulations of the one dimensional MAS spectrum using Bruker X-WinNMR software yield a quadrupole coupling constant (Qcc) value of 5.19 MHz for the oxygen environment producing the 184ppm shift, and a slightly larger value of 5.89 MHz for the environment

producing 137ppm shift. Previously, it has been ascertained that chemical shift differences in ^{17}O NMR spectra of metal oxides can be attributed to differences in the M-O-M bond angle[142,143]. In $Ba_2In_2O_5$, the O(3) site has a significantly different In-O-In bond angle than the O(1) and O(2) environments. This and the fact that its proximity to the intrinsic vacancies gives it a higher probability of having larger quadrupole coupling, and the fact that oxygens attached to lower coordinate metal ions are most often found at lower chemical shifts would imply that this site gives rise to the resonance at 137ppm. However, the resonances exist in a ratio of 3:2 (see Figure 3.5) and the oxygen environments in the matrix exist in crystallographic O(1): O(2) : O(3) ratios of 2:2:1. Given this, the more intense resonance at 184ppm must be due to either the O(1) or the O(2) environment in combination with the O(3) environment. The resonance at 184ppm is attributed to O atoms in O(3) and O(2) environments, while the resonance at 137ppm is attributed to the O(1) environment (see Figure 3.2)). This assignment is made based on the connectivity of the O(2) environment. The O(2) is attached to 4- and 6- coordinate indiums, making it more similar to the O(3) environment than the O(1) environment of only 6-coordinate indiums. The spectra of the undoped samples at various field strengths are shown in Figure 3.6. Significant narrowing of the resonances occurs as the field strength is increased from 48.8 to 122 MHz, indicative of the presence of second order quadrupolar broadening. This is not surprising as the highly vacancy-laden nature of this material should cause the In-O-In environment to be highly asymmetric with large electric field gradients. The broad lines are also an

indication that there is little oxygen motion to average out anisotropic effects (i.e. CSA and quadrupolar) at room temperature.

In an effort to try to resolve any additional ^{17}O sites in undoped barium indium oxide, ^{17}O MQMAS experiments as described above in section 1.2.9 were performed. In the spectrum of the undoped sample at a field strength of 81 MHz, there are still only 2 sites visible, one at 142ppm with Q_{cc} = 5.89 MHz and μ = 0.2 weighted at 33% of total intensity and one at 183ppm with Q_{cc} = 5.19 MHz and μ = 0.3 weighted at 67% (see Figure 3.7). The lower frequency resonance shows a slight broadening along the direction attributed to a distribution of chemical shifts, suggesting that the weaker O(3) resonance may be buried under the more intense O(2) resonance and that it has a slightly different chemical shift. This is consistent with the simulation of the one pulse data, where the fit obtained by using a single set of parameters was not particularly good.

^{17}O NMR spectra of the undoped material dried for 12 hours at 1000°C in the current study did not contain the resonance at 220ppm observed in an MAS spectrum by Adler et al.[13] The spectrum of a sample heated for two hours at 200°C before enriching in a sealed tube at 1000°C for 12 hours, however, contained an intense, sharp resonance at this chemical shift (Figure 3.8). This shift cannot be ascribed to a barium oxide impurity. While the spectrum of barium oxide shows a similarly sharp resonance due to cubic symmetry, the chemical shift of this material at 629ppm[144] is much too dissimilar. Subsequent examination of the literature of barium indium oxide revealed that it readily takes on atmospheric moisture below 300°C. It is therefore the opinion of the author

that the peak observed by Adler et al. at 220ppm in their MAS spectrum is not in fact due to the O(3) site, but to water having entered the lattice as this material is highly subject to hydration even under atmospheric conditions. It is also the opinion of the current authors that the observation that this peak is extremely narrow because the O(3) site is a "crystallographic inversion center" experiencing no second order quadrupole broadening is unlikely as the proximity of the In-O-In site to the highly vacancy laden portions of the material would cause this site to experience significant electric field gradients. Also, even were the O(3) environment an inversion center, this alone would not be enough to remove the second order quadrupolar interactions. It is far more likely that if this peak originates from moisture contained within the lattice, that this water is highly mobile and that this site experiences little second order quadrupolar effect due to motional narrowing as opposed to symmetry.

Adler et al. themselves in fact make this observation in their high temperature spectra wherein they observe coalescence of all oxygen sites above the phase transition temperature as the material becomes cubic, but that the spectrum is not significantly narrowed until it experiences rapid exchanges between all three oxygen sites. It can also be noted in Figure 3.8 that there is only a single broad resonance in addition to the narrowed water peak at 164ppm, intermediate between the original sites observed for the dry material. This is consistent with previous diffraction and simulation results for the hydrated material which indicate that barium indium oxide experiences an averaging of oxygen environments upon hydration[118,145]. Finally, it is likely that the shoulder at

higher frequency (110-90ppm) and the sharper resonances at approximately 225ppm seen in the spectrum of the nominally dry materials acquired at 19 T are due to residual moisture introduced while handling the sample in air.
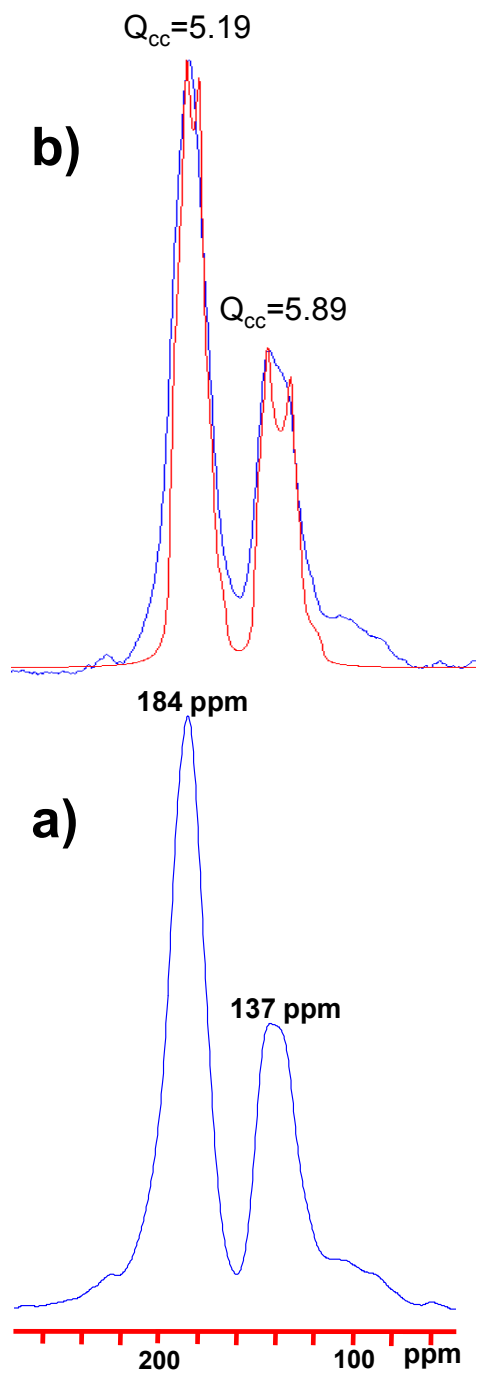
Figure 3.5 (a) Room Temperature 1pulse ^{17}O NMR of $Ba_2In_2O_5$ sample heated at 1000 °C for 12 hours before enrichment, at a field strength of 122 MHz with a spinning speed of 20 kHz, (b) simulations of spectrum using Bruker X-WinNMR software.
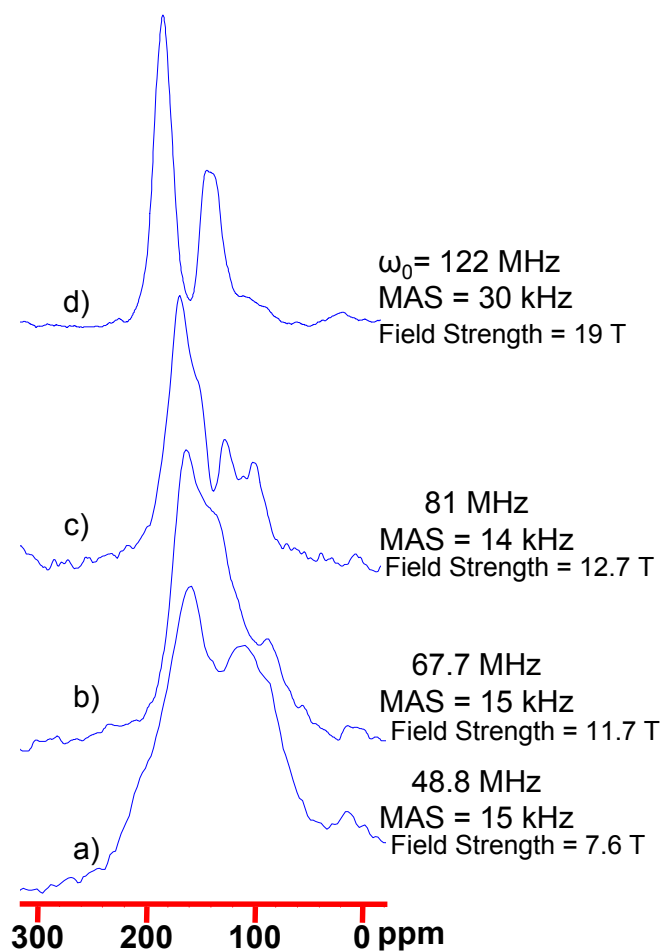
Figure 3.6 Room Temperature ^{17}O NMR spectra of $Ba_2In_2O_5$ at various field strengths and spinning speeds (a) 48.8 MHz spinning at 15 kHz, (b) 67.7 MHz spinning at 15 kHz, (c) 81 MHz spinning at 14 kHz, and (d) 122 MHz spinning at 30 kHz.
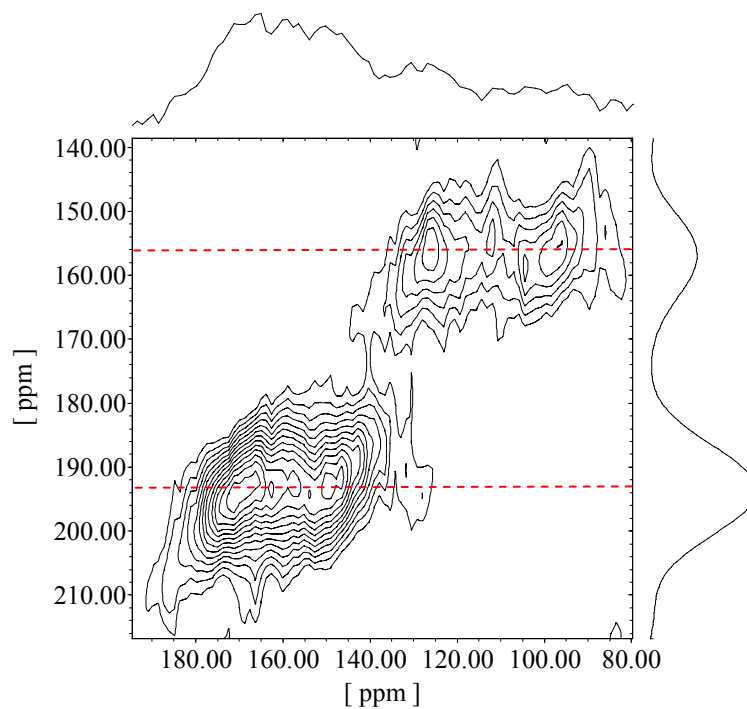
Figure 3.7 MQMAS (3Q) with projections of $Ba_2In_2O_5$ (undoped) at a field strength of 81 MHz (600 MHz rel. [1]H) and a spinning speed of 14 kHz. Dashed lines mark the locations of the isotropic resonances.
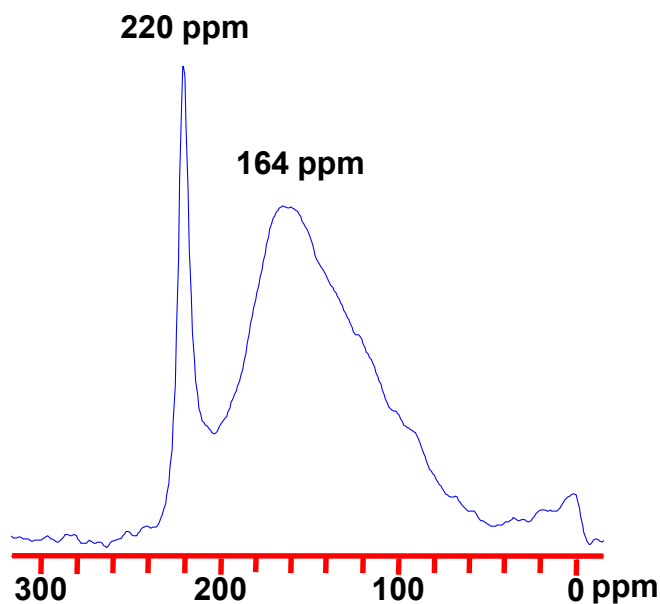
Figure 3.8 Room temperature echo ^{17}O NMR spectrum of $Ba_2In_2O_5$ heated at 200 °C for 2 hours before enriching. The spectrum was acquired at a field strength of 67.7 MHz, (500 MHz rel. [1]H) with a spinning speed of 15 kHz.

3.3.3 ^{17}O NMR of La and Ga Doped Ba$_2$In$_2$O$_5$

The ^{17}O spectrum of lanthanum doped barium indium oxide ((Ba$_{1-x}$La$_x$)$_2$In$_2$O$_{5+x/2}$ with x=0.4 contains a single resonance at 178ppm consistent with an averaging of all oxygen environments and with XRD analyses that this material displays cubic symmetry even at room temperature (Figure 3.9 (c)). The spectrum with x=0.2 also contains a single peak, however, this peak appears to contain underlying features (Figure 3.9 (b)). This may be consistent with diffraction data demonstrating that this material is tetragonal at room temperature, but may instead be indicative that at this dopant level there are still localized ordered domains of the orthorhombic form, as proposed by Mitome et al. based on HRTEM studies[130]. In the MQMAS spectra, the lanthanum doped analogs demonstrate a large distribution along the chemical shift dimension, with far less spreading in the direction of the second order quadrupole broadening as was similarly observed by Adler et al. in their comparison of the magic angle spinning versus dynamic angle spinning spectra of Zr-doped barium indium oxide samples[107]. The spread in chemical shifts further evidences the presence of localized ordering for doped systems (Figures 3.10 & 3.11). This is in contrast to the XRD studies, where cubic symmetry was observed, which implies only one *average* local environment for O. In the isotropic dimension of the x=0.2 sample, shoulders are visible at the same shift position to those observed in the undoped material. This provides strong evidence for the presence of micro-domains in this

110

sample. The pronounced shift to higher frequencies is ascribed to oxygen environments near to La^{3+} ions. Increased La^{3+} doping reduces the number of vacancies, and thus, tetrahedrally coordinated In^{3+} ions. The concentration of environments similar to those of the O(2) and O(3) sites decreases, and more O(1)-like environments are seen. This suggests that the resonance at 137ppm is actually due to the O(2) site, since this environment decreases on La^{3+} doping. This contradicts our assignment of the resonances given earlier. Alternatively, the overall shift to lower frequencies can be ascribed to the presence of La^{3+} instead of Ba^{2+} in the oxygen 1st cation coordination shell.
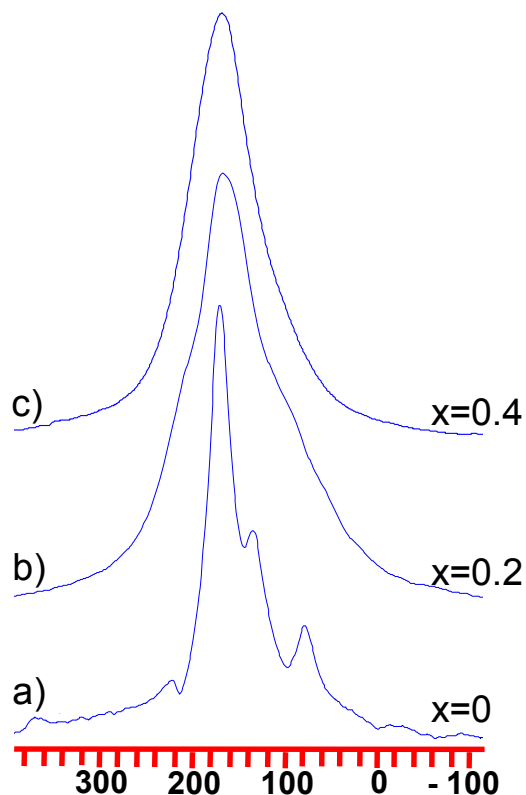
Figure 3.9 Room temperature ^{17}O NMR of $(Ba_{1-x}La_x)_2In_2O_{5+x/2}$ at a field strength of 67.7 MHz, (500 MHz rel. ^{1}H) with a spinning speed of 15 kHz.
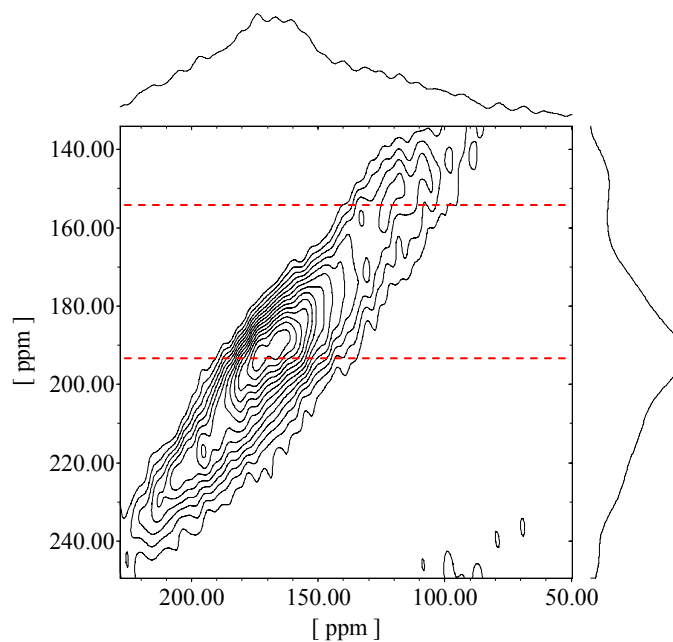
Figure 3.10 Room temperature MQMAS (3Q) spectrum with projections of $(Ba_{0.8}La_{0.2})_2In_2O_{5.1}$ at a field strength of 81 MHz (600 MHz rel. 1H) at a spinning speed of 14 kHz. Dashed lines show the location of the isotropic resonances in the undoped sample.
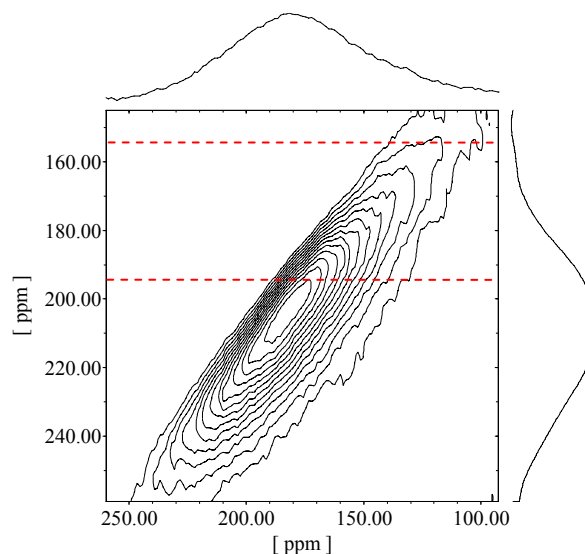
Figure 3.11 Room temperature MQMAS (3Q) spectrum with projections of $(Ba_{0.6}La_{0.4})_2In_2O_{5.2}$ at a field strength of 81 MHz (600 MHz rel. 1H) at a spinning speed of 14 kHz. Dashed lines show the location of the isotropic resonances in the undoped sample.

The ^{17}O spectra of the gallium doped samples $(Ba_2(In_{1-x}Ga_x)_2O_5)$ are quite different from their lanthanum counterparts. Two resonances are observed for all formulations, suggesting that, unlike the lanthanum samples where all oxygen sites become equivalent for x>0.2, the gallium doped samples have localized domains that persist regardless of gallium content (see Figure 3.12). The sharp peak at 220ppm in the one dimensional spectra is at the same location as the hydration peak observed in the end member and is therefore also attributed to some lattice moisture in the doped material. While previous long range measurements from the diffraction of both the gallium and the lanthanum doped samples show that the material becomes cubic at high enough doping levels, clearly the doping strategy of having isovalent cations of a significantly smaller size than in the parent structure i.e. gallium, produces a significantly different local result than the doping of cations with a different oxidation state than in the

parent structure, i.e. lanthanum. The NMR data of these samples is also consistent with HRTEM results by Mitome et al. which show that there are orthorhombic micro-domains that persist for dopant levels up to x=0.5 for gallium doped barium indium oxide, but that for lanthanum doped systems there is evidence of a tetragonal phase to x=0.2, but that above this, the material is cubic even on a local level. In the gallium doped system these micro-domains become too small to be observed by diffraction for x≥0.3, but are believed to be the cause for observations that the conductivity levels for the gallium doped systems are significantly less than those of the lanthanum doped system. In the MQMAS spectra of the gallium doped samples, the two sites persist and the spreading in the quadrupolar direction and the chemical shift direction are nearly equal. The peak at 140ppm seen clearly in the MQMAS spectrum of the x=0.45 sample, and to some extent at lower dopant levels may be due to impurities in this sample as seen in the diffraction pattern (Figures 3.13 - 3.15). As mentioned above, this could also be indicative of indium/gallium ordering, but further XRD and NMR experiments are required to confirm this hypothesis.
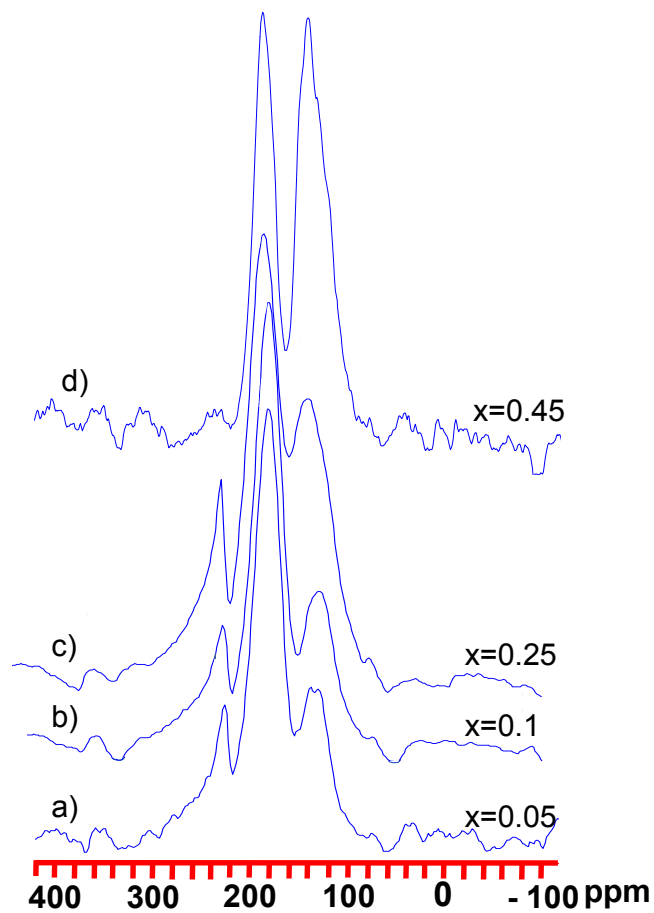
Figure 3.12 Room temperature ^{17}O NMR of $Ba_2(In_{1-x}Ga_x)_2O_5$ at a field strength of 101.5 MHz, (750 MHz rel. ^1H) with a spinning speed of 15 kHz.
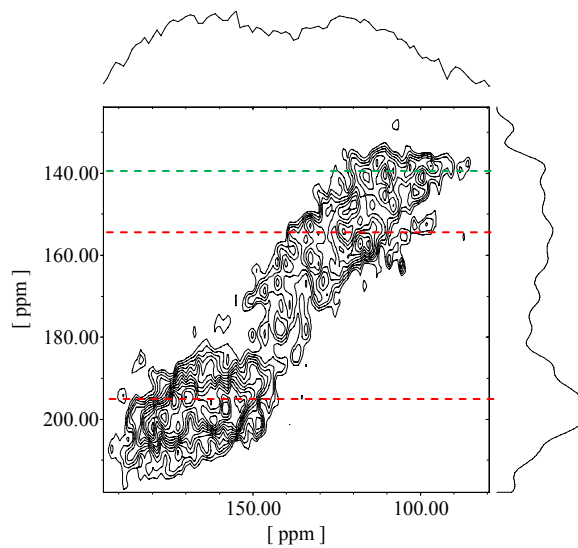
Figure 3.13 ^{17}O MQMAS NMR spectrum of $Ba_2(In_{0.9}Ga_{0.1})_2O_5$ with projections at a field strength of 81 MHz (600 MHz rel. ^1H) at a spinning speed of 14 kHz. Red dashed lines show the location of the isotropic resonances in the undoped sample. Green dashed line shows the location of a third site (see text).
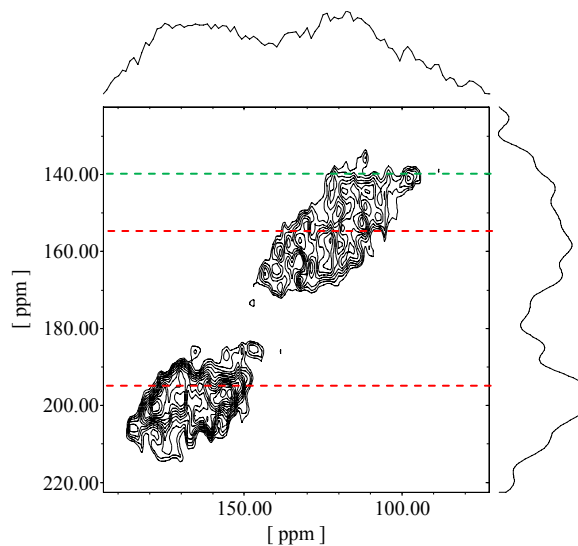
Figure 3.14 ^{17}O MQMAS NMR spectrum of $Ba_2(In_{0.7}Ga_{0.3})_2O_5$ with projections at a field strength of 81 MHz (600 MHz rel. ^{1}H) at a spinning speed of 14 kHz. Red dashed lines show the location of the isotropic resonances in the undoped sample. Green dashed line shows the location of location of a third site (see text).
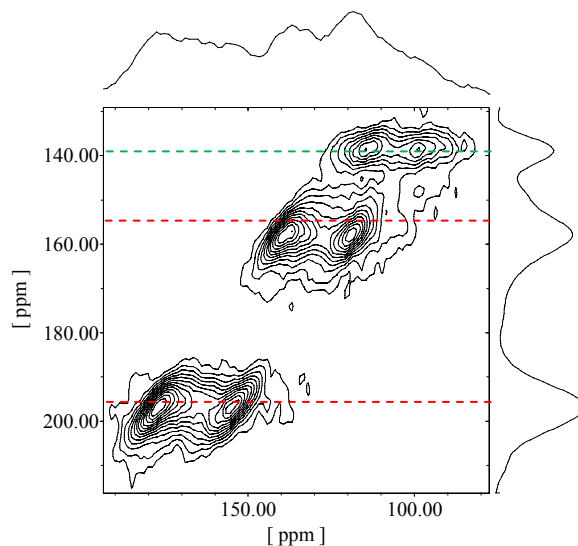
Figure 3.15 ^{17}O MQMAS NMR spectrum of $Ba_2(In_{0.55}Ga_{0.45})_2O_5$ with projections at a field strength of 81 MHz (600 MHz rel. ^{1}H) at a spinning speed of 14 kHz. Red dashed lines show the location of the isotropic resonances in the undoped sample. Green dashed line shows the location of location of a third site (see text).

117

3.3.4   Variable High Temperature ^{17}O NMR

Only at high temperature is an averaging of all oxygen sites in the gallium doped systems observed (see Figures 3.16 and 3.17). Coalescence occurs when the frequency of hops between the two sites ($1/\tau_c$) is greater or equal to $2^{-\frac{1}{2}}\pi\nu_{AB}$, where ν_{AB} is the frequency separation between the two resonances. The frequency difference between the two sites is 4.8 kHz, meaning that at high temperature, oxygens must be exchanging faster than 3.8 kHz. For the x=0.3 system, site coalescence is observed at 400°C, where for the x=0.1 system, coalescence of all of the oxygen resonances is not observed until 800°C. It is not completely clear as to whether this averaging is due to further disordering of the oxygen vacancies and a loss of the micro-domains, or to motional averaging on the spectral timescale. The loss of micro-domains at lower temperatures for higher dopant levels would be consistent with previous HRTEM results as the smaller micro-domains existing in systems with higher Ga content will presumably be averaged out to an overall disordered cubic structure at lower temperatures.
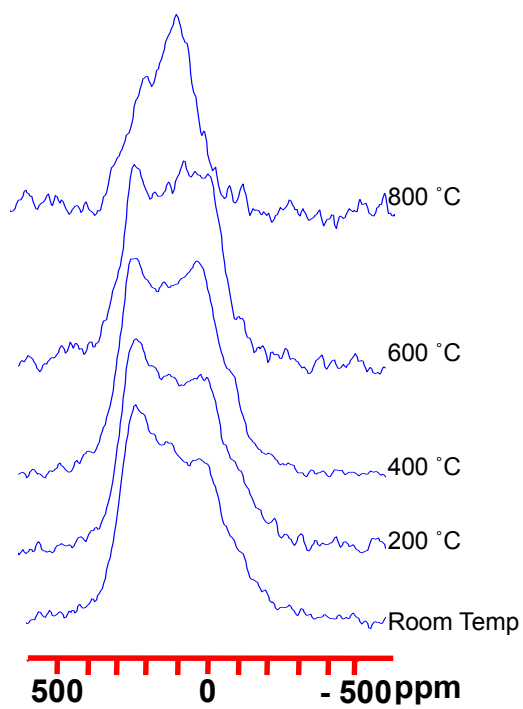
Figure 3.16 Variable temperature ^{17}O static NMR spectra of $Ba_2(In_{0.9}Ga_{0.1})_2O_5$ at a field strength of 48.8 MHz.
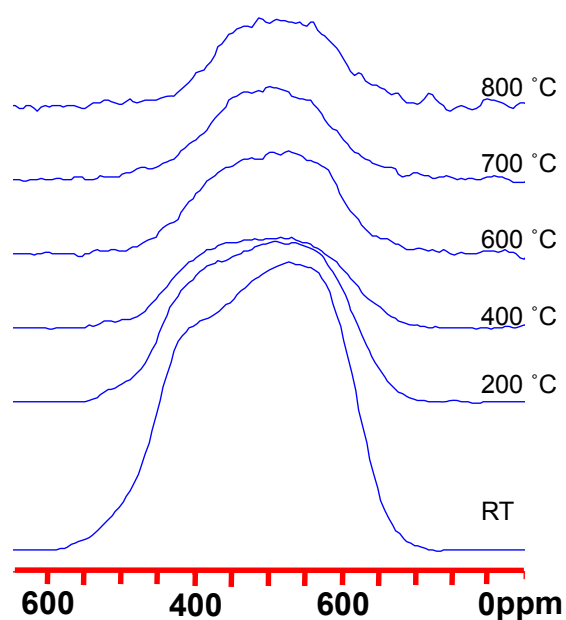
Figure 3.17 Variable temperature ^{17}O static NMR spectra of $Ba_2(In_{0.7}Ga_{0.3})_2O_5$ at a field strength of 48.8 MHz.

3.3.5 Relaxation

To probe oxygen hopping on a faster timescale, relaxation rates versus temperature for barium indium oxide samples with varying gallium and lanthanum contents are shown in Figure 3.18. Relaxation values were calculated using a stretched exponential analysis method as described in section 2.2.4. Relaxation rates for lanthanum containing systems were found to be much more rapid than those for gallium containing systems, consistent with conductivity data indicating that lanthanum doping enhances conductivity in barium indium oxide systems, where gallium doping impedes it.

120
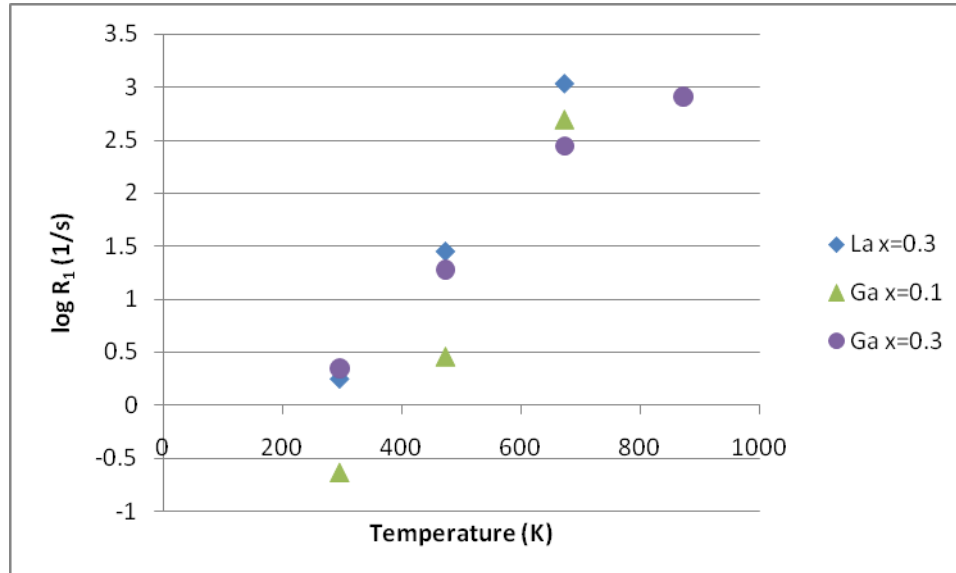
Figure 3.18 Relaxation rates vs. temperature for barium indium oxide samples with various dopant levels of lanthanum or gallium.

3.3.6 One-Dimensional ^{71}Ga NMR

The ^{71}Ga spectra of the x=0.1 and 0.25 samples of gallium doped barium indium oxide $Ba_2(In_{1-x}Ga_x)_2O_5$ show two resonances, an intense peak at 235ppm and a much smaller resonance at 127ppm (Figure 3.19). Both of these resonances are in the chemical shift range for 4-coordinate gallium. This confirms that in fact gallium in the barium indium oxide system prefers to be 4-coordinate due to its small size, but that there are two different 4-coordinate gallium environments. As was noted in the analysis of the diffraction data, it is not clear structurally as to what these two environments would look like.
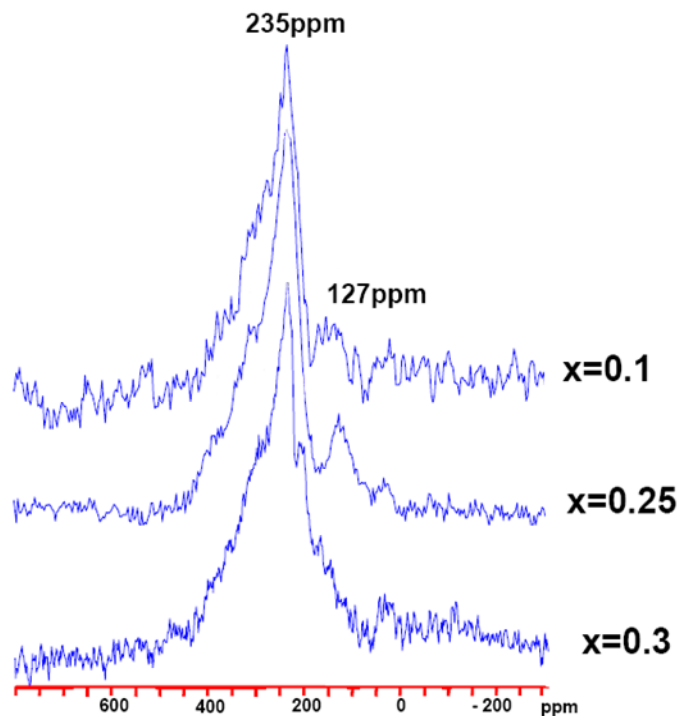
Figure 3.19 ^{71}Ga NMR spectra of Ba$_2$(In$_{1-x}$Ga$_x$)O$_5$ at a field strength of 152 MHz, spinning at 15kHz.

3.4 Discussion

As described in section 2.3.1, using equation [2.4][108], relaxation data can be used to extract correlation times (τ_c = 1/hop frequency) for oxygen motion on a very fast (kHz-MHz) timescale in ionically conducting systems. From the simulations of the 2 sites in the MAS data (Figure 3.5), an average quadrupole coupling constant of 5.6 MHz was used. Figure 3.20 shows correlation times versus T$_1$ data for lanthanum and gallium doped barium indium oxide samples. Hop frequencies derived from these as a function of temperature are compared in Figure 3.21. From these it can clearly be seen that oxygen hopping for x=0.3 lanthanum doped sample is significantly faster than for gallium doped analogs.

122

(Signal to noise of the x=0.1La-doped sample was insufficient to acquire relaxation measurements). The hop frequencies for this system overall is nearly two orders of magnitude less than that observed in the bismuth molybdate examined in Chapter 2. This is not overly surprising given the significantly broader peaks of the barium indium oxide system indicate that there is little localized motion to average peak widths at lower temperatures.
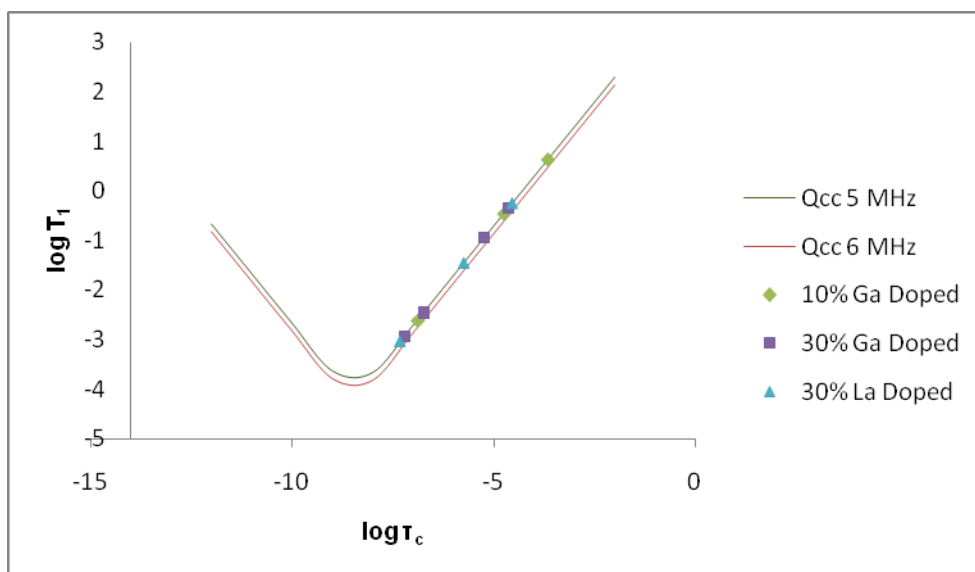
Figure 3.20 High temperature ^{17}O NMR T_1 relaxation times for average oxygen environments in gallium and lanthanum doped barium indium oxide at 8.5 T vs. calculated correlation times with an average quadrupole coupling constant of 5 MHz.
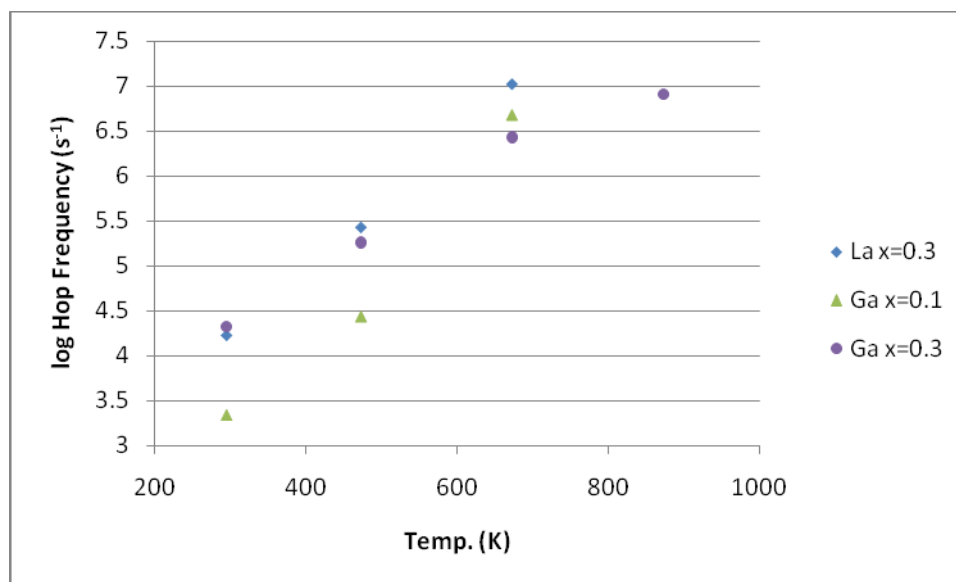
Figure 3.21 Comparison of hop frequencies vs. temperature for lanthanum (($Ba_{1-x}La_x)_2In_2O_{5+x/2}$) and gallium ($Ba_2(In_{1-x}Ga_x)_2O_5$) doped barium indium oxide samples.

3.5   Conclusions

Using ^{17}O solid state NMR we demonstrated that only two resonances exist in dry, undoped barium indium oxide in a ratio of 3:2. The more intense resonance is attributed to a combination of the O(2) and O(3) environments. The sharp resonance at 220ppm previously attributed to the O(3) site is shown to appear only upon hydration of the material and is therefore re-assigned to water in the lattice, though this may be due to a decomposition reaction which would need to be further explored. It has also been shown that significant differences between lanthanum and gallium doped samples exist on a local level. For lanthanum doped systems, material with x=0.4 is shown to have a single, symmetric resonance consistent with diffraction data indicating that this material

is cubic. The material with x=0.2 showed features indicative of the persistence of a lower symmetry structure, also consistent with diffraction data showing that this material is tetragonal. Spectra of the gallium doped compounds show two persistent resonances regardless of the doping level. This is inconsistent with long range measurements from powder diffraction indicating that the material becomes cubic at high enough doping levels, but confirms the presence of micro-domains as seen previously by HRTEM. Little oxygen motion is observed at room temperature for any of these systems, and even at high temperature is demonstrated to be an order of magnitude slower than that of the bismuth molybdate examined in the previous chapter.

Chapter 4

Proton Conduction and Hydration Dynamics in $Ba_2In_2O_5 \cdot H_2O$

Barium Indium Oxide and its doped analogs have been found to readily take on water below 300°C where they are then able to act as intermediate temperature proton-conducting materials. In the case of undoped samples, a hydrated tetragonal phase $Ba_2In_2O_5 \cdot H_2O$ is formed[145]. Variable temperature ^1H NMR data of the end member of this system shows that it possibly forms impurities during the hydration process. In addition, two-dimensional exchange (EXSY) data shows that the pathway for proton migration in these systems involves full exchange between all sites, at least on a slow timescale.

4.1   Introduction

Uptake of protons in humid atmospheres by vacancy-containing oxide ceramics has been documented since the 1950's when it was first reported in ZnO[146,147]. This was initially thought to be problematic for applications involving oxide ion conduction as the formation of hydroxide defects is a competitive process to that of oxide conduction (i.e. protons are incorporated into the matrix at the expense of oxygen vacancies)[148]. In other materials, however, protons hopping has been determined to have many uses in lower temperature applications requiring ionic conduction such as humidity and hydrogen sensors[149]. It was originally thought that proton conduction could not have uses in solid oxide fuel cell (SOFC) electrolyte materials because of the requirement for high operating temperatures when coupling with the steam reforming process. Materials such as hydroxides, hydrates and acid salts were found to have high protonic conductivity, but are unstable at high temperatures[148,149]. Because it has been found that some perovskite-based materials retain large quantities of water even in a moderately high temperature (500-800°C) range, these materials would seem to make high temperature proton conduction for intermediate temperature solid oxide fuel cell (IT-SOFC) applications a possibility[8,150-153]. Systems most appropriate for these applications retain their structure even upon continued hydration and dehydration in reducing and oxidizing atmospheres. Often they function as proton conductors at intermediate temperatures where the ratio of protonic defects dominates and as oxide conductors at high temperature once

the number of oxygen vacancies and their mobility is high enough to facilitate this process. This being said, Norby and co-workers have observed that controlling the protonation process is complicated as most oxide conductors that take on water exist most readily in an intermediate state between being anhydrous and being completely saturated with moisture[148,152]. They note that these materials take on noticeable quantities of water even at ambient conditions, while *complete* hydration is often complicated by the evaporation of lattice-trapped moisture and competition with oxygen conduction at high temperatures, and the ordering and low mobility of oxygen vacancies at low temperatures. This means that the low temperatures required to prevent dehydration often make for impractically long equilibration times[152] to meet the conditions to insert the theoretical maximum amount of water. It has also been noted in a review article on protonic conductors by Kreuer that the ability to hold moisture is often strongly in opposition to the stability of the material. They observe that in those perovskites strongly deviating from perfectly cubic symmetry and having multiple oxygen sites, the proton saturation limit is greatly reduced[8]. But, while distortions decrease the total amount of water that can be inserted into the matrix, they are able to stabilize both the overall structure, and any defects which *are* induced, making it somewhat difficult to ascertain structurally what would compose the ideal protonic conductor. Empirically this has been shown for the cases of $BaCeO_3$ and $SrCeO_3$, where the barium containing system has a far larger distortion toward the orthorhombic form. This symmetry reduction stabilizes the introduction of protons into the matrix[8]. It has also been found that low hydration

entropy can stabilize protonic defects even in systems with relatively unfavorable hydration enthalpies. The result of this is that the hydration enthalpy alone will not necessarily be indicative of the temperature of dehydration for hydrated perovskites. This was demonstrated for yttria doped barium zirconate where the dehydration temperature is surprisingly high, even given a relatively low enthalpy of hydration[154]. This series of complicating factors merits a thorough examination of the mechanisms both for the insertion of water into these systems, and for its transport once systems are hydrated.

The formation of protonic defects in perovskite-type oxide solids happens via the process of water vapor reacting with oxygen vacancies. In Kröger-Vink notation[155] this is described by:

$$H_2O_{(g)} + V_O^{\bullet\bullet} + O_O^x \leftrightarrow 2(OH)_O^{\bullet}$$
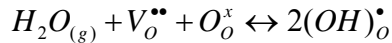
[4.1][118,149]

Where the superscripts $^{\bullet}$ and ^{x} represent positive and neutral effective charges respectively, and the subscript $_o$ denotes the oxygen site, with the formation of two protonic defects for each oxygen vacancy. The mechanism for transport was thought at first to occur via hydroxide ions moving into oxygen vacancies (vehicle mechanism), but has subsequently been determined to be via re-orientation and subsequent hopping of lone protons between oxygens (Grotthuss mechanism)[156]. This is observed by isotope effects observed in impedance measurements[152,157]. Molecular dynamics (MD) simulations have indicated that the activation energy barrier for re-orientation has been found to be lower for

weak hydrogen bonding, where strong hydrogen bonding favors rapid proton transfer[158]. For hydrated perovskites with long (>2.5 Å) O-O separations, proton transfer is exclusively intra-octahedral (see Figure 4.1(a)). In opposition, for those materials having short (<2.5 Å) O-O separations, the proton being transferred is inter-octahedral, being located in a severely bent hydrogen bond outside the BO_6 octahedra because of strong repulsive interactions between the proton and the B cation (Figure 4.1 (b)). The proton transfer mechanisms are then split between being intra- and inter- octahedral in nature. The shortening of the O-O bond allows for stronger hydrogen bonding, facilitating proton transfer, but hinders structural re-orientation. These two competitive processes have been found to have similar activation energy barriers for oxygen-oxygen separations of 2.5-3 Å, so that the overall barrier for proton conduction is similar over a wide range of hydrogen bond strengths[8,154,156,158-162].
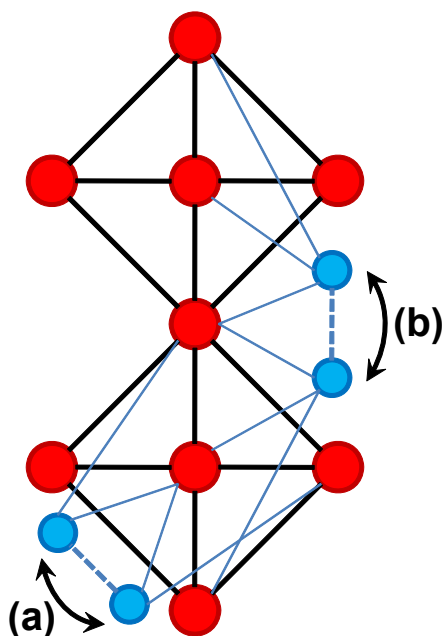
Figure 4.1 Schematic of (a) intra- versus (b) inter proton transfer in hydrated perovskites[154].

The aforementioned barium indium oxide ($Ba_2In_2O_5$) and its doped analogs have been documented to readily take hydrogen into the matrix in humid atmospheres between 200 and 300°C[84,140,145,163-166]. The end member was determined to be a reasonable protonic conductor by Zhang and Smyth in 1995[149], though it has been found that the proton conductivity of the $Ba_2In_2O_5 \cdot H_2O$ is less than 10^{-4} S cm^{-1} at 573 K. Above this temperature, $Ba_2In_2O_5 \cdot H_2O$ decomposes into dry $Ba_2In_2O_5$ and H_2O, and continued hydration and dehydration of this system leads to cracking,[167] rendering it as non-ideal for long term fuel cell applications. Understanding of the moisture uptake and protonic conductive processes in this system, however, is of particular interest as the extremely large number of vacancies in the Brownmillerite structure facilitate

a level of hydration not witnessed in related materials. Simulations by Islam et al.[118,145] have indicated that this may be because, in addition to the incorporation of protonic defects created at intrinsic vacancies (Schottky defects) in the lattice (see Figure 1.2 and Equation [4.1]), accommodation of hydroxyl groups into the free spaces in the tetrahedral layers is also possible. The authors equate movement of oxygens into these highly ordered vacancies in the tetrahedral layers with movement into interstitial sites (Frenkel defects) (Figure 1.2). These defects are formed in the process of disordering as the material is heated as described in section 3.1. Their calculations show that this process is not only possible, but highly energetically favorable. As above, in Kröger-Vink notation[155], this mechanism is described by:

$$H_2O_{(g)} + V_i^x + O_i^{''} \rightarrow 2OH_O^{'}$$
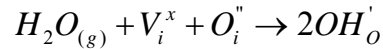
$$[4.2]^{118,145}$$

Where the superscript ' represents an effective negative charge. If water is then thought to be incorporated into the lattice as protons and interstitial oxygens, as suggested by Norby et al.[152], this would then be represented by:

$$H_2O_{(g)} + V_i^x + 2O_O^x \rightarrow 2OH_O^{\bullet} + O_i^{''}$$
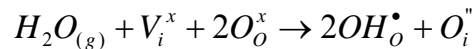
$$[4.3]^{145,152}$$

The incorporation of water into both Schottky and Frenkel types of defects in the $Ba_2In_2O_5$ lattice is then described by:

$$H_2O_{(g)} + V_O^{\bullet\bullet} + O_i^{''} \rightarrow 2(OH)_O^{\bullet} + OH_i^{'}$$
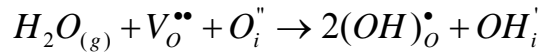
<div align="right">[4.4][118,145]</div>

By simulations, the axial O(1) site of the octahedral units is the most energetically favorable for vacancy (Schottky defect) accommodation (i.e. to bind a proton). The O-O bond lengths in hydrated barium indium oxide were found to be 2.81 and 3.00 Å for the tetrahedral [001] and octahedral [100] directions respectively[168]. As described above, with these long O-O distances, little octahedral tilting is observed and an intra-tetrahedral proton migration pathway is anticipated.

It has been reported that, according to previous thermogravimetric analysis (TGA) studies, up to an equimolar quantity of water in total can be absorbed by the undoped material[165,169]. As was noted above by Norby et al., similar to other conducting oxides, meeting the conditions for complete protonation of the barium indium oxide system is complex and intermediate stages of hydration leading to adjustments in unit cell parameters have been observed[84,169,170]. Jayaraman et al. specifically observe three distinct phases in the undoped system which they refer to as the anhydrous phase, they denote as $Ba_2In_2O_5\square$, the fully hydrated or "proton phase", denoted $Ba_2In_2O_5 \cdot H_2O$, and finally an intermediate "hydrate" phase denoted $Ba_2In_2O_5 \cdot \alpha H_2O$ where $\alpha < 1$. They point out, however, that as each oxygen is already bonded to two In^{3+} atoms, protons must be inserted into the matrix as an $-OH^-$ group entering a vacancy and an H^+ associating with oxygen ions already in the lattice, and not as water

molecules. Previous TGA results on lanthanum doped samples $((Ba_{1-x}La_x)_2In_2O_{5+x/2})$ have indicated that there is a maximum water uptake for x=0.1[164]. Plots of proton conductivity versus La content also indicate that conductivity reaches a maximum for this dopant level. This trend is thought to be because La doping causes an increase in the unit cell free volume, allowing for increased conductivity, but that the concurrent decrease in the number of oxygen vacancies with increased doping levels becomes significant above x=0.2 so as to cause a precipitous drop in protonic conductivity, indicating a close correlation between hydration and conduction levels. Omata et al. observed that for the gallium doped analogs, however, hydration levels were less than that of the end member for all dopant levels, presumably due to the smaller size of this dopant, relative to the indium cation, causing an overall decrease in the unit cell volume.

It has been shown previously by diffraction of the undoped material, that the orthorhombic structure is retained with only slight changes in displacement parameters until the material is sufficiently hydrated wherein it undergoes a change to tetragonal symmetry[169] (Figure 4.2). This occurs when the addition of hydroxides into the matrix causes one half of the indium ions to go from tetrahedral to octahedral coordination and induces a reduction in the unit cell volume by twenty-five percent[169]. This phase was originally refined to space group P4/mmm by Fischer in 1999[169], and then re-assigned to P4/mbm by Jayaraman in 2004[84]. By diffraction methods, protons have been found to order themselves into the barium indium oxide matrix in two locations (Figure 4.2). As mentioned above, one of these sites is formed by hydroxyl groups moving into

the spaces (interstitial sites) formed in the tetrahedral layers, and the other by protons associating with oxygens in the crystal lattice. There is some controversy as to which oxygen these protons are associated with. Molecular dynamics simulations by Fisher et al. have indicated that H^+ ions associate themselves with oxygens on the O(1) site[145], where x-ray diffraction data show that this proton or deuteron is more likely to be attached at the O(2) site[84,171].

While several in depth studies have clearly illustrated the complexities of the structure and long range conductivity of the hydrated form of barium indium oxide using diffraction and impedance measurements respectively[149,165,166,169], none so far have been able to experimentally confirm the localized pathway for proton migration in this system, i.e., whether the protons involved are in fact those found only in the interstitial spaces of the tetrahedral layers as indicated by simulations[118,145,168], or to examine the implications of the complex ordering which occurs upon hydration of this system. We hope to accomplish this via the utilization of variable temperature solid state nuclear magnetic resonance (NMR) measurements. While previous room temperature proton (^{1}H) and deuterium (^{2}D) solid state NMR measurements have identified a total of three discernable hydrogen environments in $Ba_2In_2O_5 \cdot H_2O$[84] present in a 1:1:2 ratio. These are currently unassigned. To address the inconsistency with diffraction results that indicate that there are only two proton environments, the authors have hypothesized that additional ordering of the proton sub lattice occurs. They believe that this results in the actual unit cell being much larger than the average unit cell of the P4/mbm space group used in the refinement, with NMR being

sensitive enough, at least for one of the two environments, to be able to distinguish between variations between different ordering schemes.

The relationship between O-H⋯O bond length, and proton chemical shifts in solid state NMR has been extensively examined[172-177]. Those species having weaker H-bonding producing peaks at lower chemical shift values, while those with shorter bonds producing peaks at higher values. In a linear regression fit of all literature data available to them at the time, Yesinowski et al. have found that this relationship in hydrous mineral species can be described by:

$$\delta_{iso}(ppm) = 79.05 - 0.255d(O - H \cdots O)(pm)$$

[4.5][177]

In these studies, hydrated forms of Brushite ($CaHPO_4 \cdot 2H_2O$), Gypsum ($CaSO_4 \cdot 2H_2O$), Hemimorphite ($Zn_4Si_2O_7(OH)_2 \cdot H_2O$), and α-Oxalic acid dihydrate (α-$(COOH)_2 \cdot H_2O$) give rise to proton chemical shifts for hydrated protons of 6.4, 5.3, 3.6, and 8.2ppm respectively. In the current work, the correlation of equation [4.5] is used to assign the peaks observed in the spectra of the hydrated phases. Using these assignments we hope to be better able to explain the dynamics of the complex proton conduction process in barium indium oxide through the use of more extensive NMR experiments at variable temperatures.

Two-dimensional exchange (EXSY) experiments (section 1.2.2) were carried out at variable temperatures in order to determine the exchange rate of protons hopping on a very slow timescale between that of the order of the

difference between the chemical shifts for the exchanging sites and the relaxation time. Proton exchange experiments have been carried out previously by Goward et al. for imidazole-based proton conductors[178]. These types of proton conducting membranes are composed of proton-conducting units tethered to a polymer backbone, allowing them to function as potential materials in IT-SOFC's. While compositionally these materials are quite different than the oxide ceramics examined in the current study, proton transport similarly occurs via a structural diffusion (i.e. Grotthus) mechanism as described above. We therefore thought it appropriate to similarly measure the proton exchange in hydrated barium indium oxide samples using this technique.
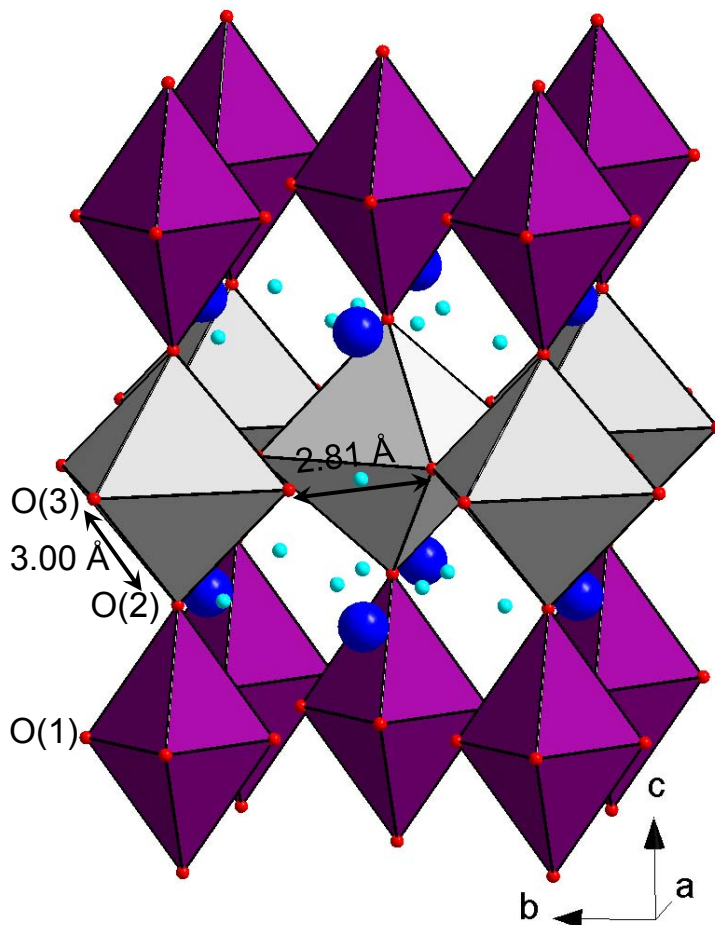
Figure 4.2 Crystal structure of $Ba_2In_2O_5 \cdot H_2O$[171]. Blue spheres represent Ba^{2+} ions, gray tetrahedra represent In^{3+} ions originally in tetrahedral layers of the dry structure, purple tetrahedra represent In^{3+} ions originally in octahedral layers of the dry structure, red spheres represent O^{2-} ions and cyan spheres represent H^+ ions. Symmetry is tetragonal with space group P4/mbm.

4.2   Experimental

The preparation of $(Ba_{1-x}La_x)_2In_2O_{5+x/2}$ (x=0, 0.05, 0.10, 0.20, 0.25, 0.30, 0.45, 0.60), and $Ba_2(In_{1-y}Ga_y)_2O_5$ (y=0, 0.05, 0.1, 0.25, 0.3, 0.45) powders was performed by a solid state route as described in section 3.2. Samples were prepared as described above in section 3.2, but by first heating the sample to

250°C under ambient conditions for 2 hours to hydrate, rather than drying. Samples for ^{1}H NMR were hydrated by placing approximately 0.5 grams into a Pyrex tube affixed to a second tube filled with de-ionized water, heating the sample to 350°C in a test tube furnace while simultaneously heating the water-filled tube to approximately 90°C in a water bath. Various samples were then cooled in different manners. Samples where the furnace was simply turned off, allowing the temperature to quickly drop back to ambient levels are subsequently referred to as "fast hydrated". Samples which were cooled to 250°C at a rate of 1 °C/min and 0.1°C/min and held for 18 hours, then cooled to room temperature are subsequently referred to as slow and ultra-slow cooled respectively.

Powder x-ray diffraction spectra were then obtained for $2\theta = 10\text{-}80°$ on a Scintag X-ray diffractometer with Cu K_{α} radiation. Thermogravimetric analysis (TGA) experiments were carried out on an (TA Instruments Q500) instrument by ramping from room temperature at a rate of 7.7 °C/min to a final temperature of 950°C, and remaining at this temperature for 1 hour.

Room and moderate temperature MAS NMR experiments were carried out at 67.7 MHz (11.7 T) on a Varian InfinityPlus-500 spectrometer equipped with Chemagnetics 4mm HX and HXY probes and also at 48.8 MHz (8.4 T) on a Varian InfinityPlus-360 spectrometer equipped with a Chemagnetics 4mm HX probe with pulse widths of 2.1 μs, pulse delays of 1-10 seconds depending upon sample, at a spinning speed of 15 kHz, and using approximately 1800 scans. Experiments were performed with a rotor-synchronized Hahn-echo pulse sequence $(\pi/2 - \tau - \pi - \tau)$ to avoid probe ringing. Variable temperature two-

dimentional exchange (EXSY) experiments were carried out using the three-pulse sequence as described in section 1.2.2.

4.3   Results

4.3.1   Powder X-ray Diffraction

From comparison of our x-ray diffraction data of undoped $Ba_2In_2O_5 \cdot H_2O$ (Figure 4.3) with that in the literature[165,169], it would appear that we have not achieved complete hydration, even for samples cooled slowly in the temperature regime of maximum water uptake. The rapidly hydrated sample (Figure 4.3 (b)) is clearly still dominated by the orthorhombic phase, but with a reduction in cell parameters evidenced by slight peak broadenings. The slow and ultra-slow hydrated samples would appear to be a mixture of more and less hydrated phases as seen in Figure 4.3 (c) & (d). Characteristic peaks of the fully hydrated tetragonal phase are marked with arrows. Upon re-examination of the literature, it was found that thermogravimetric analyses by Jayaraman et al[84]. under hydrating conditions of barium indium oxide indicated that a steady mass for the sample was attained only after heating for approximately one month. Therefore it is not surprising that, after heating for only 18 hours, that our samples demonstrate characteristics resembling both the anhydrous and hydrated forms of the material.

Results for dry lanthanum doped samples in the current study (($Ba_{1-x}La_x)_2In_2O_{5+x/2}$) (Figure 4.4) for $x \geq 0.2$ would appear to be cubic as previously reported in the literature. Peak splittings are consistent with characteristic Cu-

Kα1/Cu-Kα2 splits from the x-ray source. For x=0.1, (Figure 4.4 (c)) it would appear that some of the orthorhombic phase is still present. The sample where x=0.05 would also appear to be indexed to a cubic unit cell, though the reliability of this sample composition is somewhat questionable. Diffraction patterns for hydrated La-doped show almost no structural changes when compared with spectra for dry samples (Figure 4.5).
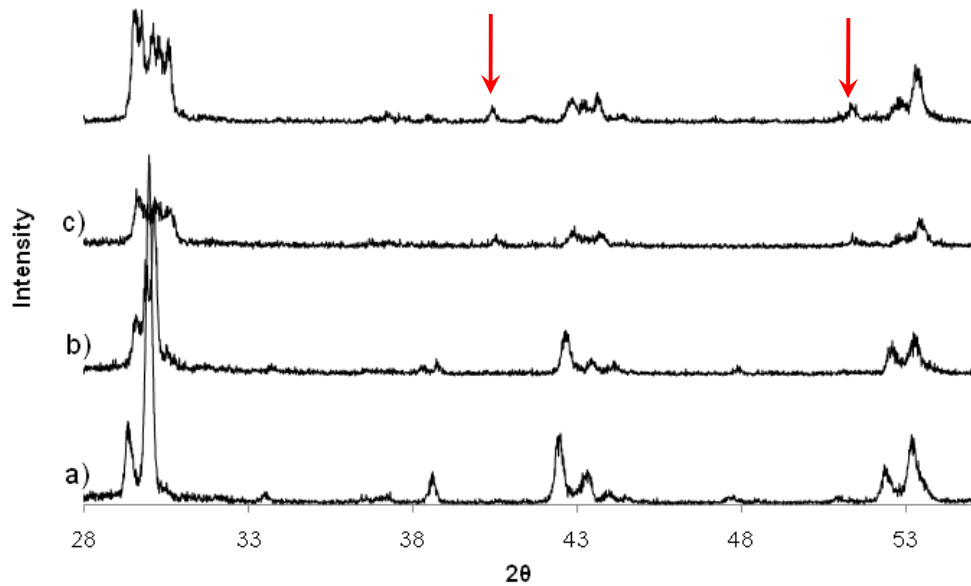
Figure 4.3 Powder x-ray diffraction of hydrated barium indium oxide $Ba_2In_2O_5 \cdot H_2O$ samples (a) dry (b) rapidly hydrated by turning off furnace during cooling (c) cooling at a rate of 1°C/min and (d) cooling at a rate of 0.1°C/min. Arrows show locations of reflections known to be characteristic of the fully hydrated form of the material.
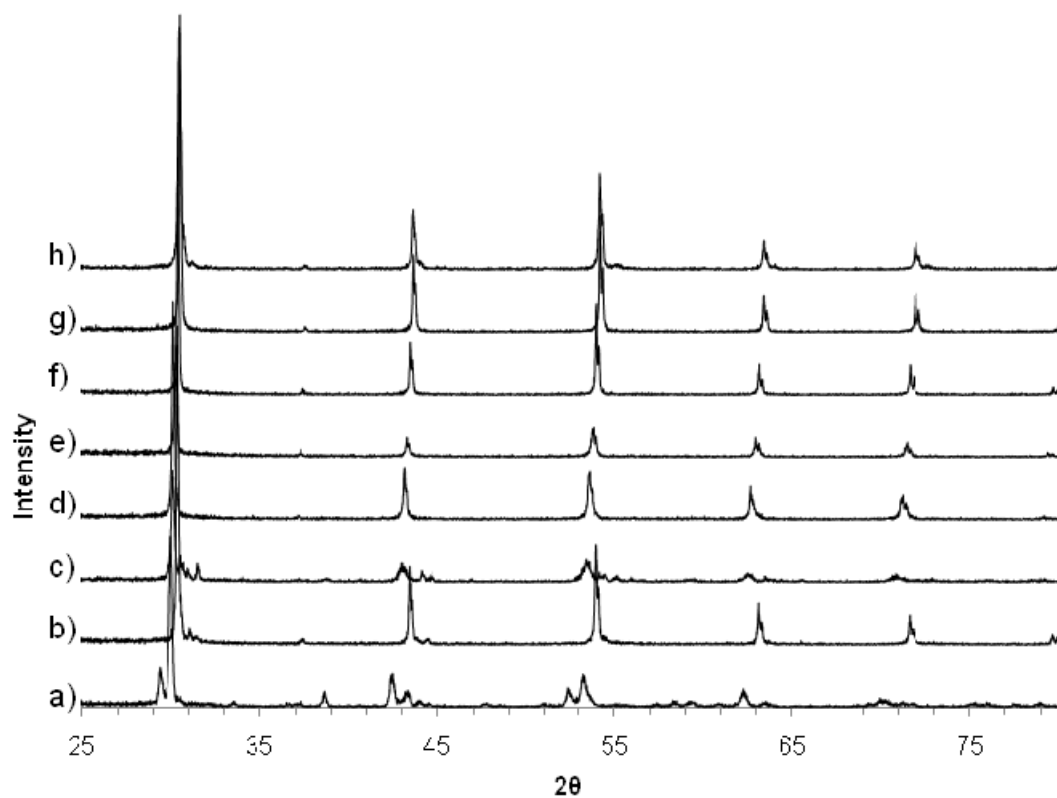
Figure 4.4 Powder x-ray diffraction of dry lanthanum doped barium indium oxide $(Ba_{1-x}La_x)_2In_2O_{5+x/2}$ samples for (a) x=0, (b) x=0.05, (c) x=0.1, (d) x=0.2, (e) x=0.25, (f) x=0.3, (g) x= 0.45, (h) x=0.6.
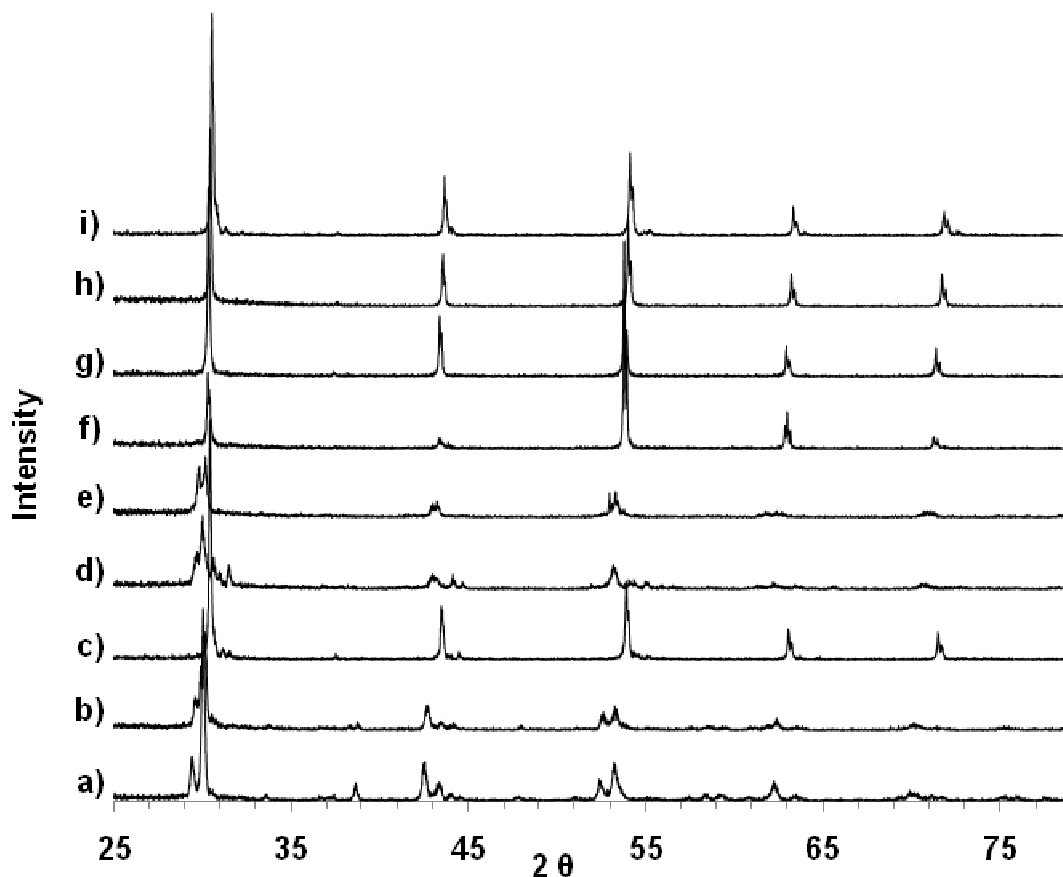
Figure 4.5 Powder x-ray diffraction of hydrated lanthanum doped barium indium oxide $(Ba_{1-x}La_x)_2In_2O_{5-x/2} \cdot H_2O$ samples for (a) x=0 (dry), (b) x=0 (fast hydrated), (c) x=0.05, (d) x=0.1, (e) x=0.2, (f) x=0.25, (g) x= 0.3, (h) x=0.45, (i) x=0.6.

4.3.2   Thermogravimetric Analysis (TGA)

In the thermogravimetric analysis (TGA) results for the undoped material shown in Figure 4.6, it can be seen that there is a clear correlation between the rate of cooling and the amount of moisture absorbed by barium indium oxide. First, a very subtle initial weight loss is observed due to the loss of surface water. The more significant weight loss occurs between 300-400°C, consistent with

143

earlier work. The material fast cooled by turning off the furnace indicates that the hydration uptake is 0.5%, corresponding to 0.17 moles of water per mole of sample, i.e. $Ba_2In_2O_5 \cdot H_2O$ (see Figure 4.6 – Fast Hydration). The uptake levels for samples slow cooled at 1°C/min and ultra-slow cooled at 0.1°C/min were 0.9% and 1.4% respectively (see Figure 4.6 – Slow and Ultra-Slow Hydration). This correlates to an insertion of 0.31mol and 0.47mol per mol of sample respectively. This is consistent with diffraction results showing that significantly more of the hydrated phase exists for the more slowly hydrated sample as seen in Figure 4.3. The mass increase observed in the TGA for the slowly hydrated sample between 600 and 950°C is not fully understood but is thought to possibly be due to CO_2 uptake, or instability in the instrument.

TGA results for La-doped samples show that, as previously reported in the literature[164] the water uptake is at a maximum for x=0.10. In the current study, the hydration level at x=0.1 was found to be the same as that for the slowly hydrated undoped sample at 0.9% correlating to an insertion of 0.31 moles of water per mole of sample, i.e. $(Ba_{0.9}La_{0.1})_2In_2O_{5.05} \cdot H_2O$. Hydration levels were found to be greatly diminished for higher doping levels (Figure 4.7), consistent with diffraction results in the current study indicating that there is little structural change in these samples upon hydration. The hydration level at x=0.1 is nearly twice the hydration level reported in the literature for this dopant level. This may be because achieving full hydration in these systems is extremely difficult and samples examined previously were not fully hydrated. No diffraction results are shown in the previous study to confirm hydration levels. Results in the current

study for x=0.05 demonstrate that the water uptake is unexpectedly low, i.e. on the order of samples with x>0.25. This is consistent with diffraction results in showing that a significant fraction of this sample demonstrates symmetry similar to samples with higher dopant levels.
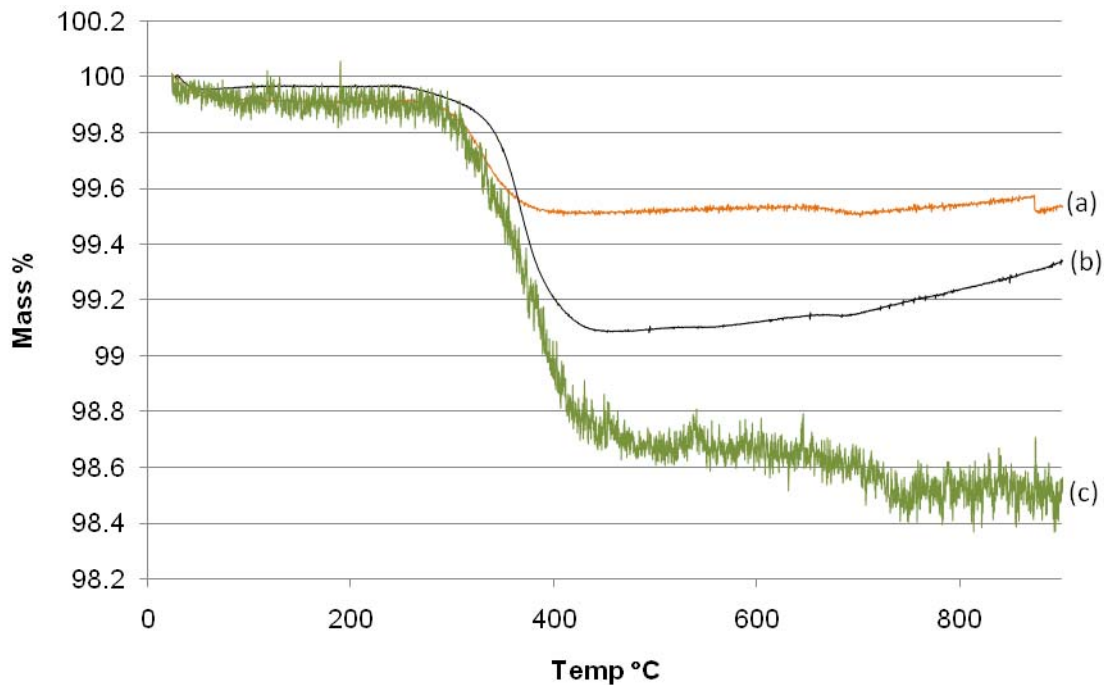
Figure 4.6 Thermogravimetric analyses (TGA's) of hydrated barium indium oxide $Ba_2In_2O_5 \cdot \delta H_2O$ samples for samples hydrated (a) by turning off furnace during cooling, (b) by cooling at a rate of 1°C/min between 350 and 250°C and (c) by cooling at a rate of 0.1°C/min between 350 and 250°C corresponding to hydration levels of δ = (a) 0.17, (b) 0.3, and (c) 0.47 moles of H_2O per mole of sample.
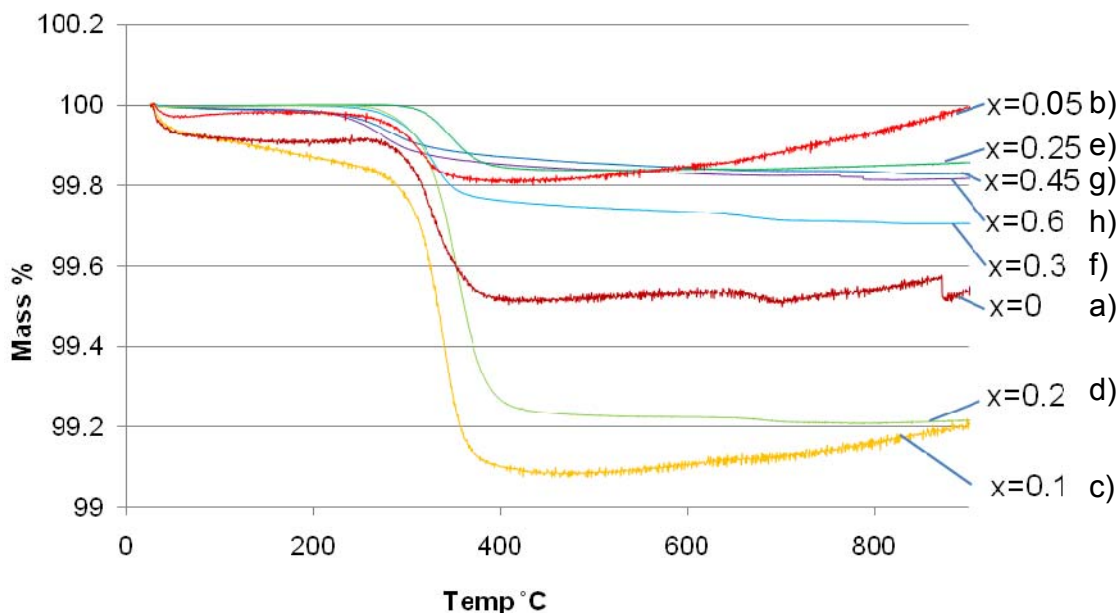
Figure 4.7 Thermogravimetric analyses (TGA's) of hydrated lanthanum doped barium indium oxide $(Ba_{1-x}La_x)_2In_2O_{5-x/2}\cdot\delta H_2O$ samples at (a) x=0, (b) 0.05, (c) 0.1, (d) 0.2, (e) 0.25, (f) 0.3, (g) 0.45 and (h) 0.60 corresponding to hydration levels of δ = (a) 0.17, (b) 0.07, (c) 0.31, (d) 0.27, (e) 0.06, (f) 0.10, (g) 0.06, and (h) 0.06 moles of H_2O per mole of sample.

4.3.3   Nuclear Magnetic Resonance (NMR)

Two sites are resolved in all the one-dimensional ^{1}H NMR spectra of the undoped $Ba_2In_2O_5\cdot H_2O$ samples with proton chemical shifts of 7.2 and 1.0ppm (see Figure 4.8). The resonance at 7.2ppm is assigned to protons bonded to interstitial oxygens in the tetrahedral layers, having an O(3)···O(3) bond length of approximately 2.81 Å (see Figure 4.2) according to diffraction data by Rolle[171]. This is in reasonably good agreement with the shift calculated using equation [4.5][177] at 7.4ppm. The resonance at 1.0ppm is then assigned to protons bonded to the O(2) site, having the longer (O(2)···O(3)) distance of 3.00 Å. This is also in reasonably good agreement with the calculated distance of 3.06 Å calculated

146

using equation [4.5][177]. Furthermore, this O(2) will not be H-bonded to the O(3) site in a linear H-bond. Upon heating, these two sites were found to lose their sidebands and to coalesce to form a peak with an intermediate shift of 4.0ppm as shown in Figures 4.8, 4.9, and 4.10 indicating that they are exchanging with one another on the spectral timescale (i.e., the timescale of the difference between the shift frequencies of each of the contributing sites i.e. 2.3 kHz). Variable temperature spectra of samples hydrated by fast cooling show resonance coalescence at around 200°C, whereas samples hydrated by slow cooling and ultra-slow cooling coalesce at 150 and 140°C respectively. The difference in coalescence temperature between the various hydration preparations is indicative of the close correlation between hydration levels and protonic hopping in these samples, as well as the sensitivity of the NMR experiment in its ability to examine this process in-situ. The disappearance of the higher field (1.0ppm) peak with increasing temperature also uncovers a third site at 0ppm (see Figure 4.2). The high field shift tells us that this site must be due to a highly shielded environment. This is the case for protons bound to very basic oxygen ions that are themselves very weak acids not involved in hydrogen bonding. The proton producing this resonance therefore may coordinated to an oxygen environment such as O(1) where strong hydrogen bonding to another oxygen site is not possible as suggested by the calculations by Islam et al. Secondly it may be that this site is from a second, less hydrated phase of the material. If insufficient protonation prevents significant tilting of the InO_6 octahedral units, proton containing oxygen sites may not be in close enough proximity to permit

exchange. This explanation is not entirely unreasonable given that the powder diffraction of these samples indicates that complete hydration has not occurred and that a second, less hydrated phase is present. However, because the intensity of this resonance increases with decreasing sample cooling rate, attributing it to a less hydrated phase is not particularly consistent with the TGA results, showing that there is a significant increase in moisture content for samples cooled more slowly during the hydration procedure. An alternative explanation is that this resonance may be due to a hydrated impurity in the sample formed during the hydration process. Based on what is believed to be the more probable scenario, the 0.0ppm resonance is tentatively attributed to barium hydroxide impurities in the samples. It is believed that this explanation is reasonable given the very basic nature of the oxygen environment in barium hydroxide and the lack of exchange between this site and the other two. From this it can be inferred that this site is not in close enough proximity to oxygens within the barium indium oxide lattice to exchange with them. Given the diffraction pattern of barium hydroxide, we cannot confirm by this method whether or not this is the case. While the NMR chemical shift of pure, crystalline barium hydroxide is 1.6ppm, it is possible that within the barium indium oxide sample, this resonance is shifted to 0.0ppm, or that this is an amorphous or poorly crystalline phase. It is also observed that the proportion of the peak at 0.0ppm increases with increasing hydration levels observed in these samples by TGA. This may because the longer prepatory method for the more hydrated sample promotes the formation of this impurity.

4.4   Two-Dimensional NMR

Two-dimensional exchange spectra show that there is an onset of proton hopping even for mixing times as short as 500 µs (not shown) by cross-peaks appearing between the 1.0 and 7.2ppm resonance. Full exchange, however, is not achieved even for mixing times as long as 100 ms (see Figure 4.11 (c)). As the temperature is increased slightly to 100°C, the exchange rate becomes much more rapid as can be observed in the increased cross peak intensity between the room temperature spectrum with a mixing time of 10 ms shown in Figure 4.12 (a), and the spectrum at 100°C shown in Figure 4.12 (b). Slices were taken at the frequencies corresponding to the three resonances in the one dimensional spectra to explore the exchange between the sites. Although it is difficult to rule out exchange between the environments giving rise to the 0.0ppm and 1.0ppm peaks due to the severe overlap between these peaks, a slice through the resonance at 7.2ppm clearly shows that exchange only involves the 1.0 and 7.2ppm resonances. This is much clearer in the spectra obtained at 250°C where there is no cross peak observed between the coalesced peak at 4.0ppm between the 1.0 and 7.2ppm resonances and the residual 0.0ppm peak (Figure 4.12 (c)). This is further evidence that this resonance is due to a proton source not in the crystal lattice.
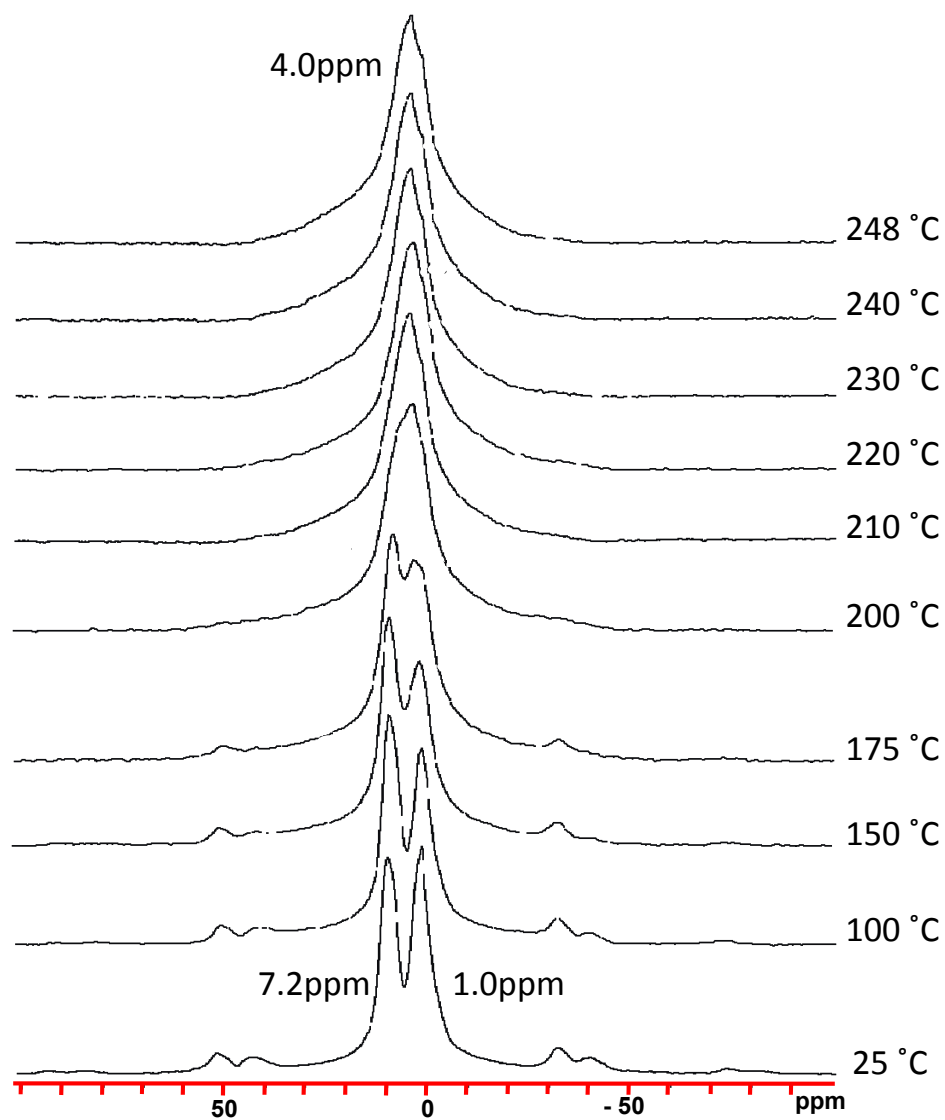
Figure 4.8 Variable temperature ^{1}H MAS NMR spin echo spectra of Ba$_2$In$_2$O$_5$•H$_2$O sample fast cooled by turning off furnace at a field strength of 360 MHz and an MAS frequency of 15 kHz.
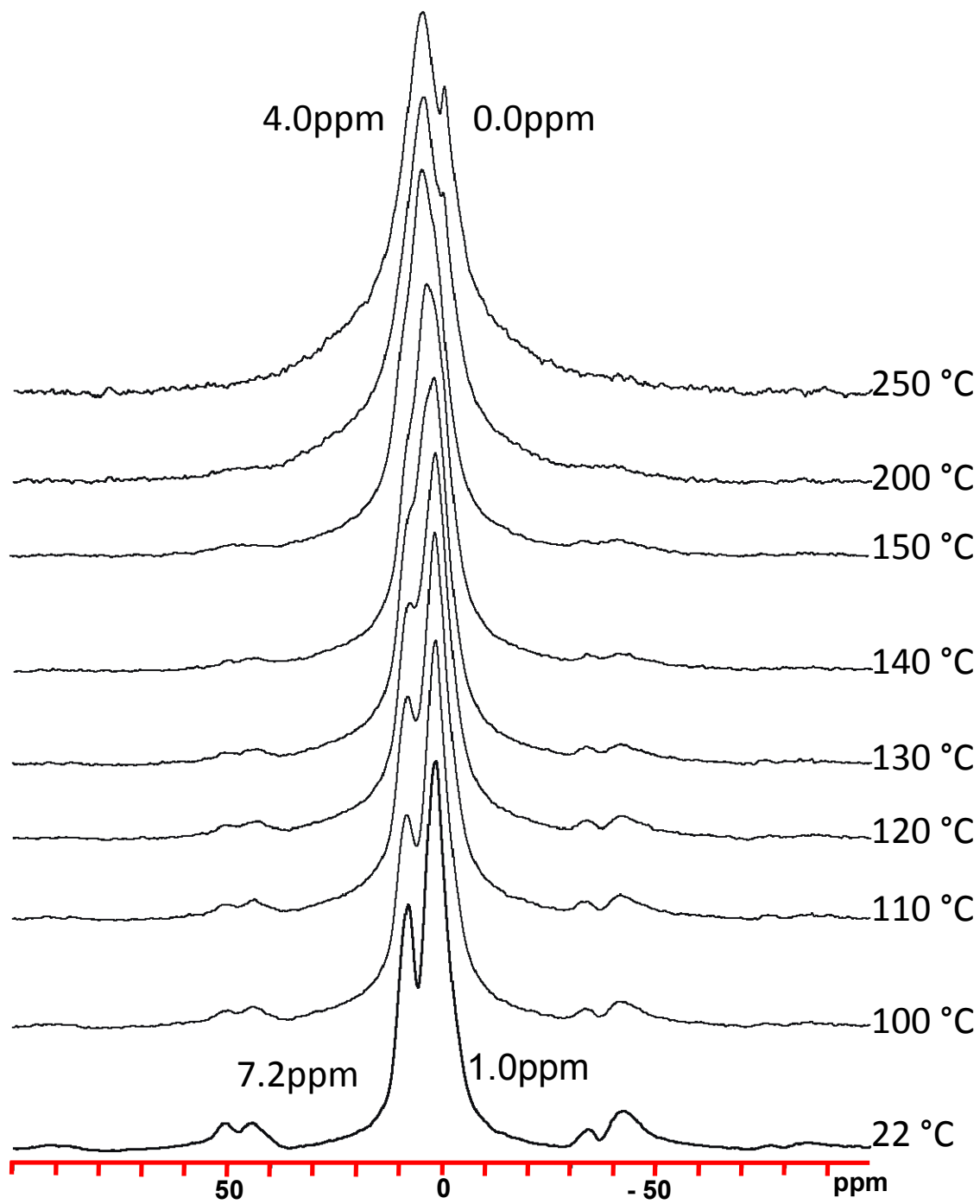
Figure 4.9 Variable temperature ^{1}H MAS NMR spin echo spectra of $Ba_2In_2O_5 \cdot H_2O$ sample cooled from 350-250 °C at 1 °C/min at a field strength of 360 MHz and a spinning speed of 15 kHz.
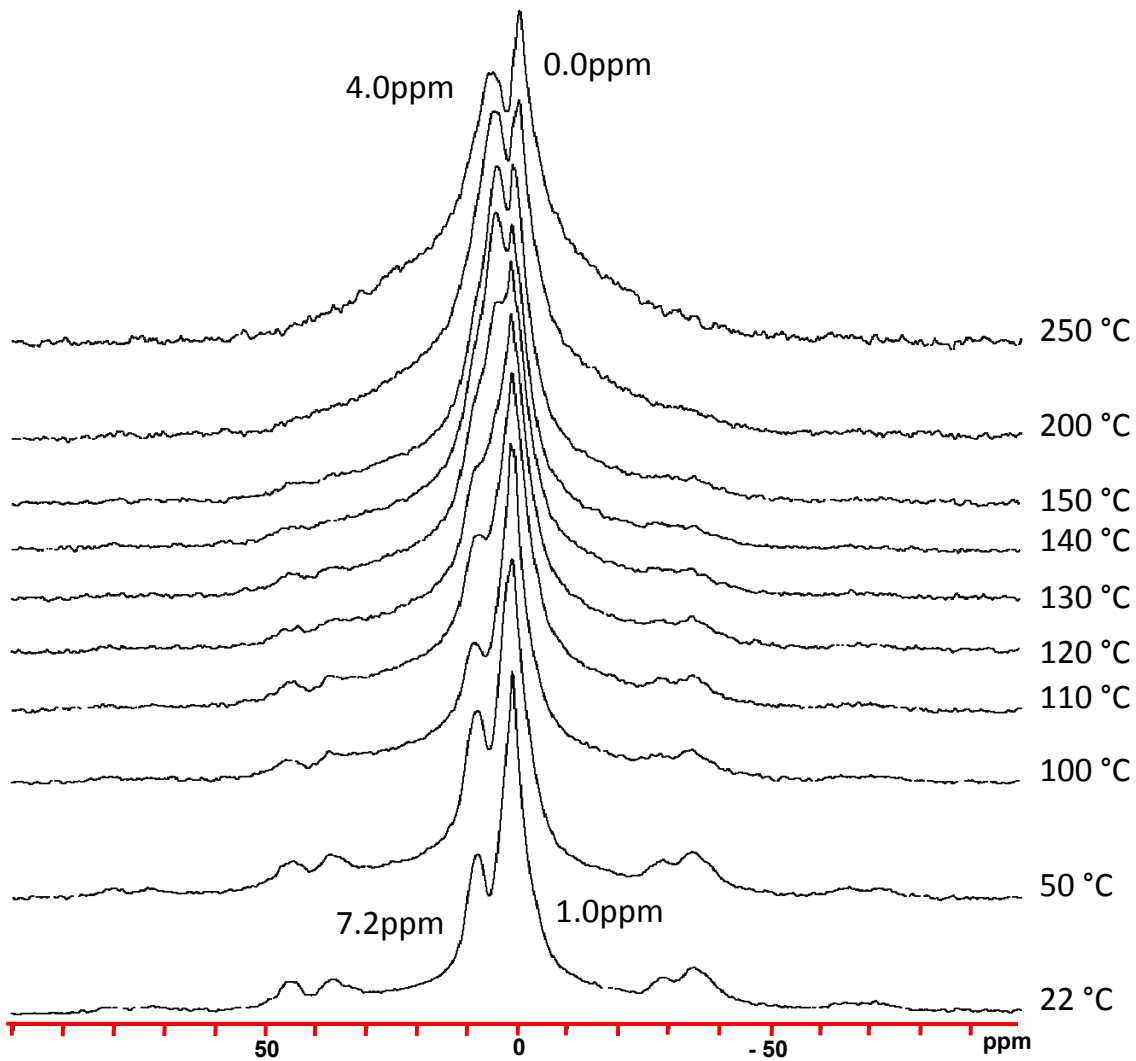
Figure 4.10 Variable temperature ^1H MAS NMR spin echo spectra of $Ba_2In_2O_5 \cdot H_2O$ sample cooled from 350-250 °C at 0.1 °C/min at a field strength of 360 MHz and a spinning speed of 15 kHz.
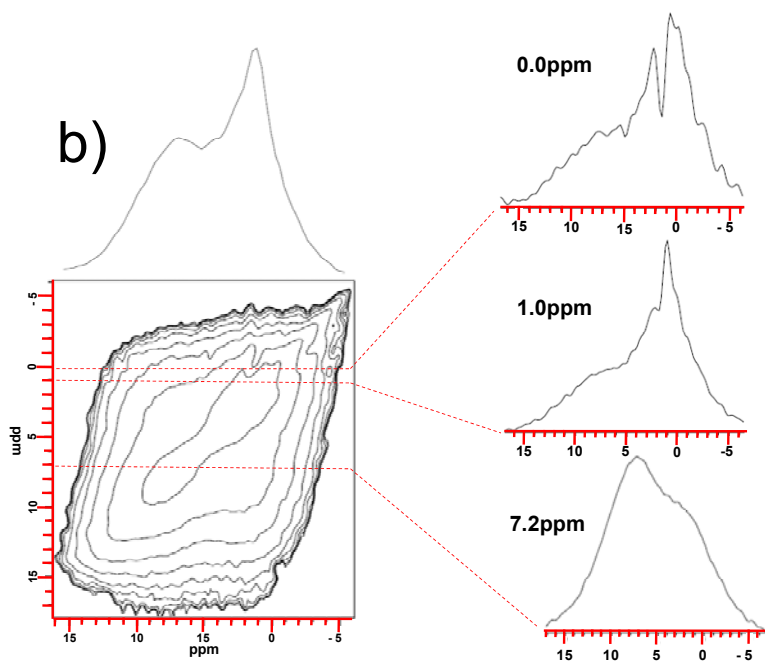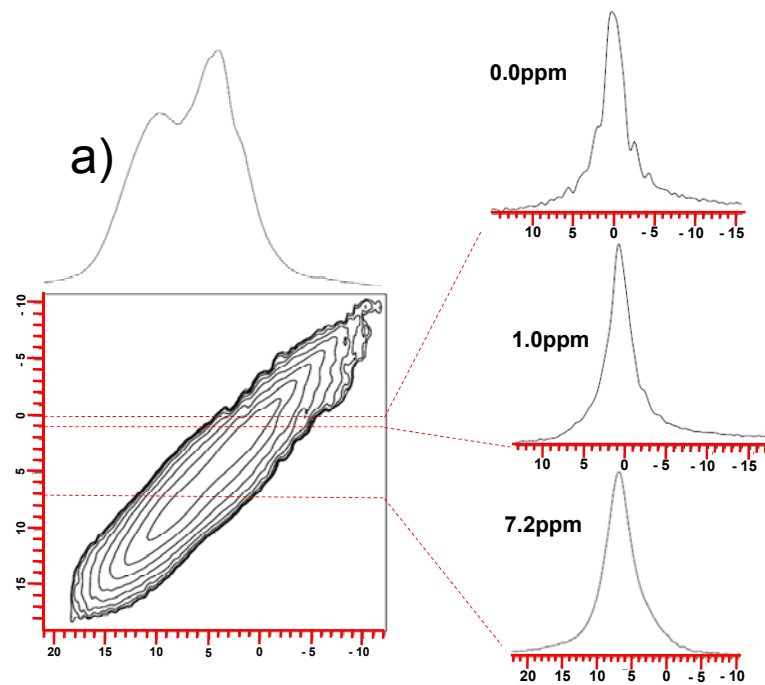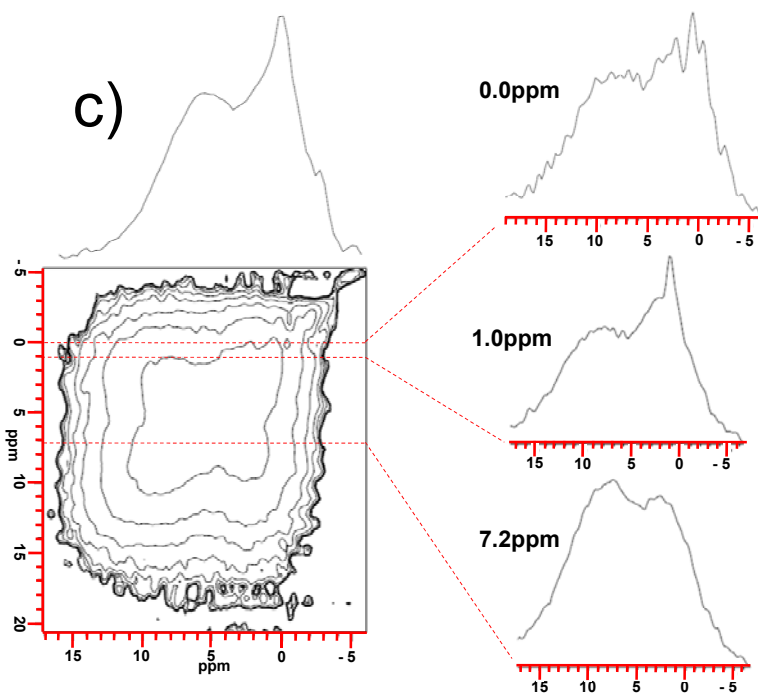
Figure 4.11 ^{1}H 2D exchange (EXSY) NMR spectrum of barium indium oxide hydrated by ultra-slow cooling between 350 and 250°C at a rate of 0.1°C/min at a field strength of 500 MHz, room temperature and a spinning speed of 15 kHz with a mixing time of a) 0.10, b) 10, c) 100 milliseconds.
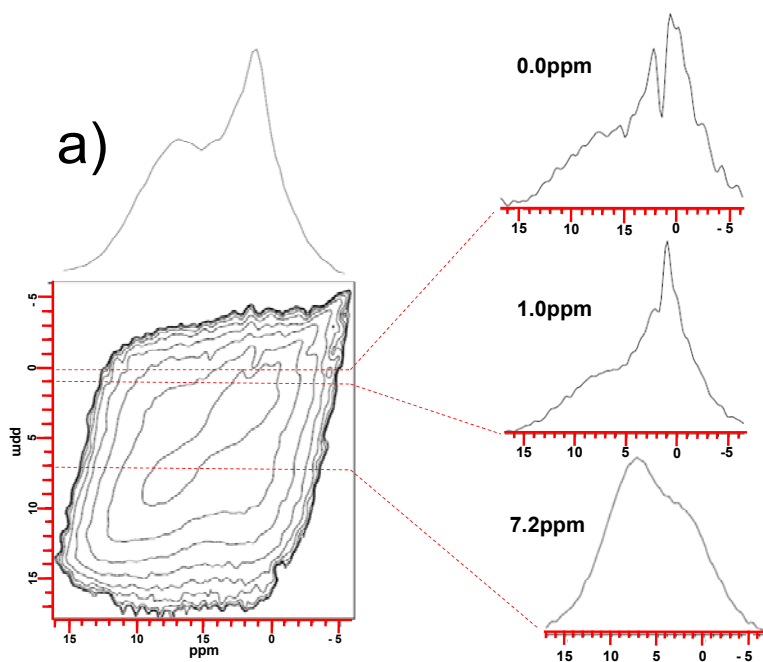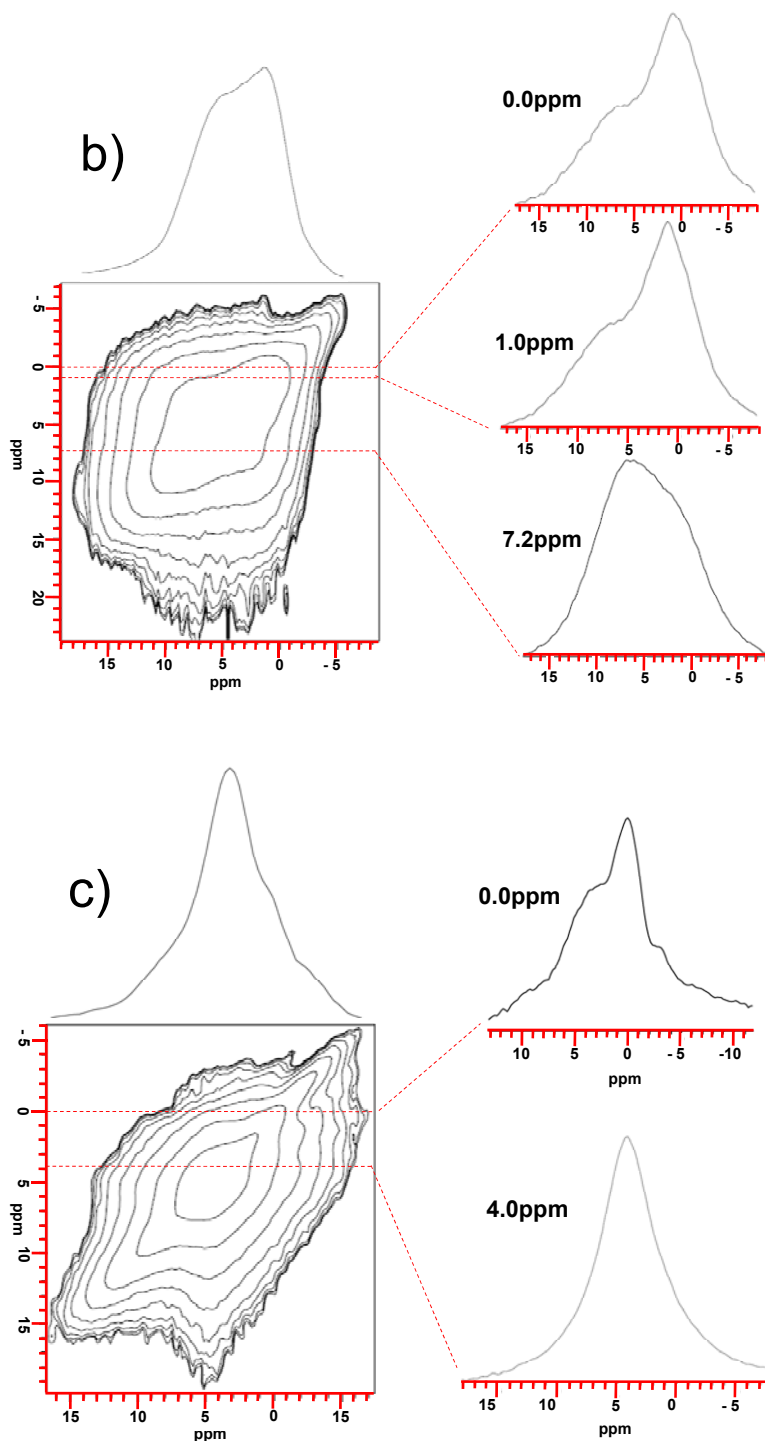
Figure 4.12 ^{1}H 2D exchange (EXSY) NMR spectrum of barium indium oxide hydrated by ultra-slow cooling between 350 and 250°C at a rate of 0.1°C/min at a field strength of 500 MHz, a spinning speed of 15 kHz and a mixing time of 10 ms at a) Room Temperature, b) 100°C and c) with a mixing time of 0.5 ms at 250°C.

4.5   Discussion

4.5.1   Proton Exchange Rates

From examination of the one dimensional variable temperature data, the hop frequency of protons on the spectral timescale as a function of temperature can be ascertained. Coalescence occurs when the exchange rate between the two sites is greater than or equal to $1/2\nu_{AB}$, where ν_{AB} is the frequency separation between the two resonances. The proton hop frequency must then be equal to or more rapid than 1.6 kHz at each coalescence temperature. Because we are best able to resolve the 1.0ppm peak in the fast hydrated sample, line-shape simulations of this sample as a function of temperature were performed. These indicate that, at room temperature, proton exchange is around 450 Hz, and increases to around 750 Hz at 175°C, and finally coalesces around 200°C.

In order to determine the hop frequency on a slower timescale, two dimensional exchange experiments were performed as described above. An effort was made at fitting a plot of the deconvoluted cross/diagonal peak ratios against the experimental mixing time in the EXSY experiments, but these fits were too poor to derive significant information. From this it was determined qualitatively that there is a large distribution in correlation times for these systems.

4.5.2 Pathway for Motion

While previous authors[84] have attributed the presence of three distinct proton environments in the solid state NMR spectra of hydrated barium indium oxide to differences in proton local environments in various regions of the extended unit cell, dynamic evidence from variable temperature one and two-dimensional experiments in the current work causes us to have to disagree with this assessment. We are of the belief that the three environments observed are not in fact split sites, but may be attributed to a barium hydroxide impurity or different hydration phases within the sample. As evidenced by coalescence of these two peaks in variable temperature one-dimensional spectra, the two types of protons attributed to the hydrated barium indium oxide crystal lattice do in fact appear to exchange with one another.

The fact that the two-dimensional exchange spectra also shows exchange between these resonances would further imply that the pathway for motion is not in fact limited to two dimensional diffusion within the interstitial O(3) spaces ([001] direction) as was previously thought based on simulation data[145,168]. While this may be a correct assessment that the primary mode of proton migration occurs between the interstitial –OH protons, the NMR data would imply that the proton in actuality does trace a two-dimensional pathway between interstitial O(3) and O(2) environments, at least on slow timescales. However, further experimentation is necessary to unequivocally state that this is in fact a viable motional pathway in this system.

4.6 Conclusions

The results of all of the experiments in this study emphasize the previous assessment that the level of moisture uptake in barium indium oxide and its doped analogs is very sensitive to the cooling rate of hydration. X-ray powder diffraction spectra of undoped material clearly show that achieving complete hydration for this system is difficult and that different hydration phases are present to varying degrees in samples hydrated under various cooling rates. Diffraction results for lanthanum doped species show that there are almost no structural changes in these materials with hydration. This is not surprising as hydration of the undoped material increases the symmetry from orthorhombic to tetragonal, where the La-doped species are already of more highly symmetric cubic symmetry for higher dopant levels. Thermogravimetric analyses (TGA) of the undoped material confirm that the hydration level of this system is highly subject to cooling rate, with samples having been cooled at 0.1°C/min taking on three times the amount of moisture per mole of sample when compared to samples having been fast cooled by simply turning off the furnace during cooling. TGA results for La-doped samples confirms previous results that the x=0.1 formulation takes on the largest quantity of water, where moisture uptake drops off precipitously for higher dopant levels. We have further demonstrated that solid state NMR is very sensitive to moisture content in these samples and can therefore be used to discern between hydration levels. In the one-dimensional spectra of the undoped material, two sites are resolved at room temperature, and a third, less hydrogen bonded site becomes apparent at high temperature. This

site may be due to a protonated site in the crystal lattice which is not in close enough proximity to other sites to exchange, or may be indicative of the presence of impurities forming during the hydration process. As this site increases in intensity with increased hydration levels, it may be an indication that allowing these samples to achieve large levels of hydration may come at the expense of having large numbers of impurities. While resolution between diagonal and cross peaks in two-dimensional exchange spectra are too poor to ascertain exchange rates and activation energies, a qualitative examination of them confirms that the 0.0ppm site visible only at high temperature is not in fact exchanging with the other sites.

Bibliography

(1)   West, A. R. *Solid State Chemistry and Its Applications*; 1st ed.; John Wiley & Sons Ltd., 1984.

(2)   Smart, L.; Moore, E. *Solid State Chemistry: An Introduction*; 2nd ed.; Nelson Thornes: Cheltenham, UK, 1995.

(3)   Contributors, W.; Wikipedia, The Free Encyclopedia: 2008; Vol. 2008.

(4)   U.S. Department of Defense Fuel Cell Test and Evaluation Center (FCTec): Johnstown, PA, 2001.

(5)   De Guire, E. J. In *ProQuest Discovery Guides*; CSA: 2003.

(6)   Contributors, W.; Wikipedia, The Free Encyclopedia: 2008; Vol. 2008.

(7)   Shuk, P.; Wiemhöfer, H. D.; Guth, U.; Göpel, W.; Greenblatt, M. *Solid State Ionics* **1996**, *89*, 179-196.

(8)   Kreuer, K. D. *Annual Review of Materials Research* **2003**, *33*, 333-359.

(9)   Chaudhuri, S.; Wang, F.; Grey, C. P. *Journal of the American Chemical Society* **2002**, *124*, 11746-11757.

(10)   Kim, N. Doctor of Philosophy, State University of New York at Stony Brook, 2004.

(11)   Kim, N.; Grey, C. P. *Science* **2002**, *297*, 1317-1320.

(12)   Wang, F.; Grey, C. P. *Chemistry of Materials* **1997**, *9*.

(13)   Adler, S. B.; Reimer, J. A.; Baltisberger, J.; Werner, U. *Journal of the American Chemical Society* **1994**, *116*, 675-681.

(14)   Holmes, L.; Peng, L.; Heinmaa, I.; x; Dell, L. A.; Smith, M. E.; Vannier, R.-N.; Grey, C. P. *Chem. Mater.* **2008**, *20*, 3638-3648.

(15)   Fu, R.; Ma, Z.; Zheng, J. P. *J. Phys. Chem. B* **2002**, *106*, 3592-3596.

(16)   Maekawa, H.; Ukei, Y.; Morota, K.; Kashii, N.; Kawamura, J.; Yamamura, T. *Solid State Communications* **2004**, *130*, 73-77.

(17)   Jayaraman, V.; Magrez, A.; Caldes, M.; Joubert, O.; Taulelle, F.; Rodriguez-Carvajal, J.; Piffard, Y.; Brohan, L. *Solid State Ionics* **2004**, *170*, 25-32.

(18)   Tambelli, C. E.; Donoso, J. P.; Magon, C. J.; Ângelo, A. C. D.; Florentino, A. O.; Saeki, M. J. *Solid State Ionics* **2000**, *136-137*, 243-247.

(19)   Maekawa, H.; Kashii, N.; Kawamura, J.-I.; Hinatsu, Y.; Yamamura, T. *Solid State Ionics* **1999**, *122*, 231-236.

(20)   Hodgkinson, P. In *Solid-State NMR Research Service Training Day* University of Durham, 2004.

(21)   Levitt, M. H. *Spin Dynamics: Basics of Nuclear Magnetic Resonance*; 1st ed.; John Wiley & Sons: New York, 2002.

(22)   Jeener, J.; Meier, B. H.; Bachmann, P.; Ernst, R. R. *Journal of Chemical Physics* **1979**, *71*, 4546-4553.

(23)   Hampson, M. R.; Hodgkinson, P.; Evans, J. S. O.; Harris, R. K.; King, I. J.; Allen, S.; Fayon, F. 2004, p 392-393.

(24)   Hampson, M. R.; Hodgkinson, P.; Evans, J. S. O.; Harris, R. K.; Kinga, I. J.; Allena, S.; Fayon, F. *Chemical Communications* **2004**, *2004*, 392-393.

(25)   Duer, M. J. *Introduction to Solid-State NMR Spectroscopy*; 1st ed.; Blackwell Publishing LTD: Oxford, UK, 2004.

(26)   Slichter, C. P. *Principles of Magnetic Resonance*; 3rd ed.; Springer-Verlag: New York, 1990; Vol. 1.

(27)   Grey, C. P.; Phillips, B. In *CEMS NMR Workshop*; Interaction, C. D. a. S. L. M. D. S. B. R. T. Q., Ed. Stony Brook, 2003.

(28)   Winter, M. J. 2003.

(29)   Frydman, L.; Harwood, J. S. *Journal of the American Chemical Society* **1995**, *117*, 5367-5368.

(30)   David D. Laws, H.-M. L. B. A. J. *Angewandte Chemie International Edition* **2002**, *41*, 3096-3129.

(31)   Taulelle, F. In *Multi-nuclear Magnetic Resonance in Liquids and Solids - Chemical Applications*; Granger, P., Harris, R. K., Eds.; Kluwer Academic Publishers: 1990, p 393-407.

(32)   Medek, A.; Harwood, J. S.; Frydman, L. *Journal of the American Chemical Society* **1995**, *117*, 12779-12787.

(33)   Goldbourt, A.; Madhu, P. K. *Monatshefte für Chemie* **2002**, *133*, 1497-1534.

(34)   Dowell, N. G.; Ashbrook, S. E.; McManus, J.; Wimperis, S. *Journal of the American Chemical Society* **2001**, *123*, 8135-8136.

(35)   MacKenzie, K. J. D.; Smith, M. E. *Multinuclear Solid-State NMR of Inorganic Materials*; 1st ed.; Elsevier Science Ltd.: Cambridge, UK, 2002; Vol. 6.

(36)   Sideris, P. In *Grey Group Meeting August 2004*; State University of New York at Stony Brook: 2004.

(37)   Man, P. P. In *Encyclopedia of Analytical Chemistry*; Meyers, R. A., Ed.; John Wiley & Sons Ltd.: Chichester, 2000, p 12224-12265.

(38)   Duer, M. J.; Painter, A. J. *Chemical Physics Letters* **1999**, *313*, 763-770.

(39)   Amoureux, J.-P.; Fernandez, C.; Steuernagel, S. *Journal of Magnetic Resonance, Series A* **1996**, *123*, 116-118.

(40)   Nielsen, U. G. PhD, University of Aarhus, 2002.

(41)   Samoson, A.; Lippmaa, E.; Pines, A. *Molecular Physics* **1988**, *65*, 1013-1018.

(42)   Wu, Y.; Sun, B. Q.; Pines, A.; Samoson, A.; Lippmaa, E. *Journal of Magnetic Resonance* **1990**, *89*, 297-309.

(43)   Gann, S. L.; Baltisberger, J. H.; Pines, A. *Chemical Physics Letters* **1993**, *210*, 405-410.

(44)   Grandinetti, P. J.; Baltisberger, J. H.; Llor, A.; Lee, Y. K.; Werner, U.; Eastman, M. A.; Pines, A. *Journal of Magnetic Resonance, Series A* **1993**, *103*, 72-81.

(45)   Grandinetti, P. J.; Lee, Y. K.; Baltisberger, J. H.; Sun, B. Q.; Pines, A. *Journal of Magnetic Resonance, Series A* **1993**, *102*, 195-204.

(46)   Sun, B. Q.; Baltisberger, J. H.; Wu, Y.; Samoson, A.; Pines, A. *Solid State Nuclear Magnetic Resonance* **1992**, *1*, 267-295.

(47)   Eastman, M. A.; Grandinetti, P. J.; Lee, Y. K.; Pines, A. *Journal of Magnetic Resonance (1969)* **1992**, *98*, 333-341.

(48)   Mueller, K. T.; Chingas, G. C.; Pines, A. *Review of Scientific Instruments* **1991**, *62*, 1445.

(49)   Mueller, K. T.; Sun, B. Q.; Chingas, G. C.; Zwanziger, J. W.; Terao, T.; Pines, A. *Journal of Magnetic Resonance (1969)* **1990**, *86*, 470-487.

(50)   Llor, A.; Virlet, J. *Chemical Physics Letters* **1988**, *152*, 248-253.

(51)   Chmelka, B. F.; Mueller, K. T.; Pines, A.; Stebbins, J.; Wu, Y.; Zwanziger, J. W. *Nature* **1989**, *339*, 42-43.

(52)   Amoureux, J. P.; Fernandez, C. *Solid State Nuclear Magnetic Resonance* **1998**, *10*, 211-223.

(53)   Amoureux, J. P.; Fernandez, C. *Solid State Nuclear Magnetic Resonance* **2000**, *16*, 339-343.

(54)   Akitt, J. W.; Mann, B. E. *NMR and Chemistry: An Introduction to Modern NMR Spectroscopy*; 4th ed.; Nelson Thornes, 2000.

(55)   Smith, S. 2005.

(56)   Hore, P. J. *Nuclear Magnetic Resonance*; 1st ed.; Oxford University Press: Oxford, UK, 1995.

(57)   Breitmaier, P. D. E.; Spohn, D. K.-H.; Berger, D. S. *Angewandte Chemie* **1975**, *14*, 144-159.

(58)   Kidd, R. G. In *NMR of Newly Accessible Nuclei*; Laszlo, P., Ed.; Academic Press Inc.: New York, 1983; Vol. 1, p 298.

(59)   Atkins, P. *Physical Chemistry, Fifth Ed.*; 5th ed.; W.H. Freeman and Company: New York, 1994.

(60)   Bull, T. E.; Forsen, S.; Turner, D. L. *Journal of Chemical Physics* **1979**, *70*, 3106-3111.

(61)   Hubbard, P. S. *The Journal of Chemical Physics* **1970**, *53*, 985-987.

(62)   Andrew, E. R.; Tunstall, D. P. *Proceedings of the Physical Society* **1961**, *78*, 1-11.

(63)   McDowell, A. F.; Snyderman, D. M.; Conradi, M. S.; Silbernagel, B. G.; Stacy, A. M. *Physical Review B* **1994**, *50*, 15764-15774.

(64)   McDowell, A. F. *Journal of Magnetic Resonance, Series A* **1995**, *113*, 242-246.

(65)   Hodgkinson, P.; Hampson, M. R.; University of Durham: 2005, p 15.

(66)   Hampson, M. R.; Evans, J. S. O.; Hodgkinson, P.; Durham University: 2005, p 21.

(67)   Johnston, D. C.; Baek, S.-H.; Zong, X.; Borsa, F.; Schmalian, J.; Kondo, S.; Ames Laboratory and Department of Physics and Astronomy, Iowa State University: 2005, p 4.

(68)   Kohlrausch, R. *Pogg. Ann. Phys. Chem.* **1854**, *91*, 179.

(69)   Cardona, M.; Chamberin, R. V.; Marx, W. *Ann. Phys. (Leipzig)* **2007**, *16*, 842-845.

(70)   Berberan-Santos, M.; Bodunov, E. N.; Valeur, B. *arXiv.org, e-Print Archive, Physics* **2008**, *arXiv:0804.1814v1 [physics.hist-ph]*, 1-3.

(71)   Williams, G.; Watts, D. C. *Transactions of the Faraday Society* **1970**, *66*, 80-85.

(72)   Williams, G.; Watts, D. C. *Transactions of the Faraday Society* **1971**, *67*, 1323-1335.

(73)   Narayanan, A.; Hartman, J. S.; Bain, A. D. *Journal of Magnetic Resonance, Series A* **1995**, *112*, 58-65.

(74)   Kaps, H.; Brando, M.; Trinkl, W.; Büttgen, N.; Loidl, A.; Scheidt, E.-W.; Klemm, M.; Horn, S. *Journal of Physics: Condensed Matter* **2001**, *13*, 8497-8508.

(75)   París, M. A.; Sanz, J.; León, C.; Santamaría, J.; Ibarra, J.; Várez, A. *Chem. Mater.* **2000**, *12*, 1694-1701.

(76)   Wachsman, E. D.; Boyapati, S.; Kaufman, M. J.; Jiang, N. *Electrochemical Society Proceedings* **1999**, *99-13*, 42-51.

(77)   Yaremchenko, A. A.; Kharton, V. V.; Naumovich, E. N.; Tonoyan, A. A. *Materials Research Bulletin* **2000**, *35*, 515-520.

(78)   Medvedeva, N. I.; Zhukov, V. P.; Gubanov, V. A.; Novikov, D. L.; Klein, B. M. *Journal of Physics and Chemistry of Solids* **1996**, *57*, 1243-1250.

(79)   Subbarao, E. C.; Maiti, H. S. *Solid State Ionics* **1984**, *11*, 317-338.

(80)   Hapase, M. G.; Tare, V. B.; Biswas, A. B. *Indian Journal of Pure and Applied Physics* **1967**, *5*, 401-404.

(81)   Takahashi, T.; Iwahara, H. *Journal of Applied Electrochemistry* **1973**, *3*, 65-72.

(82)   Takahashi, T.; Iwahara, H.; Esaka, T. *Journal of The Electrochemical Society* **1977**, *124*, 1563-1569.

(83)   Takahashi, T.; Iwahara, H.; Nagai, Y. *Journal of Applied Electrochemistry* **1972**, *2*, 97-104.

(84)   Jayaraman, V.; Magrez, A.; Caldes, M.; Joubert, O.; Taulelle, F.; Rodriguez-Carvajal, J.; Piffard, Y.; Brohan, L. *Solid State Ionics* **2004**, *170*, 25-32.

(85)   Vannier, R.-N.; Mairesse, G.; Abraham, F.; Nowogrocki, G. *Journal of Solid State Chemistry* **1996**, *122*, 394-406.

(86)   Abraham, F.; Boivin, J. C.; Mairesse, G.; Nowogrocki, G. *Solid State Ionics* **1990**, *40-41*, 934-7.

(87)   Vannier, R.-N.; Danzé, S.; Nowogrocki, G.; Huvé, M.; Mairesse, G. *Solid State Ionics* **2000**, *136-137*, 51-59.

(88)   Vannier, R.-N.; Abraham, F.; Nowogrocki, G.; Mairesse, G. *Journal of Solid State Chemistry* **1999**, *142*, 294-304.

(89)   Galy, J.; Salles, P.; Rozier, P.; Castro, A. *Solid State Ionics* **2006**, *177*, 6.

(90)   Enjalbert, R.; Hasselmann, G.; Galy, J. *Journal of Solid State Chemistry* **1997**, *131*, 236-245.

(91)   Buttery, D. J.; Vogt, T.; Yap, G. P. A.; Rheingold, A. L. *Materials Research Bulletin* **1997**, *32*, 947-963.

(92) Galy, J.; Enjalbert, R.; Rozier, P.; Millet, P. *Solid State Sciences* **2003**, *5*, 165-174.

(93) Kim, N.; Vannier, R.-N.; Grey, C. P. *Chemistry of Materials* **2005**, *17*, 1952-1958.

(94) Samoson, A.; Tuherm, T.; Past, J.; Reinhold, A.; Anupold, T.; Heinmaa, I. *Topics in Current Chemistry* **2005**, *246*, 15-31.

(95) Samoson, A.; Heinmaa, I.; Tuherm, T.; Reinhold, A.; Past, J.; Stern, R.; Anupold, T.; Not Classified ed.; Bureau, W. I. P. O.-I., Ed. Estonia, 2005.

(96) O'Dell, L. A.; Savin, S. L. P.; Chadwick, A. V.; Smith, M. E. *Faraday Discussions* **2007**, *134*, 83-102.

(97) Yang, S.; Park, K. D.; Oldfield, E. *Journal of the American Chemical Society* **1989**, *111*, 7278-7279.

(98) Olivieri, A. C. *Solid State Nuclear Magnetic Resonance* **1992**, *1*, 345-353.

(99) Emery, J.; Massiot, D.; Lacorre, P.; Laligant, Y.; Conder, K. *Magnetic Resonance in Chemistry* **2005**, *43*, 366-371.

(100) Hampson, M. R.; Evans, J. S. O.; Hodgkinson, P. *Journal of the American Chemical Society* **2005**, *127*, 15175-15181.

(101) Maricq, M. M.; Waugh, J. S. *The Journal of Chemical Physics* **1979**, *70*, 3300-3316.

(102) Vega, A. J. In *Encyclopedia of Nuclear Magnetic Resonance*; Wiley: New York, p 3869-3888.

(103) Suter, A.; Mali, M.; Roos, J.; Brinkmann, D. *Journal of Magnetic Resonance* **2000**, *143*, 266-273.

(104) Yesinowski, J. P. *Journal of Magnetic Resonance* **2006**, *180*, 147-161.

(105) Gordon, M. I.; Hoch, M. J. R. *Journal of Physics C: Solid State Physics* **1978**, *11*, 783-795.

(106) Werbelow, L.; Pouzard, G. *Journal of Physical Chemistry* **1981**, *85*, 3887-3891.

(107) Adler, S.; Russek, S.; Reimer, J.; Fendorf, M.; Stacy, A.; Huang, Q.; Santoro, A.; Lynn, J.; Baltisberger, J.; Werner, U. *Solid State Ionics* **1994**, *68*, 193-211.

(108) Speiss, H. W. In *NMR - Basic Principles and Progress* 1978; Vol. 15, p 117.

(109) Wachsman, E. D.; Boyapati, S.; Kaufman, M. J.; Jiang, N. In *International Symposium on Solid-State Ionic Devices* 1999; Vol. 99-13, p 42-51.

(110) Yaremchenko, A. A.; Kharton, V. V.; Naumovich, E. N.; Tonoyan, A. A. *Materials Research Bulletin* **2000**, *35*.

(111) Medvedeva, N. I.; Zhukov, V. P.; Gubanov, V. A.; Novikov, D. L.; Klein, B. M. *Journal of Physics and Chemistry of Solids* **1996**, *57*.

(112) Takahashi, T.; Iwahara, H.; Nagai, Y. *Journal of Applied Electrochemistry* **1972**, *2*.

(113) Takahashi, T.; Iwahara, H.; Esaka, T. *Journal of the Electrochemical Society* **1977**, *124*.

(114) Takahashi, T.; Iwahara, H. *Journal of Applied Electrochemistry* **1973**, *3*.

(115) Hapase, M. G.; Tare, V. B.; Biswas, A. B. *Indian Journal of Pure and Applied Physics* **1967**, *5*, 401.

(116) Kendall, K. R.; Navas, C.; Thomas, J. K.; Loye, H.-C. z. *Solid State Ionics* **1995**, *82*, 215-223.

(117) Goodenough, J. B.; Ruiz-Diaz, J. E.; Zhen, Y. S. *Solid State Ionics* **1990**, *44*, 21-31.

(118) Islam, M. S.; Davies, R. A.; Fisher, C. A. J.; Chadwick, A. V. *Solid State Ionics* **2001**, *145*, 333-338.

(119) Kharton, V. V.; Marques, F. M. B.; Atkinson, A. *Solid State Ionics* **2004**, *174*, 14.

(120) Prasanna, T. R. S.; Navrotsky, A. *Journal of The Materials Research Society* **1993**, *8*, 1484-1486.

(121) Mohn, C. E.; Allan, N. L.; Freeman, C. L.; Ravindran, P.; Stølen, S. *Journal of Solid State Chemistry* **2005**, *178*, 346-355.

(122) Yoshinaga, M.; Fumoto, T.; Hashimoto, T. *Journal of The Electrochemical Society* **2005**, *152*, A1221-A1225.

(123)   Hashimoto, T.; Ueda, Y.; Yoshinaga, M.; Komazaki, K.; Asaoka, K.; Wang, S. *Journal of The Electrochemical Society* **2002**, *149*, A1381-A1384.

(124)   Rolle, A.; Vannier, R. N.; Giridharan, N. V.; Abraham, F. *Solid State Ionics* **2005**, *176*, 2095-2103.

(125)   Colville, A. A.; Geller, S. *Acta Crystallographica Section B* **1971**, *27*, 2311-2315.

(126)   Steele, B. C. H. In *High Conductivity Solid Ion Conductors*; Takaharhi, T., Ed.; World Scientific Publishing Co. Inc.: Teaneck, NJ, 1989.

(127)   Yamamura, H.; Yamada, Y.; Mori, T.; Atake, T. *Solid State Ionics* **1998**, *108*, 5.

(128)   Mohn, C. E.; Allan, N. L.; Stølen, S. *Solid State Ionics* **2006**, *177*, 223-228.

(129)   Fisher, C. A. J.; Derby, B.; Brook, R. J. In *British Ceramic Proceedings: Ceramic Oxygen Ion COnductors and Their Technological Applications*; Institute of Materials: 1996; Vol. 56, p 25-33.

(130)   Mitome, M.; Okamoto, M.; Bando, Y.; Yamamura, H. *Journal of Vacuum Science and Technology B* **2001**, *19*, 5.

(131)   Kakinuma, K.; Yamamura, H.; Haneda, H.; Atake, T. *Solid State Ionics* **2002**, *154-155*, 6.

(132)   Kakinuma, K.; Yamamura, H.; Haneda, H.; Atake, T. *Solid State Ionics* **2001**, *140*, 301-306.

(133)   Liu, Y.; Withers, R. L.; Gerald, J. F. *Journal of Solid State Chemistry* **2003**, *170*, 247-254.

(134)   Tenailleau, C.; Pring, A.; Moussa, S. M.; Liu, Y.; Withers, R. L.; Tarantino, S.; Zhang, M.; Carpenter, M. A. *Journal of Solid State Chemistry* **2005**, *178*, 882-891.

(135)   Yao, T.; Uchimoto, Y.; Kinuhata, M.; Inagaki, T.; Yoshida, H. *Solid State Ionics* **2000**, *132*, 189-198.

(136)   Yoshinaga, M.; Yamaguchi, M.; Furuya, T.; Wang, S.; Hashimoto, T. *Solid State Ionics* **2004**, *169*, 9-13.

(137)   Rolle, A.; Vannier, R. N.; Giridharan, N. V.; Abraham, F. *Solid State Ionics* **2005**, *176*, 9.

(138)   Massiot, D.; Vosegaard, T.; Magneron, N.; Trumeau, D.; Montouillout, V.; Berthet, P.; Loiseau, T.; Bujoli, B. *Solid State Nuclear Magnetic Resonance* **1999**, *15*, 159-169.

(139)   Ash, J. T.; Grandinetti, P. J. *Magnetic Resonance in Chemistry* **2006**, *44*, 823-831.

(140)   Fisher, W.; Reck, G.; Schober, T. *Solid State Ionics* **1999**, *116*, 211-215.

(141)   Adler, S. B.; Reimer, J. A. *Solid State Ionics* **1996**, *91*, 175-181.

(142)   Bastow, T. J.; Dirken, P. J.; Smith, M. E.; Whitfield, H. J. *Journal of Chemical Physics* **1996**, *100*, 18539-18545.

(143)   Palumbo, J. L.; Schaedler, T. A.; Peng, L.; Levi, C. G.; Grey, C. P. *Journal of Solid State Chemistry* **2007**, *180*, 2175-2185.

(144)   Turner, G. L.; Chung, S. E.; Oldfield, E. *Journal of Magnetic Resonance* **1985**, *64*, 316-324.

(145)   Fisher, C. A. J.; Islam, M. S. *Solid State Ionics* **1999**, *1999*, 355-363.

(146)   Mollwo, E. *Zeitschrift fuer Physik* **1954**, *138*, 478-88.

(147)   Thomas, D. G.; Lander, J. J. *Journal of Chemical Physics* **1956**, *25*, 1136-42.

(148)   Norby, T. In *HYPOTHESIS II Symposium*; Saetre, T. O., Ed.; Kluwer: Grimstad, Norway, 1998, p 603-608.

(149)   Zhang, G. B.; Smyth, D. M. *Solid State Ionics* **1995**, *82*, 153-160.

(150)   Sutija, D. P.; Norby, T.; Björnbom, P. *Solid State Ionics* **1995**, *77*, 167-174.

(151)   Azad, A. K.; Irvine, J. T. S. *Solid State Ionics* **2008**, *179*, 678-682.

(152)   Norby, T.; Larring, Y. *Current Opinion in Solid State & Materials Science* **1997**, *2*, 593-599.

(153)   Iwahara, H. *Solid State Ionics* **1996**, *86-88*, 9-15.

(154)   Kreuer, K. D. *Solid State Ionics* **1999**, *125*, 285-302.

(155)   Kröger, F. A.; Vink, H. J. In *Solid State Physics, Advances in Research and Applications*; Seitz, F., Turnbull, D., Eds.; Academic Press: New York, 1956; Vol. 3, p 307-435.

(156)   Kreuer, K. D. *Chem. Mater.* **1996**, *8*, 610-641.

(157)   Scherban, T.; Norwick, A. S. *Solid State Ionics* **1989**, *35*, 189-194.

164

(158)   Kreuer, K. D. *Solid State Ionics* **2000**, *136-137*, 149-160.
(159)   Kreuer, K. D.; Schönherr, E.; Maier, J. *Solid State Ionics* **1995**, *70-71*, 278-284.
(160)   Münch, W.; Kreuer, K. D.; Adams; Seifert, G.; Maier, J. *Phase Transitions* **1999**, *68*, 567 - 586.
(161)   Münch, W.; Kreuer, K. D.; Seifert, G.; Maier, J. *Solid State Ionics* **2000**, *136-137*, 183-189.
(162)   Münch, W.; Kreuer, K. D.; Seifertli, G.; Majer, J. *Solid State Ionics* **1999**, *125*, 39-45.
(163)   Hashimoto, T.; Inagaki, Y.; Kishi, A.; Dokiya, M. *Solid State Ionics* **2000**, *128*, 227-231.
(164)   Kakinuma, K.; Tomita, A.; Yamamura, H.; Atake, T. *Journal of Materials Science* **2006**, *41*, 6435-6440.
(165)   Schober, T.; Friedrich, J.; Krug, F. *Solid State Ionics* **1997**, *99*, 9-13.
(166)   Schober, T.; Friedrich, J. *Solid State Ionics* **1998**, *113-115*, 369-375.
(167)   Omata, T.; Kita, M.; Goto, Y.; Okura, T.; Otsuka-Yao-Matsuo, S. *Journal of the Electrochemical Society* **2005**, *152*, A1068-A1072.
(168)   Fisher, C. A. J.; Islam, M. S.; Brook, R. J. *Journal of Solid State Chemistry* **1997**, *128*, 137-141.
(169)   Fischer, W.; Reck, G.; Schober, T. *Solid State Ionics* **1999**, *116*, 211-215.
(170)   Schober, T.; Friedrich, J. *Solid State Ionics* **1998**, *113-115*, 369-375.
(171)   Rolle, A., L'Universite Des Sciences et Technologies De Lille 1, 2005.
(172)   Sternberg, U.; Brunner, E. *Journal of Magnetic Resonance, Series A* **1993**, *108*, 142-150.
(173)   Berglund, B.; Vaughan, R. W. *Journal of Chemical Physics* **1980**, *73*, 2037-2043.
(174)   Jeffrey, G. A.; Yeon, Y. *Acta Crystallographica Section B* **1986**, *B42*, 410-413.
(175)   Kaliaperumal, R.; Sears, R. E. J.; Ni, Q. W.; Furst, J. E. *Journal of Chemical Physics* **1989**, *91*, 7387-7391.
(176)   Eckert, H.; Yesinowski, J. P.; Silver, L. A.; Stolper, E. M. *J. Phys. Chem.* **1988**, *92*, 2055-2064.
(177)   Yesinowski, J. P.; Eckert, H.; Rossman, G. R. *J. Am. Chem. Soc.* **1988**, *110*, 1367-1375.
(178)   Goward, G. R.; Schuster, M. F. H.; Sebastiani, D.; Schnell, I.; Spiess, H. W. *J. Phys. Chem. B* **2002**, *106*, 9322-9334.